2022

Evaluating solar-induced fluorescence across spatial and temporal scales to monitor primary productivity

BOSTON UNIVERSITY

GRADUATE SCHOOL OF ARTS AND SCIENCES

Dissertation

EVALUATING SOLAR-INDUCED FLUORESCENCE ACROSS SPATIAL AND TEMPORAL SCALES TO MONITOR PRIMARY PRODUCTIVITY

by

JULIA KATHRYN MARRS

B.A., Barnard College of Columbia University, 2012
M.A., City University of New York Hunter College, 2016

Submitted in partial fulfillment of the

requirements for the degree of

Doctor of Philosophy

2022

Approved by

First Reader ______________________________
Lucy R. Hutyra, Ph.D.
Professor of Earth & Environment

Second Reader ______________________________
Mark Friedl, Ph.D.
Professor of Earth & Environment

Third Reader ______________________________
Nathan Phillips, Ph.D.
Professor of Earth & Environment

Fourth Reader ______________________________
David W. Allen, Ph.D.
Research Chemist
National Institute of Standards and Technology

DEDICATION

Dedicated to my family, without whose support and encouragement this work would not have been finished. You are a constant source of inspiration to me as a scientist and as a person. I am so grateful for birdwatching (in Wingspan and in real life), drag shows, video games, and good meals with you all, and I love you so much.

ACKNOWLEDGMENTS

I am fortunate to have had the invaluable support and guidance of my advisor Lucy Hutyra, my committee chair Taylor Jones, and my committee members, David Allen, Barry Logan, Mark Friedl, and Nathan Phillips, who have encouraged me and shaped my thinking in so many ways. I would like to thank my collaborators Jaret Reblin, Dalia Tabachnik, David Bombard, Andrew Reinmann, Clare Kohler, Joy Winbourne, Ian Smith, Wiley Hundertmark, Lauren Cabrera, Carol Johnson, Robert Stevens, Masanao Yajima, Ryan Frost, and the Boston University Master of Science in Statistical Practice Consulting team the who have all been so generous with their time and help with the conceptual framing of this work, as well as in the laboratory and field. This work was funded by the National Institute of Standards and Technology, where James Whetstone, in particular, has supported this work at every stage, by the United States Department of Agriculture National Institute of Food and Agriculture, and by the Frederick S. Pardee Center for the Study of the Longer Range Future, where I was lucky to spend a summer with Cynthia Barakatt, John Prandato, and the 2020 Graduate Summer Fellows. I owe a debt of gratitude to the departmental administrators, present and past, in the Department of Earth & Environment, especially Matthew Dicintio, Frederick George III, Lauren Consalvo, Jeffrey Tschirhart, Alissa Beideck Landry, and William Edwards, who have helped me with countless questions and concerns over the years. Last but certainly not least, I am incredibly lucky to know many wonderful scientists and friends, including Luca Morreale, Sarah Garvey, Andrew Trlica, Ana Reboredo Segovia, Tempest McCabe, Celeste Gambino, Hristiana Stoynova, Boris Litvin, John Foster, Emily Schottenfels, Andrew Christ, Shane

Hennessey, Donovan Dennis, Shivani Ehrenfeucht, Nicole Greenhouse, Emma and Kathryn Ruopp, Rajesh Singh, Caden Friedenbach, Katherine Dauber-Decker, and Katie and Andrew Belloli. I could not imagine a better, kinder, or more admirable group of friends, and I will forever be grateful for such excellent company over the last five years and many more to come.

EVALUATING SOLAR-INDUCED FLUORESCENCE ACROSS SPATIAL AND TEMPORAL SCALES TO MONITOR PRIMARY PRODUCTIVITY

JULIA KATHRYN MARRS

Boston University Graduate School of Arts and Sciences, 2022

Major Professor: Lucy R. Hutyra, Professor of Earth & Environment

ABSTRACT

Solar-induced chlorophyll fluorescence (SIF) has been widely cited in carbon cycling studies as a proxy for photosynthesis, and SIF data are commonly incorporated into terrestrial primary productivity models. Though satellite-based SIF products show close relationships with gross primary productivity (GPP), this is not universally true at intermediate scales. A meta-analysis of the tower-based and airborne SIF literature revealed that mean SIF retrievals from unstressed vegetation span three orders of magnitude. While reporting on spectrometer calibration procedures, hardware characterizations, and associated corrections is inconsistent, laboratory and field experiments show that these factors may contribute to significant uncertainty in SIF retrievals. Additionally, there remain ongoing questions regarding the interpretation of SIF data made across spatial scales and the link between satellite SIF retrievals and primary productivity on the ground. Chlorophyll fluorescence originates from dynamic energy partitioning at the leaf level and does not exhibit a uniformly linear relationship with photosynthesis at finer scales. As a standalone metric, SIF measured at the tower scale was not found to track changes in carbon assimilation following stomatal closure induced in deciduous woody tree branches. This lack of relationship may be explained by alternative

energy partitioning pathways, such as thermal energy dissipation mediated by xanthophyll cycle pigments; the activity of these pigments can be tracked using the photochemical reflectance index (PRI). Gradual, phenological changes in energy partitioning are observed as changes in the slope of the SIF-PRI relationship over the course of a season. Along with high frequency effects such as wind-mediated changes in leaf orientation and reflectance, and rapid changes in sky condition due to clouds, PRI offers crucial insights needed to link SIF to leaf physiology. While SIF offers tremendous promise for improving the characterization of terrestrial carbon exchange, and a fuller understanding of the boundaries on its utility and interpretation as a biophysical phenomenon will help to create more reliable models of global productivity.

TABLE OF CONTENTS

LIST OF TABLES

LIST OF FIGURES

LIST OF ABBREVIATIONS

$^1O_2$	singlet oxygen
3FLD	3-band FLD
%	percent
º	degrees
ºC	degrees Celsius
λ	wavelength
λ_{in}	in-band wavelength
λ_{out}	out-of-band wavelength
μ	mean
µm	microns
µmol	micromoles
ρ	reflectance
σ	standard deviation
ΦF	fluorescence yield
ΦP	photochemical yield or photosynthetic light use efficiency
$\Phi PSII$	light-use efficiency of PSII
ω	solid angle
A	antheraxanthin
ABA	abscisic acid
$A_{aperture}$	aperture area
A_{net}	net C assimilation

APAR	absorbed PAR
BC	blue channel
BCC	blue chromatic coordinate
C	carbon
cm	centimeters
CO_2	carbon dioxide
CO_{2i}	leaf internal carbon dioxide concentration
Chl	chlorophyll
D	non-radiative decay
D_{af}	aperture-fiber distance
DESIS	DLR Earth Sensing Imaging Spectrometer
DLR	Deutsches Zentrum für Luft- und Raumfahrt (meaning German Aerospace Center)
DN	digital number
DOAS	differential optical absorption spectroscopy
E	irradiance
ECOSTRESS	Ecosystem Spaceborne Thermal Radiometer Experiment on Space Station
ED	energy dissipation
EDT	Eastern Daylight Time
ESA	European Space Agency
F/*n*	F-number or focal ratio

f_{esc}	canopy escape probability of fluorescence
FL	focal length
FLD	Fraunhofer line depth
F_m’	maximum PAM fluorescence under illumination
FOREST	Forested Optical Reference for Evaluating Sensor Technology
F_s	steady-state PAM fluorescence
F-SFM	full-spectrum SFM
F_v’	variable PAM fluorescence under illumination
F_v’/F_m’	PSII quantum yield under illumination
FWHM	full width at half maximum
g	grams
GC	green channel
GEP	gross ecosystem productivity
GMT	Greenwich mean time
GPP	gross primary productivity
g_{sw}	stomatal conductance to water
ha	hectares
HPLC	high performance liquid chromatography
iFLD	improved FLD
IMS	irradiance-measuring spectrometer
in	inches
km	kilometers

L	radiance
LAI	leaf area index
LME	linear mixed-effects
m	meters
mbar	millibars
Mg	megagrams
min	minutes
mL	milliliters
mm	millimeters
mM	millimolar
mol	moles
MPa	megapascals
ms	milliseconds
mW	milliwatts
n	number
NASA	National Aeronautics and Space Administration
NDVI	normalized difference vegetation index
nFLD	*n*-band FLD
NIR	near-infrared
NIR_v	near-infrared reflectance of vegetation
NIST	National Institute of Standards and Technology
nm	nanometers

O_2	oxygen gas
O_2-A	oxygen A-band atmospheric absorption feature
OSSE	observing system simulation experiment
p	*p*-value or probability value
PAM	pulse-amplitude modulated
PAR	photosynthetically active radiation
P_{ET}	photosynthetic electron transport
P_{CF}	photosynthetic C fixation
pFLD	principal component analysis-based FLD
PRI	photochemical reflectance index
P_{RS}	photorespiration
PSII	Photosystem II
PTFE	polytetrafluoroethylene
R	reflectance
R^2	coefficient of determination
RC	red channel
RHM	reflectance height method
RMS	radiance-measuring spectrometer
s	seconds
SAM	Snapshot Area Map
SFM	spectral fitting methods
SIF	solar-induced chlorophyll fluorescence

SMA	SubMiniature version A
SNR	signal-to-noise ratio
sp.	species
sr	steradians
SR	spectral resolution
SSI	spectral sampling interval
SZA	solar zenith angle
TS	transfer spectroradiometer
V	violaxanthin
VZA	view zenith angle
W	watts
Z	zeaxanthin

CHAPTER ONE: INTRODUCTION

Photosynthesis is a fundamental biological process with crucial implications for food and resource production (Wolf et al., 2015), a wide range of ecological dynamics (Field et al., 2007), and both the current and future status of Earth's climate systems (Allen et al., 2018; Heimann and Reichstein, 2008). The uptake of carbon (C) by the terrestrial biosphere is a key element of the global C cycle (Le Quéré et al., 2018; Pan et al., 2011), and there has been longstanding scientific interest in quantifying the current magnitude and potential future changes in the terrestrial C sink (Ryu et al., 2019). However, due to the challenges to direct measurements of C uptake at the global scale, the terrestrial biosphere is also the source of the largest uncertainties in estimated global carbon budgets (Huntzinger et al., 2017; Rotach et al., 2014). In the interest of addressing these uncertainties, long-running satellite programs have monitored the Earth's surface, and traditional vegetation greenness indices derived from satellite measurements of reflected sunlight can be used to track the extent, health, and dynamics of global vegetation (Thompson et al., 2017). However, these indices suffer from limitations associated with saturation at moderately high leaf area (Asner et al., 2004), posing significant challenges to constraining GPP, particularly because many of the most productive forests are also those with the highest leaf area index (LAI). Furthermore, greenness indices cannot be used to track annual cycles in light use efficiency or primary productivity in evergreen forests, where canopy pigmentation and structure do not change dramatically with the seasons (Gamon et al., 1995; Springer et al., 2017). Attempts to overcome these challenges using global models of GPP have been limited by insufficient data to fully constrain model outputs, particularly in these highly productive regions (Anav et al., 2015). In response to these challenges, there has been increasing interest over the last two decades in measuring solar-induced chlorophyll fluorescence (SIF), a faint and temporally dynamic signal originating from the dissipation of the light absorbed by plant leaves (Porcar-Castell et al., 2014).

Plants face a particular metabolic challenge in that they require photons absorbed from sunlight in order to power linear electron transport (a chain of energy-generating reactions in the light reactions of photosynthesis), but have limited control over how many photons are incident on their leaves at any given moment. In order to avoid cellular damage resulting from the absorption of more photons than can be used for photosynthesis on an instantaneous basis, plants have several additional pathways by which excess energy can be safely used or lost (Baker, 2008). SIF is the result of one such pathway, by which plants may re-radiate light at a higher wavelength than was absorbed, resulting in a net reduction in absorbed energy (Porcar-Castell et al., 2014). An additional share of energy is lost as heat through constitutive, non-radiative decay (D), and leaves may also engage a regulated photoprotective mechanism known as energy dissipation (ED) involving carotenoid pigments of the xanthophyll cycle (Demmig-Adams and Adams, 2006).

A large share of absorbed light is used to support photochemistry in unstressed, healthy leaves (Demmig-Adams, 1998). Levels of ED vary in response to excess light absorption and generally increase during exposure to environmental stress, at times rising dramatically to consume the greatest share of absorbed light (Logan et al., 1998; Verhoeven et al., 1999). With the goal of minimizing cellular damage, the emission of photons as SIF may also be modulated on short time scales in order to dissipate the remaining fraction of unused energy. This energy partitioning may be monitored at the leaf level using pulse-amplitude modulated (PAM) fluorometers (Maxwell and Johnson, 2000), and SIF may be monitored remotely using spectrometer systems to quantify the in-filling of atmospheric absorption features and Fraunhofer lines by fluorescent photons by comparing detailed spectra of radiance measured from vegetation with those collected from downwelling irradiance (Meroni et al., 2009).

Since photochemistry and fluorescence represent competing fates for absorbed photons, both of which also compete with ED, we may expect them to exhibit a complex, perhaps even an inverse relationship (Magney et al., 2020; Porcar-Castell et al., 2008). However, many studies using satellite data report a direct relationship between SIF and upscaled model estimates of GPP (Frankenberg et al., 2011; Sun et al., 2018; Verma et al., 2017). Some authors even report near-universal correlation between SIF and eddy-covariance flux tower-derived GPP estimates (X. Li et al., 2018; Xiao et al., 2019). This apparent contradiction has inspired a great deal of work investigating the linearity of the SIF-GPP relationship across scales. Evidence suggests that satellite-scale linearity may be may be driven in part by averaging across observations collected across multiple latitudes, measurement dates, and environmental conditions (Yao Zhang et al., 2018), and by consistent canopy escape probabilities for SIF photons leaving homogeneous canopies (Dechant et al., 2020), independent of a physiological link. Additionally, the nadir view angle used by most satellite platforms has been shown to result in stronger SIF-GPP relationships than would be found using observations collected from more extreme angles (Z. Zhang et al., 2018). One hypothesis suggests that averaging over areas of vegetation with heterogeneous physiological states linearizes the satellite SIF-GPP relationship to a greater degree than would be observed at the leaf level (Gu et al., 2019a). Other researchers point out that SIF and GPP share a common driver, the amount of photosynthetically active radiation (PAR) absorbed by leaves (APAR) (Du et al., 2017; Miao et al., 2018; Wieneke et al., 2018). A recent synthesis of studies on non-linearity in SIF-GPP relationships emphasizes that most SIF-measuring satellites are in sun-synchronous orbits that permit data collection exclusively around local midday and under clear-sky conditions; under these well-illuminated conditions, observed vegetation would plausibly exhibit a direct, linear SIF-GPP relationship, as many surplus photons are lost as fluorescence alongside high photosynthetic rate (Magney et al., 2020).

Regardless of which combination of these hypotheses is true, it clear that satellites can offer limited insight into leaf or whole-plant energy partitioning on the ground. Thus, while landscape-scale correlation between GPP and SIF is informative, the link between SIF and C fixation at finer spatiotemporal scales remains a crucial area of uncertainty. Many previous studies aimed at addressing this gap have collected intermediate-scale measurements from towers or airborne platforms, with some indicating the possibility of directly downscaling satellite data using transformed tower-based SIF measurements (Duveiller and Cescatti, 2016) and of linearly scaling from instantaneous to monthly SIF-GPP relationships (albeit at large spatial scales) (Wood et al., 2017). Nonetheless, the strength and direction of the SIF-GPP relationship measured at intermediate scales varies widely within the literature (Helm et al., 2020; Maguire et al., 2020), and interpretation of these results is complicated by the variety of instrumentation and measurement geometries used. There are substantial uncertainties associated with spectral resolution (Julitta et al., 2016), changes in ambient temperature (L. Li et al., 2018), atmospheric conditions along the viewing path to vegetated targets (Sabater et al., 2018), sensor noise (Burkart et al., 2015), and the calibration and characterization of deployed hardware. While each of these factors may individually contribute only a small amount of error, these uncertainties compound when attempting to retrieve a dynamic fluorescence signal that counts for only 1 % to 5 % of incoming radiance (Meroni et al., 2009).

Despite these challenges, it appears that the SIF signal can be useful in predicting GPP across scales, so long as it is fully contextualized within energy partitioning dynamics, including energy dissipated as heat. Use of the reflectance-based photochemical reflectance index (PRI) (Gamon et al., 1992), which provides insight into the thermal energy dissipation pathway that competes with both SIF and photochemistry for absorbed light, has been shown to improve SIF-GPP relationships across scales (Chang et al., 2020b; Middleton et al., 2016; Wang et al., 2020). SIF and PRI show dynamic responses to transient environmental changes, as well as diurnal variations and seasonal trends, and can provide complementary insights into controls on SIF and energy partitioning across scales.

In this dissertation, I have worked to understand the boundaries on the utility and interpretation of the SIF signal. My first chapter examines limitations on the potential of SIF to capture energy partitioning dynamics and induced changes in photosynthetic rate at small temporal and spatial scales. In the second chapter of my dissertation, I examine errors and uncertainties introduced by instrumentation and hardware used to measure SIF at the tower scale. Using a meta-analysis of the published literature on SIF measured at similar scales, I contextualize these effects within the wide variability in reported SIF retrieval magnitudes. My third chapter focuses on the identification of leaf- and branch-level environmental and physiological drivers of variation in the SIF signal. Persistent monitoring of vegetation using a camera-coupled spectrometer system enabled an examination of SIF retrievals in the context of leaf-level energy partitioning and physiological variation on rapid (seconds-to-minutes), diurnal, and seasonal time scales. My work has aimed to provide insights into mechanisms by which SIF can offer insight into GPP across spatiotemporal scales, and to identify complementary environmental and instrumentation-related considerations that can improve modelling and upscaling efforts to enhance the utility of the satellite record in tracking vegetation productivity and plant physiology.

CHAPTER TWO: SOLAR-INDUCED FLUORESCENCE DOES NOT TRACK PHOTOSYNTHETIC CARBON ASSIMILATION FOLLOWING INDUCED STOMATAL CLOSURE

Marrs, J.K., Reblin, J.S., Logan, B.A., Allen, D.W., Reinmann, A.B., Bombard, D.M., Tabachnik, D., Hutyra, L.R., 2020. Solar-induced fluorescence does not track photosynthetic carbon assimilation following induced stomatal closure. *Geophysical Research Letters* 47, 1–11. https://doi.org/10.1029/2020GL087956.

Abstract

Since 2006, six satellites measuring solar-induced chlorophyll fluorescence (SIF) have been launched to better constrain terrestrial gross primary productivity (GPP). The promise of the SIF signal as a proxy for photosynthesis with a strong relationship to GPP has been widely cited in carbon cycling studies. However, chlorophyll fluorescence originates from dynamic energy partitioning at the leaf level, and does not exhibit a uniformly linear relationship with photosynthesis at finer scales. We induced stomatal closure in deciduous woody tree branches and measured SIF at a proximal scale, alongside leaf-level gas exchange, pulse amplitude modulated (PAM) fluorescence, and leaf pigment content. We found no change in SIF or steady-state PAM fluorescence, despite clear reductions in stomatal conductance, carbon assimilation, and light-use efficiency in treated leaves. These findings suggest that equating SIF and photosynthesis is an oversimplification that may undermine the utility of SIF as a biophysical parameter in GPP models.

Introduction

The terrestrial biosphere is a crucial sink for anthropogenic emissions of carbon to the atmosphere (Pan et al., 2011) and a focal area of Earth systems research (Le Quéré et al., 2018). Numerous satellite programs monitor global vegetation, but there is insufficient on-the-ground data to fully constrain fluxes and feedbacks in modeled GPP (Anav et al., 2015; Huntzinger et al., 2017). Recent GPP modeling efforts have incorporated remotely measured SIF emitted by vegetation (Porcar-Castell et al., 2014), with satellite SIF retrievals reported to show a positive, linear relationship with upscaled GPP model outputs (Sun et al., 2018) and flux tower estimates across biomes (Verma et al., 2017; Xiao et al., 2019). However, the SIF signal originates from a pathway competing with photochemistry for absorbed light energy, suggesting that photosynthetic rate could be inversely related to fluorescence flux. We hypothesize that strong SIF-GPP correlations arise from a shared driver, such as chlorophyll content or strong seasonal changes in alternative sinks for absorbed energy (Magney et al., 2019a), rather than a universal ability of SIF to report real-time insights into the biophysics of photosynthesis.

SIF contains valuable physiological information. Chlorophyll fluorescence emission has been the subject of several decades' work revealing energy partitioning at the leaf level, typically measured using PAM fluorometers (Maxwell and Johnson, 2000). Such instruments characterize the competing pathways by which leaves maximize the use of energy from absorbed light to power photochemistry, while balancing the need to dissipate excess energy to prevent singlet oxygen ($^1O_2$)-mediated cellular damage (Baker, 2008). Figure 1 depicts the potential fates for a photon with notation, where appropriate, to indicate the associated PAM fluorescence parameters that provide information on each energy partitioning pathway. Data collected using PAM fluorometers can be used to quantify ΦPSII, the light-use efficiency of linear electron transport (a chain of energy-generating reactions originating at Photosystem II) in the light reactions of photosynthesis (P_{ET}). Crucially, the relationship between this parameter and carbon assimilation in the dark reactions of photosynthesis (P_{CF}, also referred to as A_{net} when measured in the context of leaf-level gas exchange) is non-linear, due to photorespiration (P_{RS}), particularly at low internal concentrations of CO_2 (CO_{2i}).

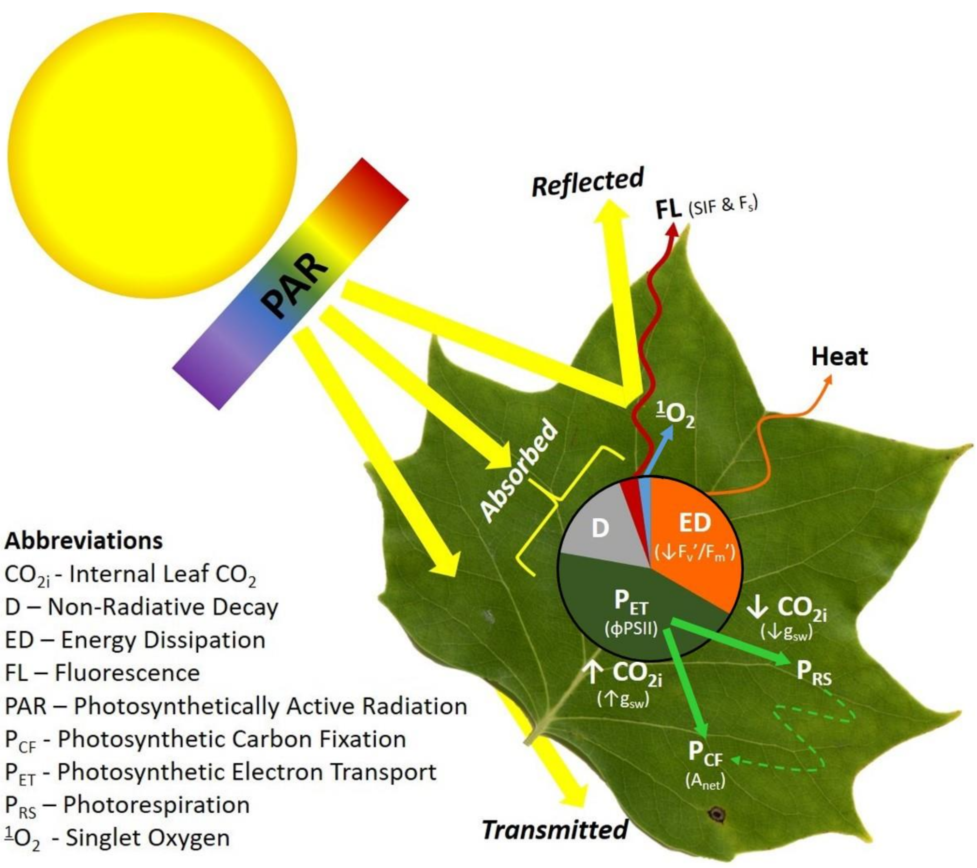

Figure 1. Potential fates for a photon incident on a leaf. Pie chart represents approximate partitioning of absorbed energy among these fates.

A share of absorbed light is used to support photochemistry in unstressed, healthy leaves (Demmig-Adams, 1998), but leaves routinely absorb more photons than can be used on an instantaneous basis. While some energy is lost as heat through constitutive, non-radiative decay (D), leaves may also engage a regulated photoprotective mechanism known as energy dissipation (ED) involving carotenoids of the xanthophyll cycle (Demmig-Adams and Adams, 2006). Energy dissipation can be tracked using PAM fluorescence as decreases in Photosystem II quantum yield measured during illumination (F_v'/F_m') (Demmig-Adams and Adams, 2006; Logan et al., 2007). Levels of ED vary in response to excess light absorption and generally increase during exposure to environmental stress, at times rising dramatically to consume the greatest share of absorbed light (Logan et al., 1998; Verhoeven et al., 1999). Fluorescence emission accounts for the remaining small fraction of absorbed light, typically 1 % to 5 % of incoming radiance (Meroni et al., 2009). PAM fluorometers measure F_s, a broadband, leaf-level quantification of steady-state fluorescence emission from illuminated leaves. F_s is an actively induced signal generated by the measuring beam of a PAM fluorometer, responding to many physiological drivers and providing little insight into photosynthetic activity without consideration of other physiological parameters (Logan et al., 2007). In contrast, SIF is measured as a faint, but highly temporally dynamic enhancement in the apparent reflectance inside spectrally narrow solar Fraunhofer lines or atmospheric absorption features (Meroni et al., 2009).

Since photochemistry and fluorescence represent competing fates for absorbed photons, both of which also compete with ED, we may expect them to exhibit a complex, perhaps even an inverse relationship, as is observed under conditions (e.g. low light) where

ED remains low (Porcar-Castell et al., 2014, 2008). Numerous studies report a positive relationship between SIF and GPP (Sun et al., 2018; Verma et al., 2017; Xiao et al., 2019), suggesting SIF is a proxy for photosynthesis (Yang et al., 2015). Though the term ‘proxy’ indicates an indirect representation used at a scale where direct measurement is impossible, its usage in highly cited SIF studies and conference sessions, (e.g. Yongguang Zhang et al., 2018) has come to imply a more universal substitution in the literature on global GPP modeling. Some researchers have suggested that the strong, direct SIF-GPP relationships observed by satellites at the landscape scale may be an artifact of averaging over space, time, or view angle (Gu et al., 2019a; Yao Zhang et al., 2018; Z. Zhang et al., 2018), which serves to linearize the canopy-scale relationship more than would be observed at a smaller spatial or temporal resolution. Even at the leaf-scale, some have found a non-linear relationship between SIF and GPP, particularly in high-light conditions where photosynthesis saturates while fluorescence emission continues to increase (Gu et al., 2019a; Magney et al., 2017). Similarly, the magnitude of the change in SIF may not track changes in photosynthesis in response to stresses over shorter durations (Helm et al., 2020). Thus, while landscape-scale correlation between GPP and SIF is informative, the link between SIF and leaf or whole-plant physiology on the ground and on shorter time scales remains a crucial area of uncertainty.

Previous work on this question has involved intermediate-scale measurements from towers or airborne platforms, and some authors report sufficient agreement across scales to allow for the creation of methods for downscaling satellite data using transformed tower-based measurements (Duveiller and Cescatti, 2016). However, spatial or temporal aggregation is often employed: though some authors have measured changes in SIF over a period of hours following herbicide application (Pinto et al., 2020), correlations in daily mean tower-based SIF retrievals and flux tower-based GPP are more commonly reported (Wohlfahrt et al., 2018; Yang et al., 2017). Though this aggregation may be justified in the context of other studies reporting linear scaling from instantaneous to monthly SIF-GPP relationships (albeit at large spatial scales) (Wood et al., 2017), averaging across large diel variations limits the ability to track rapid changes in physiological activity.

Materials & Methods

Experimental Design

To evaluate whether remotely sensed SIF tracks changes in photosynthesis at short temporal scales, we experimentally manipulated instantaneous leaf P_{CF} by simulating water stress in deciduous woody trees (Figure S1). Experimental trees were selected for well-illuminated, healthy branches extending out from the site treeline, and included three individuals of *Liriodendron tulipifera*, and three oaks, two individuals of *Quercus palustris* and one of *Quercus alba*. Water stress conditions were simulated using foliar application of the plant hormone abscisic acid (ABA) or a pressure cuff to induce emboli in individual branches. Both treatments were chosen with the goal of inducing stomatal closure, which limits leaf-level exchange of water vapor for carbon dioxide and thereby reduces carbon assimilation in treated leaves without influencing leaf pigment content.

On the morning of 10 July 2019, pre-treatment measurements of SIF, leaf-level gas exchange (A_{net} and stomatal conductance to water, g_{sw}), PAM fluorescence (F_s, ΦPSII, F_v'/F_m'), and leaf pigments (chlorophyll pool, chlorophyll *a/b* ratio, and xanthophyll cycle pigment pool) were made under clear sky conditions. Following pre-treatment measurements, experimental manipulations were performed on all branches. Heavy clouds and light afternoon rains on 11 July 2019 delayed repeat measurements until the following morning. On the morning of 12 July 2019, post-treatment measurements were performed on all branches at the same time of day to within two min, under nearly identical sky conditions.

Site Description & FOREST Project

Data were collected at the Forested Optical Reference for Evaluating Sensor Technology (FOREST) site on the campus of the National Institute of Standards and Technology (NIST) in Gaithersburg, MD. The FOREST site is a remnant stand of large-stature forest (~165 Mg C ha^{-1}) dominated by oaks and tulip poplars, and was established as an urban testbed for carbon monitoring and instrument development in 2017. Complementary biometric and environmental parameters, including soil temperature, soil moisture, air temperature, relative humidity, stem respiration, soil respiration, sap flux, and atmospheric CO_2 concentration were measured at frequent intervals. Further information on data collection methodology and spatial trends can be found in (Smith et al., 2019).

SIF Instrumentation Deployment

Spectra used in SIF retrievals were collected using two QE Pro (Ocean Insight, Largo, Florida, United States) grating spectrometers with a 0.25 nm spectral resolution and a 160 nm spectral range centered at approximately 730 nm. Spectrometers were housed inside a temperature-controlled building (24 ºC ± 2 ºC on average) facing the FOREST treeline, with fiber optic cables running out through wall ports.

Measurements of radiance reflected and SIF emitted from the treeline were collected using a 127 mm 1250 mm FL (F/10) reflector telescope coupled to a fiber optic cable and situated on an external balcony (Figure S2c). When viewing over the approximately 100 m distance between balcony and treeline, the telescope field of view allowed for measurement of an approximately 0.75 m diameter area of interest. The telescope sight was aligned in the field, allowing for targeting of experimental branches (Figure S2e) with ± 10 cm accuracy. More details on alignment methodology may be found in the Supplemental Information.

Vegetation was viewed at a nearly perpendicular angle into the side of the treeline, rather than from above the canopy (Figure S2a). Multiple scattering within leaves may result in proportionally higher near-infrared than red chlorophyll fluorescence emission from the undersides of leaves (Van Wittenberghe et al., 2015), which may be more visible at our site than from a typical tower. However, since we performed SIF retrievals using the Fraunhofer Line Depth (FLD, Plascyk and Gabriel, 1975) method in the near-infrared oxygen A-band (O_2-A) atmospheric absorption feature, this was not anticipated to pose any problems to measurement. Downwelling irradiance was measured using a fiber optic cable affixed along the external wall of the building, with an attached Ocean Insight CC-3 opal glass cosine corrector extending above the roof. The limitations of this cosine corrector at extreme sun angles were characterized using laboratory tests with the fiber and cosine corrector mounted on a rotating stage opposite a known light source. Downwelling spectra were corrected for underestimation of incident irradiance based on solar zenith angle at the time and date of measurement.

Prior to deployment, spectrometers were radiometrically calibrated by transferring the scale from a calibrated spectroradiometer using an integrating sphere at NIST. These radiometric responsivities were determined with the telescope and cosine corrector fore-optics attached, in order to account for spectral and radiometric effects on measured signal. Linear functions determined from laboratory measurements of electronic dark current were used to correct individual field measurements based on spectrometer integration time. Spectra were corrected as in (Sabater et al., 2018) to account for atmospheric O_2 absorption along the branch-telescope path length, as determined using a TruPulse 200 hypsometer (Laser Technology, Inc., Centennial, Colorado, United States). Further details on all corrections and calibrations can be found in (Marrs et al., 2019).

Spectra were recorded consecutively from the field of view targeted with the telescope (n = 20 spectra per branch per day) before and after applying experimental treatments, at the same time of day. Spectra were collected with the highest frequency allowed by spectrometer integration time, adjusted to achieve 80 % to 90 % of detector dynamic range (5.5 s to 12 s, depending on branch illumination levels). Spectra were acquired using OceanView software and were processed in RStudio (RStudio Team, 2015) with custom R (R Core Team, 2018) code. The 3FLD method (Maier et al., 2003) was evaluated alongside the standard FLD approach. We observed a linear relationship between retrievals obtained using the two methods, with lower absolute magnitudes of SIF from the 3FLD retrievals (Figure S3).

Kautsky Curve

To confirm our capacity to detect a physiologically meaningful chlorophyll fluorescence signal, we measured the Kautsky effect (Kautsky and Hirsch, 1931), in which dark-acclimated photosystems suddenly exposed to light are temporarily unable to perform electron transfer, resulting in a large spike in fluorescence intensity as a compensatory mechanism, followed by a gradual decline upon the induction of photochemical and non-photochemical mechanisms of chlorophyll de-excitation. The resulting Kautsky curve (Figure S4) shows strong agreement in timing and relative signal magnitude in PAM fluorescence and SIF measurements, indicating that our remote spectrometer deployment captured the same fluorescence dynamics observed at the leaf level.

Gas Exchange & PAM Fluorescence

Leaf-level photosynthetic CO_2 assimilation and pulse-amplitude modulated chlorophyll fluorescence emission were measured using a LI-COR 6800 photosynthesis analyzer with the 6800-01A fluorometer head (LI-COR Biosciences, Lincoln, Nebraska, United States) (Figure S2b). Measurements were made on full-sun acclimated leaves in the area of interest of the SIF measurements at 1600 µmol photons m^{-2} s^{-1}, a reference concentration of 400 parts per million CO_2, a temperature-control block temperature of 30 °C and a vapor pressure deficit of 2.0, which were intended to simulate ambient conditions for parameters other than temperature, which was set slightly above ambient to reduce the risk of condensation within the instrument. A timeseries of local meteorological data can be found in Figure S5. Branch values represent the mean of triplicate measurements on separate leaves.

ABA

To induce stomatal closure, abscisic acid was applied as a foliar spray with 0.25 g ABA (plantmedia.com, Dublin, Ohio, United States) dissolved in 25 mL of ethanol. The ABA solution was diluted to 0.5 mM ABA in 0.1 % Triton X-100 (~ 2 % ethanol in the final spray) and was liberally applied to both sides of all leaves on ABA-treated branches twice in the afternoon of the pre-treatment day, following intial measurements (Figure S2f). Leaves were treated a second time as above with freshly prepared ABA solution just after dawn on 12 July 2019.

Pressure Cuff

We introduced emboli into the xylem of branches to simulate water stress, prompt stomatal closure, and lower leaf photosynthetic rates. In preliminary testing, it took several hours for pressurizations to affect leaf gas exchange. Experimental branches were pressurized in the late afternoon of 10 July 2019. To introduce emboli, we used a split pressure chamber (Adams and Demmig-Adams, 1992; Hubbard et al., 2001) sealed around branches to inject pressurized nitrogen gas into the xylem. Machined blocks of aluminum were bolted together and sealed around an attached branch (Figure S2d). This chamber enclosed a 10 cm long length of a branch ranging from 1 cm to 2 cm in diameter. The chamber was sealed around the projecting branches using conical rubber gaskets fitted around the stems that expanded radially when compressed by tightening mated aluminum end caps into matching keyways on the chamber. Once sealed, the chamber was slowly pressurized to 6.9 MPa using compressed nitrogen gas. The chamber was held at that pressure for 10 min and was then vented slowly and allowed to return to atmospheric pressure.

In preliminary testing of species with diffuse-porous wood, the leaves on pressure-treated branches wilted significantly following pressurization while leaves from ring-porous species did not. To avoid changes in leaf geometry that might alter remotely measured SIF in ways that were unrelated to the impacts of the stem pressurization on leaf photosynthesis, we did not pressure treat branches of *L. tulipifera* as it has diffuse-porous wood and instead focused the branch pressurizations on ring-porous *Quercus sp.* in this study. No wilting was observed in pressurized *Quercus* branches.

Leaf Chlorophylls & Carotenoids – Extraction & Quantification

Leaf samples for the analysis of chlorophylls and carotenoids were collected from designated pigment-monitoring leaves on each branch both before and after experimental manipulations were performed. These collections were coordinated temporally with measurements of all other parameters made on adjacent leaves of the same focal branches in the same light environment. At the point of collection, leaf samples were immediately frozen in liquid nitrogen and were stored at -80 °C until processed. Leaf pigments were extracted from these stored samples in acetone according to (Adams and Demmig-Adams, 1992) modified as described in (de Viller et al., 2017). Following extraction, leaf pigments were quantified by high performance liquid chromatography (HPLC) as described in (de Viller et al., 2017).

Statistical Analyses

For each tree, one adjacent healthy branch was designated as a control for comparison to treated branches on the same tree. To account for environmental or other external changes across field measurement days, control branch data were used as a baseline for comparison with treated branches on the same tree, with the assumption that all neighboring branches on a tree shared similar physiological conditions before the experiment began. However, in order to compare across sets of branches, it was necessary to control for between-tree variability. Such variability was especially evident in SIF retrievals (see Figure 3), but analyses were performed identically for all parameters. Data were analyzed using linear mixed-effects (LME) models of the interaction between time (pre- vs. post-treatment) and treatment type, with tree identity held as a random effect. Statistical analyses were performed with R (R Core Team, 2018) in Rstudio (RStudio Team, 2015). LME models were constructed and run using the lme4 package (Bates et al., 2015), and 95 % confidence intervals around the coefficient for the interaction term were calculated using the effects package (Fox and Weisber, 2019).

Results

Following experimental manipulations, both A_{net} and g_{sw} decreased significantly, falling nearly to zero (Figure 2). These results indicate that both types of manipulations were effective in reducing stomatal conductance to water and CO_2, resulting in a nearly complete shutdown in P_{CF}. In order to relate these changes back to SIF, they must be assessed in the context of overall energy partitioning in these treated leaves. PAM fluorescence measurements of ΦPSII show a significant reduction following treatment, albeit of a smaller magnitude than observed in g_{sw} and A_{net}. This indicates decreased light-use efficiency of PSII and suggests, in the context of the lower carbon fixation observed in leaf-level gas exchange measurements, that a greater fraction of the energy from P_{ET} is being used for photorespiration after stomatal closure. With observed reductions to energy use in P_{CF}, we expected to see increases elsewhere. Values of F_v'/F_m' decreased by 20 ± 7 % after treatment, indicating increased levels of ED as a compensating mechanism. These observations show that our experimental treatments altered leaf-level energy partitioning, with gas exchange and P_{CF} dramatically reduced, and complementary increases in P_{RS} and ED. Critically, we observe no consistent trends in SIF or F_s that would be indicative of these dramatic changes observed in other energy partitioning parameters.

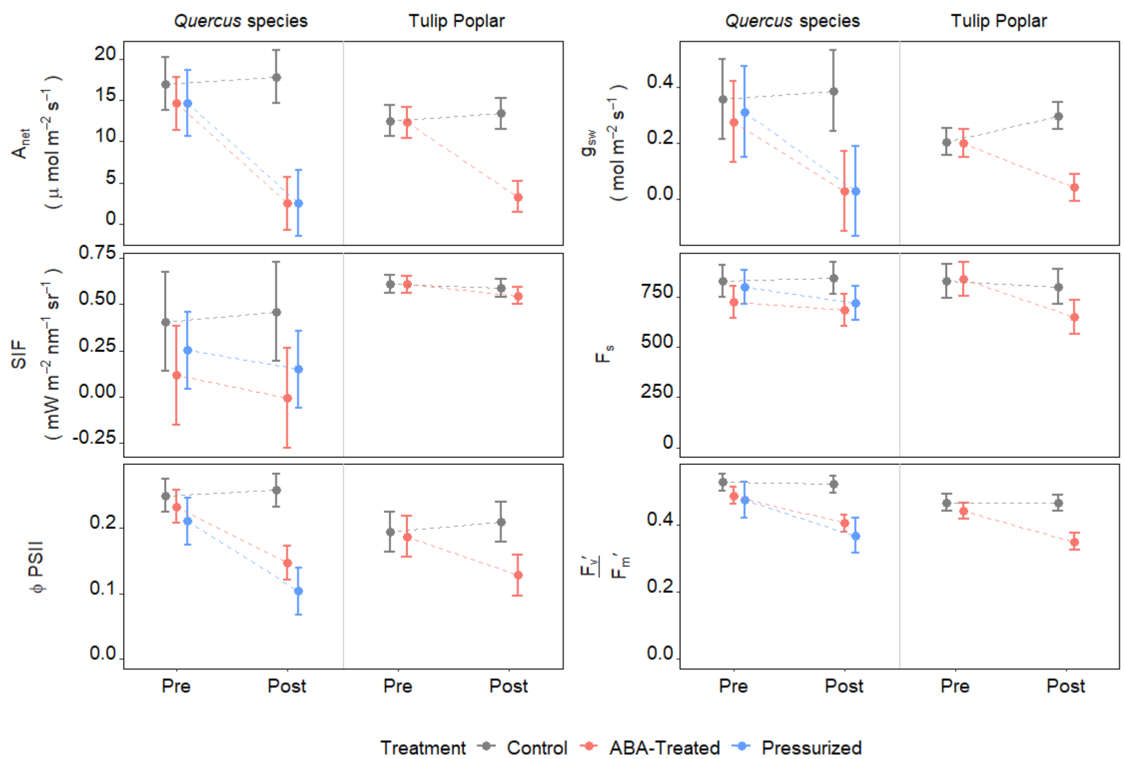

Figure 2. Trends in SIF, gas exchange, and PAM fluorescence parameters. Error bars represent 95 % confidence intervals determined from LME models. Points are means from pre-treament ("Pre") and post-treatment ("Post") days.

Individual SIF retrievals from trees targeted in this experiment are variable, with large branch-to-branch differences in magnitude (Figure 3). While this variability is common and the motivation for spatial and temporal aggregation performed in many studies, we present all data points here for transparency and ease of comparison with F_s values measured from the same branches. SIF varies strongly with instrument field of view, incident light variations, leaf density and angle, and chlorophyll content (Verrelst et al., 2015). Some SIF retrievals on branches with a smaller proportion of illuminated vegetation in the instrument field of view result in small negative values. Negative SIF is a physical impossibility and an artifact of the calculations underlying SIF retrievals, but it also highlights the importance of external drivers on the final magnitude of a recorded SIF value. Similarly, F_s values are variable, with no consistent direction of change between pre- and post-treatment values from treated branches. We observe no changes in leaf chlorophyll pools and a significant change in xanthophyll cycle pool size in only pressurized *Quercus* branches post-treatment (Table 1), and thus can rule out the scenario in which such changes might obscure an otherwise significant trend in SIF or F_s. Neither fluorescence parameter, if used as a stand-alone monitoring method, would have provided insight into the nearly complete elimination of photosynthetic carbon assimilation, nor given clear insight into resulting adjustments in leaf-level energy partitioning. Note that the data presented here were collected following experimental manipulations to three tree species at one study site, this does not necessarily provide universal insight into the range of physiological conditions under which SIF may be measured.

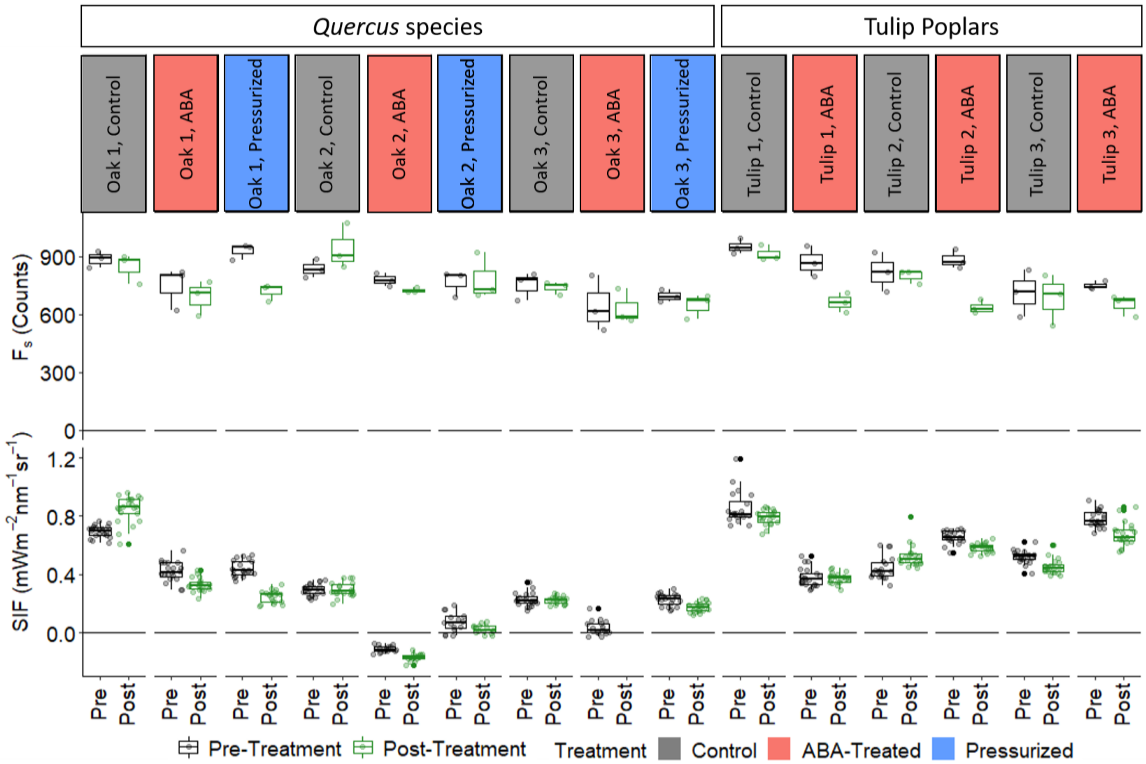

Figure 3. Variability in fluorescence measurements. Individual F_s and SIF. Boxes show 25th percentile, median, and 75th percentile with lines extending to 1.5 times the interquartile range. Oaks 1 and 3 are *Quercus palustris*; Oak 2 is *Quercus alba*.

		Control			Treated	
Parameter	**Species**	**Pre-Treatment**	**Post-Treatment**	**Treatment**	**Pre-Treatment**	**Post-Treatment**
Chlorophyll Pool (Chl $a+b$) (μmol m^{-2})	*Quercus* species	457 ± 109.9	491 ± 110.3	ABA	435 ± 109.9	427 ± 109.9
				Pressurized	433 ± 116.2	431 ± 116.2
	Tulip Poplar	549 ± 69.4	533 ± 76.4	ABA	520 ± 69.4	537 ± 69.4
Chl a:b Ratio	*Quercus* species	3.4 ± 0.19	3.4 ± 0.19	ABA	3.3 ± 0.19	3.4 ± 0.19
				Pressurized	3.3 ± 0.15	3.3 ± 0.15
	Tulip Poplar	2.7 ± 0.06	2.7 ± 0.07	ABA	2.7 ± 0.06	2.7 ± 0.06
Xanthophyll Pool (V+A+Z) (μmol m^{-2})	*Quercus* species	34.3 ± 6.25	34.9 ± 6.43	ABA	34.1 ± 6.25	42.3 ± 6.25
				Pressurized	29.2 ± 5.19	50.0 ± 5.19
	Tulip Poplar	31.7 ± 12.19	39.7 ± 13.02	ABA	32.5± 12.19	45.1 ± 12.19

Table 1. Leaf chlorophyll and xanthophyll concentrations. Error ranges represent 95 % confidence intervals determined from linear mixed effects models. Xanthophyll pigments include V = violaxanthin, A = antheraxanthin, and Z = zeaxanthin.

Conclusions

How do we reconcile the ambiguity in our observations with the strong SIF-GPP relationships found at larger scales? Traditional models of GPP define it as the product of the photosynthetic light-use efficiency (ΦP) of vegetation and absorbed PAR (APAR, the product of PAR intensity and the fraction absorbed by photosynthetic elements on the ground) (Monteith, 1972). SIF, as a phenomenon intrinsically connected to the use or dissipation of incoming light, should contain information about both ΦP and APAR (Porcar-Castell et al., 2014), meaning that it can be related back to modeled GPP. A typical formulation of this relationship sets SIF = $\Phi F \bullet APAR \bullet f_{esc}$, where ΦF is fluorescence yield (Berry et al., 2013) and f_{esc} represents the escape probability of fluorescence (Yoshida et al., 2015). The latter is a crucial factor when modeling the proportion of fluorescence emitted at the leaf level that will reach the outer canopy without being scattered or reabsorbed (Dechant et al., 2020; Verrelst et al., 2015), but one that we can assume to remain constant over a daily course of measurements. Most work on SIF assumes constant ΦF : ΦP in order to formulate the linear relationship between SIF and GPP that matches observations at large scales. However, recent work questions these assumptions, suggesting SIF tracks rates of linear electron transport, thus only providing insights into the light reactions of photosynthesis (Gu et al., 2019a).

If SIF is directly affected by the light reactions, we should not expect it to mirror changes in gas exchange and carbon assimilation, consistent with our experiments. Instead, we propose the hypothesis that the SIF-GPP relationship at large spatial and temporal scales is the result of a shared driver. Chlorophyll content in the vegetated area of interest is a fundamental property relating these two processes; areas with denser vegetation or higher chlorophyll concentrations may fix more carbon and emit more chlorophyll fluorescence. The link between chlorophyll content and APAR has motivated the use of traditional greenness indices as GPP model inputs that may perform nearly as well as SIF when used in combination with other environmental parameters (Sims et al., 2008), and has been demonstrated to drive fluorescence dynamics within canopies (Maguire et al., 2020). Nonetheless, the influence of xanthophyll pigments and ED must also be considered in order to explain seasonal variability in SIF from evergreen forests (Magney et al., 2019a).

SIF has often been described as a proxy for photosynthesis. However, findings from the PAM fluorescence literature show that this is an oversimplification at small spatial and temporal scales, and one that may undermine the utility of the SIF signal as part of a complex, but fundamental biophysical process. Previous studies using herbicides that fully inhibit P_{ET} show increased SIF after treatment (Pinto et al., 2020; Rossini et al., 2015), indicating a clear linkage to leaf-level energy partitioning, though with the opposite trend as satellite-based SIF-GPP relationships. In order to take full advantage of information provided by remotely measured chlorophyll fluorescence, a fuller picture of energy partitioning on the ground is needed. In particular, this includes a need to better characterize energy dissipation dynamics. This may be accomplished in a number of ways; for example, the photochemical reflectance index (PRI) (Gamon et al., 1992) provides insight into the xanthophyll cycle by which energy dissipation is regulated, and can be measured at a variety of scales to match tower, airborne, or satellite SIF measurements. The ability to relate leaf-level phenomena to global processes requires data collection and synthesis across multiple scales. SIF offers tremendous promise for improving the characterization of terrestrial carbon exchange, and a fuller understanding of the boundaries on its utility and interpretation will help to create more reliable models of global productivity.

CHAPTER THREE: INSTRUMENTATION SENSITIVITES FOR TOWER-BASED SOLAR-INDUCED FLUORESCENCE MEASUREMENTS

Marrs, J.K., Jones, T.S., Allen, D.W., Hutyra, L.R., 2021. Instrumentation sensitivities for tower-based solar-induced fluorescence measurements. *Remote Sensing of Environment* 259, 112413. https://doi.org/10.1016/j.rse.2021.112413

Abstract

Solar-induced chlorophyll fluorescence (SIF) has been widely cited as a proxy for photosynthesis and is being incorporated as a common input in terrestrial primary productivity models. Though satellite-based SIF products show close relationships with terrestrial gross primary productivity (GPP), there is wide variability in the magnitude of published SIF retrievals made at intermediate scales. In a meta-analysis of the tower-based and airborne SIF literature, we found that mean SIF retrievals from unstressed vegetation spanned a wide range, from 0.041 mW m^{-2} nm^{-1} sr^{-1} to 14.8 mW m^{-2} nm^{-1} sr^{-1}, with a majority of values falling below 4 mW m^{-2} nm^{-1} sr^{-1}. We compiled information on reported spectrometer calibration procedures, hardware characterizations, and associated corrections from these same papers, and found inconsistent reporting on if and how key calibration methodology was performed. In order to quantify the importance of such methodological differences on final SIF retrievals made at a proximal scale, we performed radiometric calibrations and corrections for electronic dark current, detector noise, atmospheric O_2 absorbance, and cosine corrector effects on three field-deployed spectrometers. We found dramatic changes in SIF retrieval magnitude before and after applying calibrations and corrections, as well as significant differences between instrument

performance in the field and expected performance based on laboratory characterizations. Based on these tests, and on a Monte Carlo simulation of uncertainty estimates associated with each of these corrections, it is likely that calibration methodologies and hardware characterizations explain some of the observed variability in published SIF retrievals. This wide range in baseline SIF retrieval methodologies and resultant magnitudes severely limit researchers' ability to synthesize and advance the utility of SIF in modeling GPP across scales. Further, variability in calibration and correction methodology may explain the weak SIF-GPP relationship across studies at tower scales.

Introduction

The terrestrial biosphere is a crucial sink for anthropogenic emissions of carbon to the atmosphere (Pan et al., 2011), but is also the source of the largest uncertainties in estimated global carbon budgets (Le Quéré et al., 2018). These uncertainties arise in part because global models of the GPP of vegetation are limited by insufficient data to fully constrain outputs (Anav et al., 2015) and by underlying assumptions that oversimplify real-world heterogeneity. Long-running satellite programs have persistently monitored global vegetation via greenness indices (Thompson et al., 2017), but these also suffer limitations associated with saturation at moderately high leaf area (Asner et al., 2004). As a potentially more direct measure of GPP, there has been increasing interest in SIF (Ryu et al., 2019), a faint chlorophyll fluorescence signal originating from the dissipation of excess light absorbed by plants (e.g. Krause and Weis, 1991). If more energy is absorbed by a leaf than can be used for photosynthesis on an instantaneous basis, plants may re-radiate light at a longer wavelength as one of several strategies to dissipate this unused energy and avoid cellular damage (Baker, 2008; Porcar-Castell et al., 2014).

Recent advances in remotely measuring GPP take advantage of this signal as a means of remotely tracking primary productivity. Satellite platforms measure SIF as a weak enhancement in the apparent reflectance inside solar Fraunhofer lines and atmospheric absorption features (Meroni et al., 2009). SIF shows a strong linear relationship with GPP at the satellite scale (Frankenberg et al., 2011; Sun et al., 2018; Verma et al., 2017). However, the near-universal correlation reported between satellite SIF and flux tower estimates of GPP (X. Li et al., 2018; Xiao et al., 2019) may be driven by satellite view angle (Z. Zhang et al., 2018), canopy structure (Dechant et al., 2020) and temporal aggregation or averaging (Lin et al., 2019), independent of a physiological link. In general, averaging over areas of vegetation with heterogeneous physiological states likely linearizes the satellite SIF-GPP relationship to a greater degree than would be observed at the leaf level (Gu et al., 2019a). While the relationship between GPP and SIF is also encouraging at tower and airborne scales (Magney et al., 2019a; Yang et al., 2017; Zarco-Tejada et al., 2016), the link between SIF measured from a remote platform and plant physiology on the ground remains a crucial area of study.

Previous work confronting these challenges has employed intermediate-scale measurements from towers, drones, or light aircraft, which offer the opportunity for closer comparisons with flux tower and leaf-level quantifications of primary productivity. There is some evidence that the SIF-GPP relationship may hold across spatial and temporal scales (Duveiller and Cescatti, 2016; Wieneke et al., 2018; Wood et al., 2017) and that more nuanced relationships observed at finer spatiotemporal scales may not contradict linear relationships found elsewhere (Magney et al., 2020). Nonetheless, other authors show that intermediate-scale SIF measurements are subject to diurnal (Campbell et al., 2019; Middleton et al., 2017), seasonal (Liu et al., 2017; Nichol et al., 2019), and structural (Goulas et al., 2017; Migliavacca et al., 2017) effects that influence attempts to directly relate these values to GPP. Additionally, the interpretation of SIF values measured from towers and aircraft is complicated by the variety of associated instrumentation and measurement geometries. There are substantial uncertainties around absolute SIF retrieval magnitude associated with differences in spectral resolution (Julitta et al., 2016), changes in ambient temperature (L. Li et al., 2018), atmospheric conditions along the viewing path to vegetated targets (Sabater et al., 2018), sensor noise (Burkart et al., 2015), stray light effects (Albert et al., 2019), SIF retrieval method (Chang et al., 2020a), and the calibration and characterization of deployed hardware. Various methods for accounting for each of these potential error sources have been considered (Gu et al., 2019b) and their influence on final SIF retrievals quantified within individual field-deployed systems (Frankenberg et al., 2018; Grossmann et al., 2018). While each of these factors may individually contribute only a small amount of error, these uncertainties compound when attempting to retrieve a dynamic fluorescence signal that counts for only 1 % to 5 % of incoming radiance (Meroni et al., 2009). Recent work by Pacheco-Laborador and colleagues (2019) modeled the effects of numerous potential sources of uncertainty originating from typical SIF-measuring instrumentation and hardware. In this work, we sought to investigate how these crucial factors have been taken into account in the published literature, and to expand upon this comprehensive characterization of error sources by investigating the effects of instrument deployment in a field setting.

We performed a meta-analysis of SIF values and retrieval methods, target type, vegetation stress conditions, hardware specifications, and calibration methodology. We contextualized calibrations and hardware characterizations in our field-based system within the published literature on tower-based and airborne SIF retrievals. That literature stretches back nearly two decades and includes a wide variety of measurement platforms deployed across seasons and land cover types for a variety of purposes. In order to understand and correct for these same effects on a field-deployed system, we performed a variety of calibrations and characterizations in both laboratory and field settings. Using those data, we analyzed the effects of these factors on the magnitude of, and uncertainty around, retrieved SIF values. Using these two complementary analyses, we examined sources of hardware-based and environmental uncertainty that may contribute to variability in SIF retrieval magnitude and SIF-GPP relationships at intermediate scales.

Methodology

Meta-analysis

In order to capture information on SIF values observed at the tower scale, we performed a meta-analysis of the published literature. On 19 September 2019, a Web of Science search was performed using the search terms “sun induced fluorescence” OR “solar induced fluorescence” AND “tower” (capitalized conjunctions indicate search engine logical operators). The search was repeated with the term “airborne” in place of “tower,” but this search yielded an identical list. Our search returned 246 papers, and an initial check was performed by scanning abstracts and methods sections for mentions of SIF data collected from tower, drone, crane, or airborne platforms. Studies of only data from satellite-based platforms or which concerned only modeling work with no field component were excluded from this analysis. This resulted in a final pool of 91 papers published since 2003, which were then examined in depth. Details were extracted on numerous variables, including maximum and mean SIF values for control and (if applicable) stress conditions, instrument specifications, target vegetation location and species, data collection protocol, SIF retrieval method, and whether and how a variety of calibrations and corrections were performed. Calibrations and corrections investigated included those that introduce random error, such as stray light and detector signal-to-noise ratio, those that can introduce constant offsets, such as the choice of a radiometric light source for calibration, those that are dependent on sun angle and illumination level, such as detector nonlinearity, correction for electronic dark signal, or choice of cosine corrector material, as well as distance-dependent effects of atmospheric corrections. A plot visualizing the number of corrections applied by the papers in this analysis can be found in Figure S6a. Data were recorded for a total of 61 variables; the full results of this meta-analysis can be found in Table S1 (references cited in Table S1 include Alonso et al., 2017; Amoros-Lopez et al., 2006; Atherton et al., 2016; Bandopadhyay et al., 2019; Buddenbaum et al., 2015; Burkart et al., 2015; Campbell et al., 2019; Cecchi et al., 2003, 1994; Cendrero-Mateo et al., 2018; Cheng et al., 2013; Cogliati et al., 2018, 2012; Colombo et al., 2016; Corp et al., 2006; Damm et al., 2010; Daumard et al., 2016, 2012, 2010; Ding et al., 2017; Drolet et al., 2014; Du et al., 2019; Frankenberg et al., 2018; Gamon et al., 2018; Garzonio et al., 2017; Gerhards et al., 2018; GomezChova et al., 2006; Goulas et al., 2017; Grossmann et al., 2018; Hernandez-Clemente et al., 2017; Hu et al., 2018, 2017; JB-Hyperspectral Devices UG, 2019; Jimenez et al., 2018; Jülich Research Centre, 2014; Liu et al., 2017, 2005; Lu et al., 2018; Lucieer et al., 2014; Magney et al., 2019a; Makisara et al., 1993; Meroni et al., 2011; Miao et al., 2018; Middleton et al., 2017, 2007; Migliavacca et al., 2017; Moya et al., 2006; Ni et al., 2016; Nichol et al., 2019; Paul-Limoges et al., 2018; Perez-Priego et al., 2015; Pinto et al., 2017; Qiu et al., 2018; Raczka et al., 2019; Rascher et al., 2015, 2009; Rossini et al., 2016, 2015, 2010; Shan et al., 2019; von Hebel et al., 2018; Wieneke et al., 2018; Wohlfahrt et al., 2018; Wyber et al., 2017; Xu et al., 2018; Yang et al., 2017, 2018, 2015; Zarco-Tejada et al., 2016, 2013; Y J Zhang et al., 2018). A majority, 61 papers, reported SIF data in radiometric units, rather than as uncalibrated digital numbers, or relative quantifications of fluorescence magnitude. Of these, 24 also reported data on GPP, gross ecosystem productivity (GEP), or leaf-level net carbon assimilation (A_{net}) on the same vegetation targets from which SIF data were collected.

Maximum and mean values of SIF and primary productivity were taken directly from the publication when possible, or were extracted as hand-digitized points from relevant figures using Plot Digitizer software (Huwaldt, 2015). All available points from relevant figures were digitized, sometimes including those representing variable sky conditions or low-light hours. However, many authors specified that their reported data were filtered for the influence of clouds or otherwise filtered to include only SIF retrievals made in high-light conditions; no paper represented in this meta-analysis presented data from exclusively low-light conditions. Because of differences in scope across all the papers in this analysis, the mean values in Table S1 represent averages over different time scales. Details of these differences in temporal scale are noted in the table, but were not analyzed in detail here.

Study Site

Field measurements were made at the Forested Optical Reference for Evaluating Sensor Technology (FOREST) test site, established in 2016 on the campus of the National Institute of Standards and Technology (NIST) as a testbed for urban carbon monitoring alongside instrument calibration and validation procedures (Marrs et al., 2020). The FOREST site is a remnant stand of large-stature forest (~165 Mg C ha^{-1}) dominated by oaks and tulip poplars. Within a one hectare plot, biometric and environmental parameters, including soil temperature, soil moisture, air temperature, relative humidity, stem respiration, soil respiration, sap flux, and atmospheric CO_2 concentration were measured at frequent intervals as detailed in Smith et al. (2019). Complementary atmospheric measurements from a nearby weather station on the NIST campus further facilitated the examination of links between observable optical signals and underlying biophysical phenomena.

Laboratory Calibration & Characterization

Three Ocean Insight QE Pro grating spectrometers were characterized during the process of testing and deploying field instrumentation. Over the course of the 2017 – 2019 summer field seasons, the same spectrometer (QE Pro 1) was used to measure reflected radiance and fluorescence from vegetated targets. One spectrometer (QE Pro 2) was used to measure downwelling solar irradiance during the 2017 season, and was replaced with

QE Pro 3 for the 2018 and 2019 field seasons. All field SIF retrievals presented here were collected with a dual-spectrometer setup, where QE Pro 1 collected reflected radiance and fluorescence, and either QE Pro 2 or QE Pro 3 (depending on the year) was used to measure downwelling irradiance. Although the use of a dual spectrometer system may introduce some errors due to small spectral offsets even between spectrometers with the same specifications (Cendrero-Mateo et al., 2019), we chose this configuration in order to simultaneously measure sky and vegetation targets, thereby avoiding issues of differential illumination in sequential measurements. All spectrometers had an F-number of 4, a full width at half maximum of 0.45 µm, and used a #H36 grating, a 5 µm slit size, and 1044 pixel detectors. Table 2 summarizes the details of spectral range and resolution for each instrument.

Instrument	**Spectral Range**	**Dispersion**
QE Pro 1	650.2 nm to 883.6 nm	0.225 nm/pixel
QE Pro 2	650.3 nm to 878.6 nm	0.221 nm/pixel
QE Pro 3	650.2 nm to 876.5 nm	0.219 nm/pixel

Table 2. Spectrometer Specifications. Spectral range and resolution details for three grating spectrometers used in our analyses. Values in this table differ slightly from the nominal values specified by the manufacturer.

Radiometric Responsivity

The spectral radiance responsivity of each of our spectrometers was determined by transferring the scale of a calibrated Spectral Evolution SR3500 spectroradiometer (Spectral Evolution, Haverhill, Massachusetts, United States) using a large lamp-illuminated integrating sphere (diameter = 1.2 m with a 45 cm exit port). Radiometric responsivity values convert the raw digital number (DN) values recorded by the spectrometer detector into physical units of radiance (L) or irradiance (E). The fiber optic of the transfer spectroradiometer (TS) was mounted alongside the fiber and fore-optic of each instrument to be characterized, positioned so that the field of view was filled by the aperture of the integrating sphere.

In the case of the instrument used to measure radiance, the responsivity was calculated as in Equation 1. The radiance-measuring spectrometer (RMS) was attached to an Ocean Insight QP400-2-VIS-NIR fiber optic cable; this cable was 2 m in length with a 400 µm core diameter. This fiber optic cable was coupled via a SubMiniature version A (SMA) connector to a 127 mm diameter reflector telescope with a focal length of 1250 mm (F/10). Radiometric responsivity was determined with this telescope attached as in the field deployment. The telescope lens and calibrated spectroradiometer fiber tip were placed 49.5 cm from the integrating sphere aperture, a distance at which it was empirically determined that light from the integrating sphere filled the full field of view of the telescope.

$$Responsivity = (DN_{RMS} - DN_{RMS,\,dark}) / L_{TS} \qquad (1)$$

Each spectrometer used to measure irradiance was deployed in the field and radiometrically calibrated with an Ocean Insight CC-3 cosine corrector attached via an SMA connector to an Ocean Insight custom fiber optic cable, 6.67 m in length with a 400 µm core diameter. To account for the diffusive properties of this cosine corrector, additional considerations were made during calibration design and responsivity calculation (Figure S7). In order to avoid distance dependence issues when working with irradiance-measuring instruments, these measurements were made from a distance (D_{af} = 139.7 cm) at which the signal was empirically determined to plateau at equal or greater distances. To correct for the signal measured by the transfer spectroradiometer, which was not equipped with a cosine corrector, the aperture-fiber distance (D_{af}) and aperture area ($A_{aperture}$) were used to determine the solid angle (ω) being measured, and to convert the transfer spectroradiometer signal into irradiance values before calculating responsivity, as shown in Equations 2 to 4, where IMS is the irradiance-measuring spectrometer.

$$\omega = A_{aperture} / D_{af}^2 \tag{2}$$

$$E_{TS} = L_{TS} \bullet \omega \tag{3}$$

$$Responsivity = (DN_{IMS} - DN_{IMS,\, dark}) / E_{TS} \tag{4}$$

Laboratory Signal-to-Noise Ratios

Multiple spectra (n = 30 for radiance-measuring spectrometer; n = 5 for irradiance-measuring spectrometers) were collected and averaged in order to determine radiometric responsivities from the large integrating sphere. Numbers of spectra were determined based on integration time needed to reach 80 % to 90 % of detector saturation, as well as the low variability in signal from the integrating sphere. The standard deviation between repeated measurements from the integrating sphere light source is approximately 5×10^{-5} W m^{-2} nm^{-1} sr^{-1}. Using these data, signal-to-noise ratios (SNR) were calculated by normalizing the mean of consecutively collected spectra by their standard deviation. Since the integrating sphere is a stable light source over the time of repeat spectrum collection, these represent SNR values under laboratory conditions with low humidity and stable temperature.

Fore-Optics

Potential spectral effects of attached fore-optics were also tested by mounting spectrometers side by side on a balcony platform under clear sky conditions with all fore-optics removed. Spectra of sky illumination were recorded, then the same fiber was attached to each instrument one by one and the sky was re-measured. A cosine corrector was added to the end of the fiber following each measurement and sky illumination was again measured. All measurements for each instrument were made within 20 min of each other. No spectral shifts were observed as a result of attaching any fore-optics; more details and results of this test were described by Marrs et al. (2019).

Cosine Corrector

A cosine corrector is a small disc of diffusive material added to the end of a fiber optic cable in order to reduce the angular effects of solar position when measuring downwelling irradiance in the field. While a perfect cosine corrector would collect light over a full 180º, allowing integrated measurements from the full hemisphere of the sky, imperfections in the diffusive disc or its housing would result in a more limited field of view and a potential underestimation of incoming irradiance. In order to characterize different diffusive materials used in the cosine correctors being considered for our final field deployment, we tested the performance of three cosine correctors in a laboratory setting.

A spectrometer-coupled fiber optic cable was mounted on a rotating stage on one end of a laboratory optical bench. At the other end (distance = 232.4 cm), a 1000 W FEL lamp (FEL is a lamp designation, not an acronym; see Fraser et al., 2007) was mounted, centered in front of an alignment laser. A cosine corrector was connected to the front of the fiber optic cable, and a first measurement was made with the fiber aligned directly toward the FEL lamp, simulating a measurement with the sun directly overhead (simulated solar zenith angle (SZA) = 0º). Measurements repeated at 10º increments away from the lamp in each direction, simulating solar zenith angles up to 60º. Photos of this experimental design can be found in Figure S8. This procedure was performed using Ocean Insight CC-3 opal glass, Ocean Insight CC-3-UV-S Spectralon, and Ocean Insight CC-3-UV-T Teflon cosine correctors. The latter two materials are both made of polytetrafluoroethylene (PTFE); Teflon has a higher density and lower transmissivity than Spectralon (Tsai et al., 2008). In order to account for diffuse reflectance off other surfaces in the laboratory, a post (1.27 cm in diameter) was placed between the diffuser and FEL lamp, at a distance of 52.1 cm from the lamp. Black tape was added to the side of the post facing the diffuser in order to further reduce stray light reflected back in the direction of measurement. Measurements were repeated with the post in place with all diffuser materials at all angles, and the resulting diffuse signals were subtracted during analysis.

The performance of each diffusive material was characterized by comparing the amount of light collected at a simulated solar zenith angle of 0º to that collected at each angle away from center. With a perfect cosine corrector, the amount of measured light should fall off at extreme angles following a cosine function, where we would expect to see a 50 % reduction in measured light intensity at 60º away from center. Reductions below this expected cosine curve in the laboratory translate to an underestimation of incoming irradiance in the field. This underestimation was calculated at multiple wavelengths in order to characterize spectral dependence in cosine correction. In order to characterize what these underestimations mean for SIF retrievals, custom R code (R Core Team, 2018) simulating solar geometry was written and run in RStudio (RStudio Team, 2015) to estimate resulting error at different times of day and year.

Electronic Dark Current

Detector electronic dark current was characterized in the laboratory by varying the integration time of measurements made while blocking light from the fiber port of each instrument. A linear function was fit to each set of measurements in order to describe the increase in dark current signal with increasing integration time. Data used to fit these linear functions were visualized by Marrs et al. (2019). During field measurements, these spectrometer-specific functions were used to subtract expected electronic dark current based on measurement integration time.

Field Characterizations

At the FOREST field site, spectrometers were housed inside a temperature-controlled building (24 ºC ± 2 ºC) facing the FOREST treeline, with fiber optic cables running out through wall ports. The telescope used to measure reflected radiance from the treeline was situated on an external balcony, coupled to one of the fiber optic cables. The balcony extends from the third story of the field building, such that the treeline was viewed at a nearly perpendicular angle (Figure S9). Although this view angle is more extreme than in some other tower systems, our meta-analysis revealed a wide range in view zenith angles in systems studied here (Figure S10). When viewing over the approximately 100 m distance between balcony and treeline, the telescope field of view was approximately 0.75 m. Downwelling irradiance was measured using a fiber optic cable affixed along the external wall of the building, with the cosine corrector extending above the roof. For all field data presented here, a cosine corrector with an opal glass diffuser was used.

Field Signal-to-Noise Ratios

SNR values measured in the laboratory can provide an estimate of an instrument's performance when measuring a stable light source in controlled conditions. However, the SIF signal is faint and temporally dynamic, and must be retrieved from radiance and irradiance signals. SIF retrievals presented here were performed using the Fraunhofer Line Depth (FLD) method (Plascyk and Gabriel, 1975), in which SIF is retrieved as an in-filling in the atmospheric O_2-A absorption feature. This involves a transformation of spectral radiance and irradiance signals measured at 757.5 nm (λ_{out}) and 760.5 nm (λ_{in}); the full formula is presented in Equation 5.

$$SIF = [(E_{\lambda out} \bullet L_{\lambda in}) - (L_{\lambda out} \bullet E_{\lambda in})] / (E_{\lambda out} - E_{\lambda in}) \quad (5)$$

Due to changes in solar position over hours and seasons, dynamic atmospheric conditions, and changes in leaf angle and illumination due to wind, we can expect both lower signal intensity and higher variability in the field than in the laboratory. In order to characterize these differences, SNRs were calculated from a time series of data collected continuously from 11:30 to 14:30 local time (15:30 to 18:30 GMT) on 6 September 2018 (day of year 249) for radiance and irradiance data at both in- and out-of-band wavelengths, as well as the resulting SIF retrievals. Each SNR time series was calculated as the mean of values recorded within a 5 min interval divided by the standard deviation of those values.

Atmospheric Correction

Over the approximately 100 m path length between vegetation and balcony-mounted instrumentation (and even over much smaller distances), it is necessary to apply an atmospheric correction to recorded spectra in order to account for additional absorption by atmospheric O_2 along this 100 m path length. Atmospheric transmissivity at 760.5 nm (inside the well of the O_2-A absorption feature) was calculated as in Sabater et al. (2018) to account for atmospheric O_2 absorption, using air temperature, air pressure, and relative humidity data recorded as near as possible to the time of measurement. These values were also adjusted to the path length between the telescope and canopy area of interest, as determined using a TruPulse 200 hypsometer. The inverse of this transmissivity was then used to correct for the signal lost along the path from the treeline to the telescope.

Physiological Measurements

Given the many above-described factors that affect field measurements of SIF, we performed a test to confirm that our deployed instrumentation could be used to measure a physiologically meaningful chlorophyll fluorescence signal. The Kautsky effect is a phenomenon in which photosystems of dark-acclimated vegetation suddenly exposed to light are temporarily unable to perform electron transfer, resulting in a large spike in fluorescence intensity as a compensatory mechanism, followed by a gradual decline upon the induction of photochemical and non-photochemical mechanisms of chlorophyll de-excitation (Kautsky and Hirsch, 1931). This effect is traditionally measured using a pulse-amplitude modulated (PAM) fluorometer at the leaf level (Maxwell and Johnson, 2000), but can also be captured by remote observations.

A portion of *Quercus alba* (white oak) foliage, approximately 2 m in diameter and 100 m from the field building balcony, was dark-acclimated by covering with a tarp for 30 min. A FMSII PAM fluorometer (Hansatech Instruments Ltd., King's Lynn, Norfolk, United Kingdom), was attached to a healthy leaf on this branch just before removal of the tarp. The radiance-measuring telescope system was pointed at the center of this branch. Spectra were collected for 5 min, with a 5 s integration time determined based on illumination level. In this and all following field experiments, integration time was set and dynamically adjusted with the goal of maintaining 80 % to 90 % of detector saturation.

Uncertainty Estimation

Spectral measurements of downwelling irradiance and reflected radiance in the field are subject to angular, atmospheric, temporal, and illumination effects that may alter the final value of a SIF retrieval. We employed a Monte Carlo method to characterize the uncertainty resulting from these effects over the course of a day. For this estimation, we used idealized data for downwelling irradiance at both in-band ($E_{\lambda in}$) and out-of-band ($E_{\lambda out}$) wavelengths, and for out-of-band reflected radiance ($L_{\lambda out}$); these data were based on a smoothed time series of data collected at our field site (Figure S11a-b). Smoothing was performed using the stat_smooth function in R (Wickham et al., 2019). We also used an idealized SIF time series for the same hours, based on SIF values retrieved from the original time series used to generate the smoothed radiance and irradiance data. For the purposes of this analysis, these values were considered to be true SIF magnitudes to which retrievals performed under different scenarios were compared. From these prescribed $E_{\lambda in}$,

$E_{\lambda out}$, $L_{\lambda out}$, and SIF data, in-band radiance values ($L_{\lambda in}$) were calculated using the FLD SIF retrieval formula given in Equation 5.

Using these values, we then performed a SIF observing system simulation experiment (OSSE), with different combinations of corrections for electronic dark current, detector noise, cosine corrector effects, and atmospheric O_2-A absorption applied during the retrieval process. The magnitude of the applied correction was calculated for each time point, depending on illumination level, solar geometry, and environmental parameters. The suncalc package in R (Thieurmel and Elmarhraoui, 2019) was used to determine solar geometry and was combined with the cosine corrector characterization data from Figure 6 and Figure S12 to account for cosine corrector error. A time series of air temperature, air pressure, and relative humidity were obtained from a nearby Weather Underground station (Figure S11c-e) and were used as in Sabater et al. (2018) to calculate overall error in the atmospheric correction by adjusting the $L_{\lambda in}$ value from Equation 5 to account for the estimated absorption along the path length between vegetation and sensor. This implementation applies to the standard FLD retrieval method, but atmospheric corrections must be calculated and implemented differently for other retrieval methods (Chang et al., 2020a). In addition, distributions of uncertainty associated with each of these corrections were defined. Electronic dark correction and detector noise error distributions were determined from laboratory characterizations of three Ocean Insight QE Pro spectrometers; more details on these values can be found in Marrs et al. (2019). For each run of the OSSE simulation, dark current and detector noise effects were selected from known distributions. All errors were propagated through the SIF retrieval performed at each time point, producing a range of SIF values to be compared with the true SIF time series. For each combination of corrections, 500 simulations were performed. Table 3 shows details of the parameters and uncertainty distributions used in these simulations.

Parameter	**Value**
Distance to Target	100 m
Latitude	39.126º north
Longitude	77.221º west
Radiometric Responsivity – Radiance	In-band: 289.25 DN W^{-1} m^{-2} nm^{-1} sr^{-1} ms^{-1} Out-of-band: 291.5 DN W^{-1} m^{-2} nm^{-1} sr^{-1} ms^{-1}
Radiometric Responsivity – Irradiance	In-band: 242.3833 DN W^{-1} m^{-2} nm^{-1} ms^{-1} Out-of-band: 244.0667 DN W^{-1} m^{-2} nm^{-1} ms^{-1}
Air Temperature Uncertainty	Standard deviation = 0.3 ºC
Air Pressure Uncertainty	Standard deviation = 50 mbar
Relative Humidity Uncertainty	Standard deviation = 5 %
Dark Correction Distribution	Uniform distribution: Min = 0.015 ms DN^{-1} Max = 0.091 ms DN^{-1}
Detector Noise Distribution	Normal distribution: Mean = 0 DN, SD = 7.5 DN

Table 3. Parameters used in the observing system simulation.

Results

In a meta-analysis of the literature on tower-based SIF-measuring systems, we found wide variability in reported SIF retrieval magnitudes, coupled with similar variation in instrumentation, hardware, and calibration methods. In order to contextualize this variability within the scope of field-deployed SIF-measuring systems, we characterized the performance of several spectrometers and associated hardware in both laboratory and field settings. We identified spectral, angular, and atmospheric effects with the potential to affect retrieved SIF values and to alter the performance of the field-deployed hardware below what laboratory characterizations would suggest. Based on variability in our hardware, we used a Monte Carlo approach to quantify the uncertainties in SIF retrievals introduced by several key corrections and calibrations. Of these, the correction for atmospheric O_2 absorption in the wavelengths used for SIF retrievals showed the most dramatic effects; our meta-analysis showed that this correction is inconsistently applied in the literature. Overall, the results of our field testing suggest that differences in instrumentation and calibration across field studies may contribute to the wide variability in published SIF retrievals.

Meta-analysis

A meta-analysis of the literature on tower-based SIF measurements reveals a wide range in mean values for far-red SIF retrievals from unstressed vegetation. Discussion of the results and implications of this meta-analysis will focus on far-red SIF retrievals. Where available, mean and maximum SIF values from red wavelengths are summarized in Table S1 and show similar trends in mean SIF retrieval variability to far-red SIF retrievals. Although there is an established literature on the physiological information captured by different wavelengths of the chlorophyll emission spectrum (e.g. Magney et al., 2019b), we chose not to focus on red retrievals here, due to the smaller number of reported data in this wavelength range. Even within the red and far-red retrieval categories, differences exist among the various spectral windows or wavelengths used to perform SIF retrievals. A full analysis of these retrieval effects is outside the scope of this manuscript, but the choice of window size and central wavelength certainly also influences SIF magnitude (Cendrero-Mateo et al., 2019).

Although the majority of mean SIF values are below 4 mW m^{-2} nm^{-1} sr^{-1}, the full range of reported mean values spans three orders of magnitude, from 0.041 mW m^{-2} nm^{-1}

sr^{-1} to 14.8 mW m^{-2} nm^{-1} sr^{-1} (Figure 4a). Variability is also high even within seasons. Summer values for unstressed vegetation range two orders of magnitude, from 0.16 mW m^{-2} nm^{-1} sr^{-1} to 14.8 mW m^{-2} nm^{-1} sr^{-1} (Figure 4b). These ranges include values across seasons; the minimum values from Magney et al. (2019a) are from a dataset collected on evergreens in winter, and the maximum value from Corp et al. (Corp et al., 2006) are from an agricultural field in summer.

Within this wide variability, some patterns related to seasonality and land cover type emerge. SIF retrievals from forested targets show an annual pattern, with higher SIF values reported from spring and summer measurements than from autumn or winter measurements (Figure 4b). Perhaps because of irrigation, multiple cropping cycles, fertilizer additions to croplands, and phenological or structural effects of different crops' growth phases, mean SIF values from agricultural areas do not show uniform spring and summer increases followed by declines in fall and winter. This difference may also have been driven by short agricultural growing seasons, which may not perfectly align with seasonal distinctions. Overall, SIF retrievals over agricultural lands are higher across all seasons, with a mean of 1.9 mW m^{-2} nm^{-1} sr^{-1} and a standard error of $\pm$ 0.32 mW m^{-2} nm^{-1} sr^{-1}, as compared to 1.2 $\pm$ 0.25 mW m^{-2} nm^{-1} sr^{-1} in forests and 1.7 $\pm$ 0.25 mW m^{-2} nm^{-1} sr^{-1} across all other biomes.

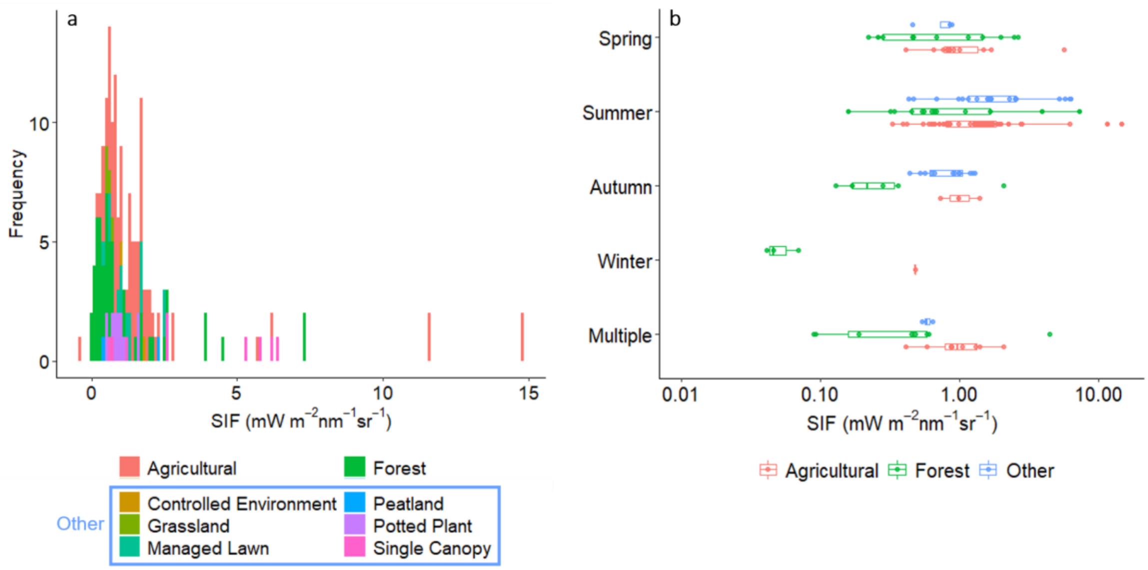

Figure 4. Variability in SIF Retrievals from Literature Meta-Analysis. Published mean far-red SIF retrievals from unstressed vegetation, as a histogram color-coded by vegetation type (a) and seasonal boxplots color-coded by simplified vegetation type categories (b). In panel b, the x-axis is plotted on a log scale to illustrate the wide range of variability and enhance detail in boxplots. Boxes show 25th percentile, median, and 75th percentile with lines extending to 1.5 times the interquartile range. The "Multiple" category in panel b indicates values reported at a scale that averaged or aggregated observations across multiple seasons.

In contrast to the strong SIF-GPP relationships observed at the satellite scale, mean SIF retrievals from tower and airborne relationships are not broadly predictive of the mean GPP values alongside which they were reported (Figure 5). Linear models of the SIF-GPP relationship show small positive slopes in non-agricultural areas, but none of these slope coefficients are statistically significantly different from zero for any land cover type. Additionally, R^2 values of 0.0015 for agricultural areas, 0.03 for forests, and 0.23 for all other land covers show that mean SIF is not significantly correlated with mean GPP across the studies examined here. It is worth noting that the mean values shown in Figure 2 represent data collected from a variety of targets and locations with varied processing and averaging strategies, instrumentation, and calibration methodologies. Figure S6b illustrates the number of corrections applied to the data shown in Figure 2.

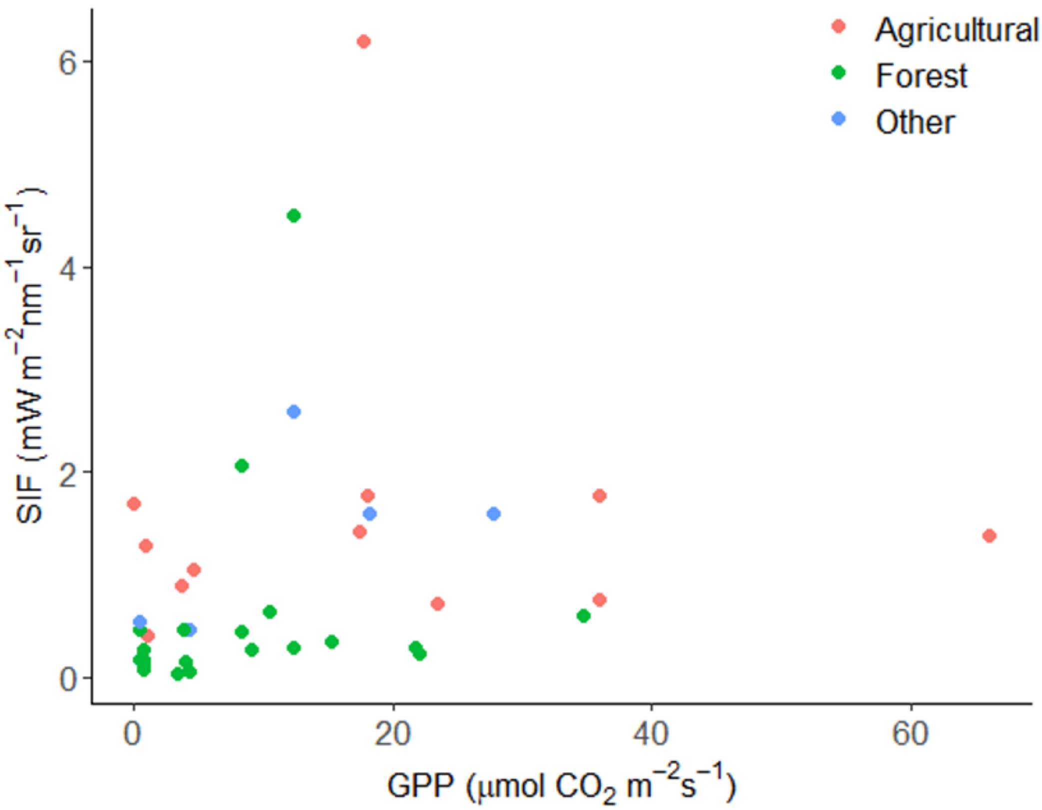

Figure 5. SIF-GPP Relationships. Mean far-red SIF from unstressed vegetation plotted against mean GPP measured from the same vegetated target. Points are color-coded by simplified vegetation type, as in Figure 1b.

Calibrations & Characterizations

Below, we describe several key sources of error in measuring spectra in laboratory and field settings, any of which may alter the final retrieved SIF signal. As a check on our system after calibration and corrections, we measured a Kautsky curve in order to confirm that physiologically meaningful signals matching leaf-level measurements could be recorded by our field instrumentation. The timing and relative magnitude of the SIF retrievals performed after exposing the dark-acclimated vegetation to light shows close agreement with steady-state fluorescence (F_s) measured at the leaf level, and indicate that our instrument deployment could capture the same fluorescence dynamics at a distance of 100 m as were seen with leaf-level instrumentation (see Figure S4 and Marrs et al., 2020).

One key challenge to reliable SIF measurements is the SNR of measurements of such a faint signal. In a laboratory setting, we found that, when measuring a stable light source (Figure 6a) without any fore-optics attached to the fiber optic cable, the SNR was greater than 1000 over the majority of the spectral range of our spectrometers (Figure 6b). The addition of the telescope decreased the SNR slightly, with a larger discrepancy observable in wavelengths > 700 nm. The attachment of a cosine corrector resulted in a large loss of signal, approximately halving the SNR of the spectrometer across the spectral range as a result of the attenuated signal.

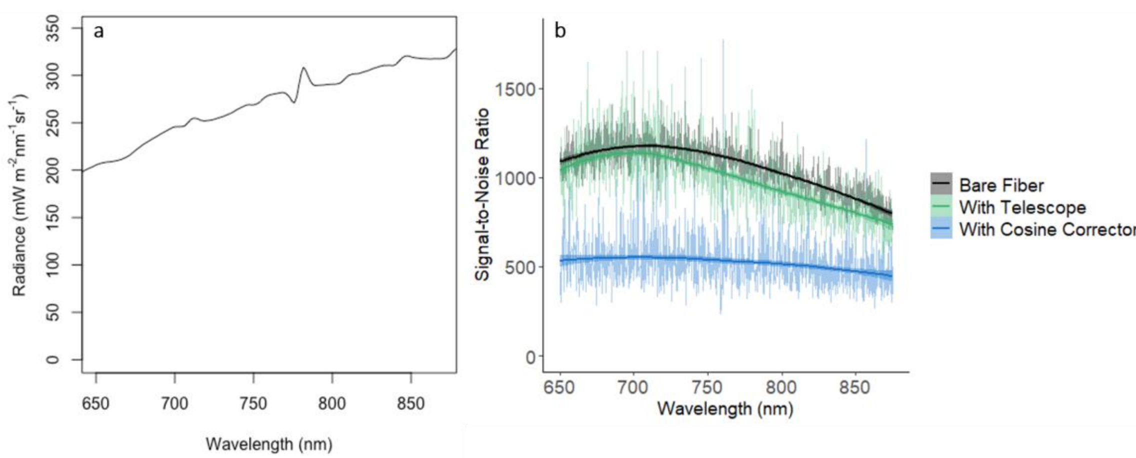

Figure 6. Laboratory Signal-to-Noise Ratios. Signal-to-noise ratios calculated from repeated measurements of a known radiance source (a), using a bare fiber optic cable, as well as telescope and cosine corrector fore-optics (b). Error ranges around smoothed loess lines in panel b represent the 95 % confidence interval.

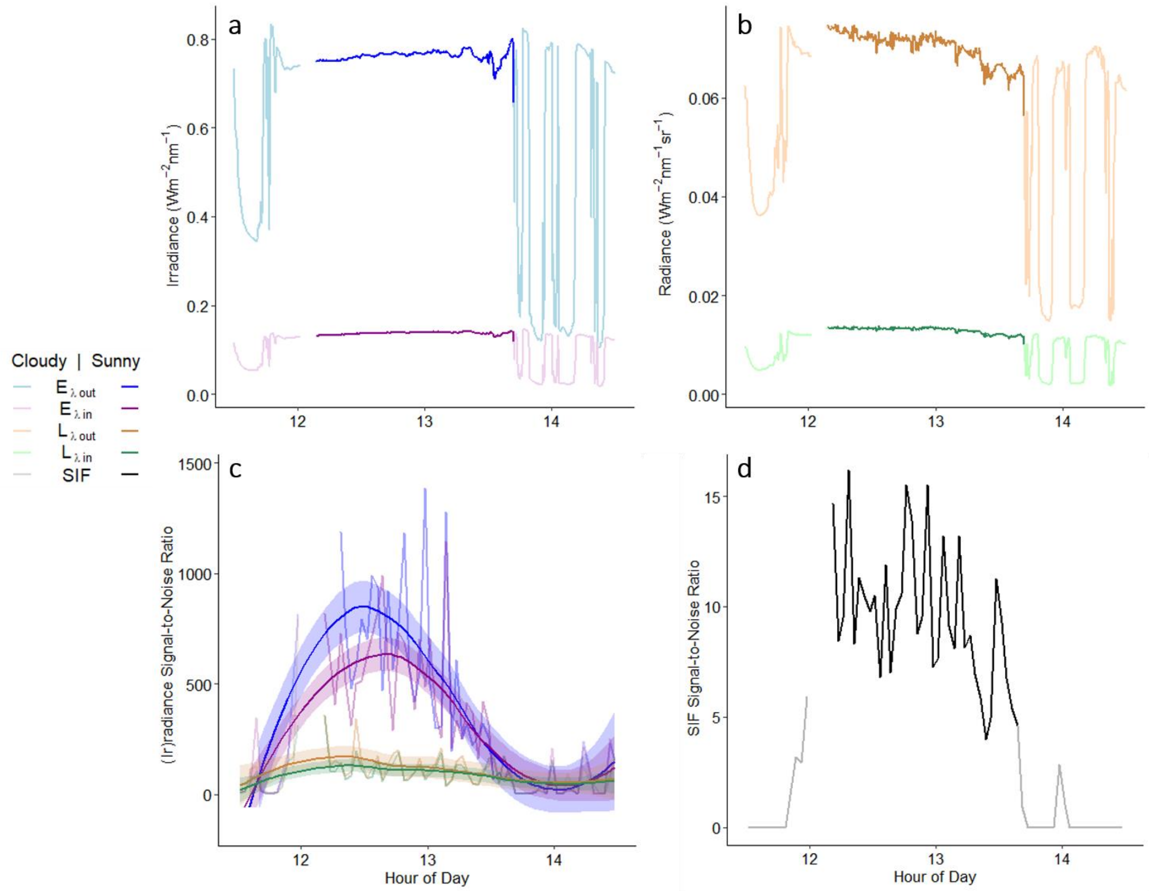

Figure 7. Field Signal-to-Noise Ratios. Three hours of continuous in-band (λ_{in}) and out-of-band (λ_{out}) irradiance (E) and radiance (L) measurements collected in a field setting are shown in panels a and b. Signal-to-noise ratios were calculated from 5 min intervals of these data (c) and of the resulting SIF retrievals (d). Error ranges around smoothed loess lines in panel c represent the 95 % confidence interval.

SNR values measured in field conditions are much more variable. Figures 7a-b show a time series of downwelling irradiance and reflected radiance measured continuously for three hours centered on solar noon (13:15 local time) on a day with intermittent cloud cover. Each panel shows radiance or irradiance measured both in and outside the O_2-A feature, wavelengths at which we expect to see very different signal magnitude due to atmospheric absorption effects. Figures 7c-d show these time series transformed into SNR values calculated at 5 min intervals. Irradiance measurements were collected every 1300 ms, so each SNR is calculated from the mean of 230 spectral irradiance values, divided by their standard deviation. Integration times for radiance reflected from relatively less bright treeline were 10 s, so 30 spectra are used to calculate each radiance SNR value. SIF retrievals are limited by the integration time of the radiance-measuring telescope system, so were also performed every 10 s and SNR was calculated as for radiance data.

During periods of clear skies, such as the period from approximately 12:10 to 13:40 local time shown in Figure 7, irradiance SNR values are nearly as high as in the laboratory. Despite slight atmospheric variability during this period, signal intensity from the sun is nearly three times as bright as the integrating sphere light source. In contrast, the cloudy periods immediately preceding and following these clear skies result in much lower SNR values. Although irradiance intensities are occasionally as high as during the clear sky period, the greater signal variability results in a larger standard deviation over a 5 min interval and a decreased SNR. Although they were collected with the same spectrometer and telescope configuration tested in the laboratory, radiance SNR values in the field are much lower. This is driven by the lower reflectance from the vegetated target at which the telescope was aimed. In this case, mean signal is low enough that overpassing clouds and resulting noise do not alter SNR values to the same degree seen with irradiance. All of this variability is commonplace in a field deployment, but is crucially important to retrieved SIF values. Over the course of this time series, the maximum SNR for 5 min of SIF retrievals was 16.2. These SNR values and those shown in Figure 7 are particular to our system and the illumination levels measured during our laboratory and field tests. While exact SNR values may vary in other tower-based systems, these results highlight the additional errors introduced in field settings beyond those characterized in the laboratory.

Laboratory characterizations of diffusive materials used in fiber-coupled cosine correctors show all materials tested here lead to underestimations of incoming light (Figure 8a). In our testing, opal glass outperformed either type of PTFE, but all materials show deviations from the theoretical cosine function expected in this kind of test. Discrepancies between expected and measured light intensities grow more extreme with simulated SZA, with errors of nearly 20 % from measurements at a simulated SZA of 60º using a Teflon diffuser (Figure 8b). Figure 8c shows the course of SZA values throughout high light hours of the day on five days within the typical growing season in Maryland. On 6 September, the date on which the time series in Figure 7 were collected, the highest SZA is 33.8º, with values up to 53.5º within three hours of solar noon. The use of an opal glass cosine corrector like the one deployed at our field site led to a 2 % to 8 % underestimation of downwelling solar irradiance, depending on the time of day (Figure 8d). Across all materials tested here, these trends hold true across wavelengths; small variations in deviation from theoretical values were observed across the in-band and out-of-band wavelengths relevant to FLD SIF retrievals (Figure S12). Measurements made at other times or days of year, or with other diffusive materials, will be associated with their own errors, which must be corrected in order to accurately quantify O_2-A in-filling and perform SIF retrievals.

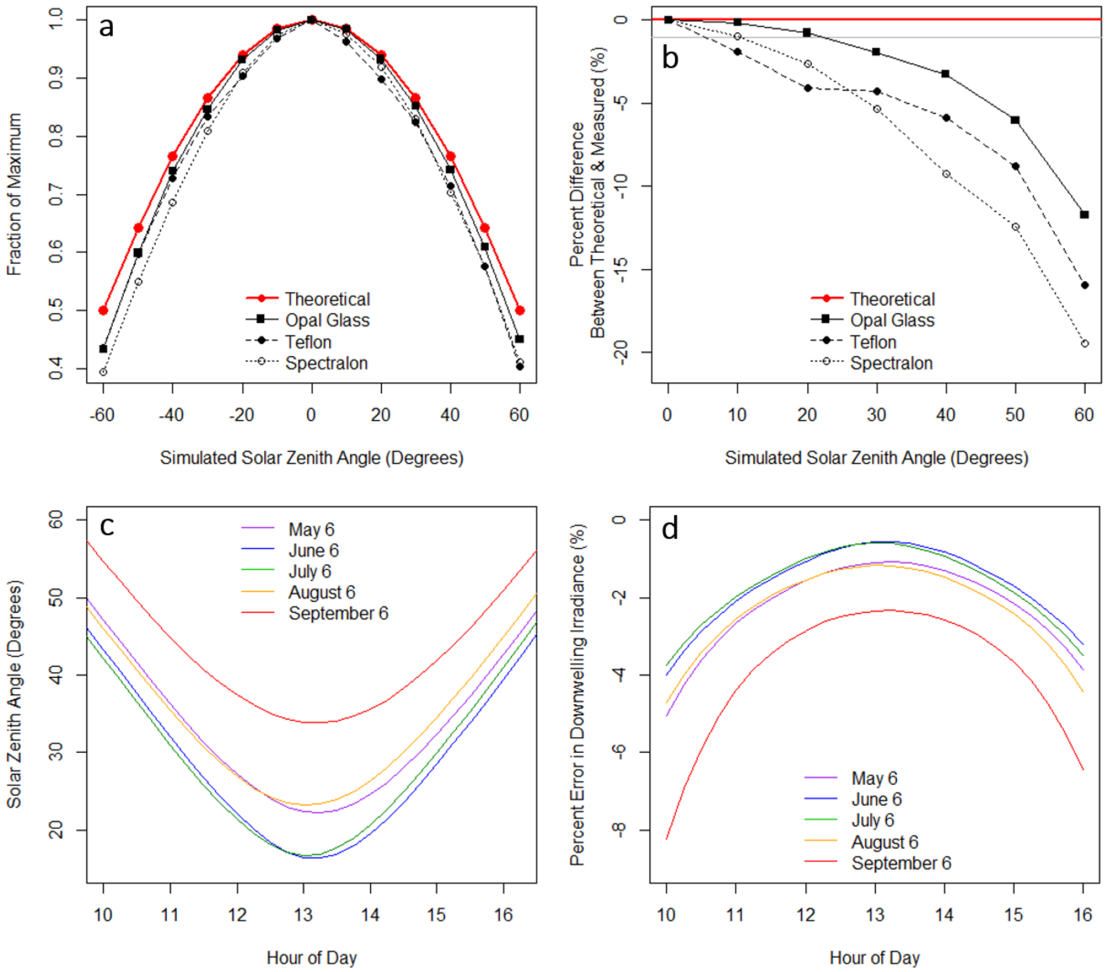

Figure 8. Cosine Corrector Effects. Diffusive materials were characterized in terms of the fraction of the light from a 1000 W FEL lamp each captured at ten degree increments away from center (a) and as the percent deviation from the theoretical cosine function used to predict the decrease in signal intensity at more extreme angles (b). Simulated solar zenith angles in the laboratory are related to true solar geometry over a field site throughout the growing season (c) in order to predict percent error in measured downwelling solar irradiance across time of day and year (d).

Quantifying Uncertainty in SIF Retrievals

A simulation of the uncertainties introduced by performing the above-discussed corrections demonstrates that the magnitude of and variability in SIF retrievals is highly dependent on calibrations and corrections applied to measured spectra. Depending on the time of day, the magnitude of retrieved SIF values changes with illumination level, sun angle, and environmental parameters. These changes are represented as the offset between the true SIF time series shown in Figure 9 and the solid lines corresponding to combinations of applied corrections and calibrations. The error ranges around these lines represent the uncertainties associated with the corrections themselves, as well as variability in detector noise. The size of each range is dependent on the error distribution and underlying assumptions used to generate it.

For example, the green line at the bottom of Figure 9 represents a scenario in which all corrections have been applied, except for atmospheric O_2-A absorption. Failure to apply this correction dramatically changes retrieved SIF; values are negative at all hours of the day, due to absorption of all chlorophyll fluorescence and some reflected radiance by atmospheric O_2. For this simulation, we assume that spectra were collected by spectrometers whose electronic dark signal and cosine corrector effects are known and corrected. Since the atmospheric correction was not applied in this scenario, errors associated with temperature, pressure, and relative humidity measurements are not introduced to this calculation. Thus, the only remaining uncertainty around these SIF retrievals is the small effect of detector noise, resulting in the small error ribbon around this line. In contrast, the peach-colored line representing a simulation in which no corrections are applied has a much larger associated uncertainty. In this 'No Corrections' scenario, it is not assumed that we know and can correct for electronic dark signal and cosine corrector effects. Instead, values for these parameters are drawn from error distributions, leading to wider ranges of uncertainty in resulting SIF retrievals. In the scenario where dark, cosine, and atmospheric corrections have been applied, the uncertainty around SIF retrievals is largest at solar noon, with a standard deviation of approximately ± 6.6 % around retrieved SIF values. This value represents the uncertainty in our field measurement system after applying all corrections discussed above.

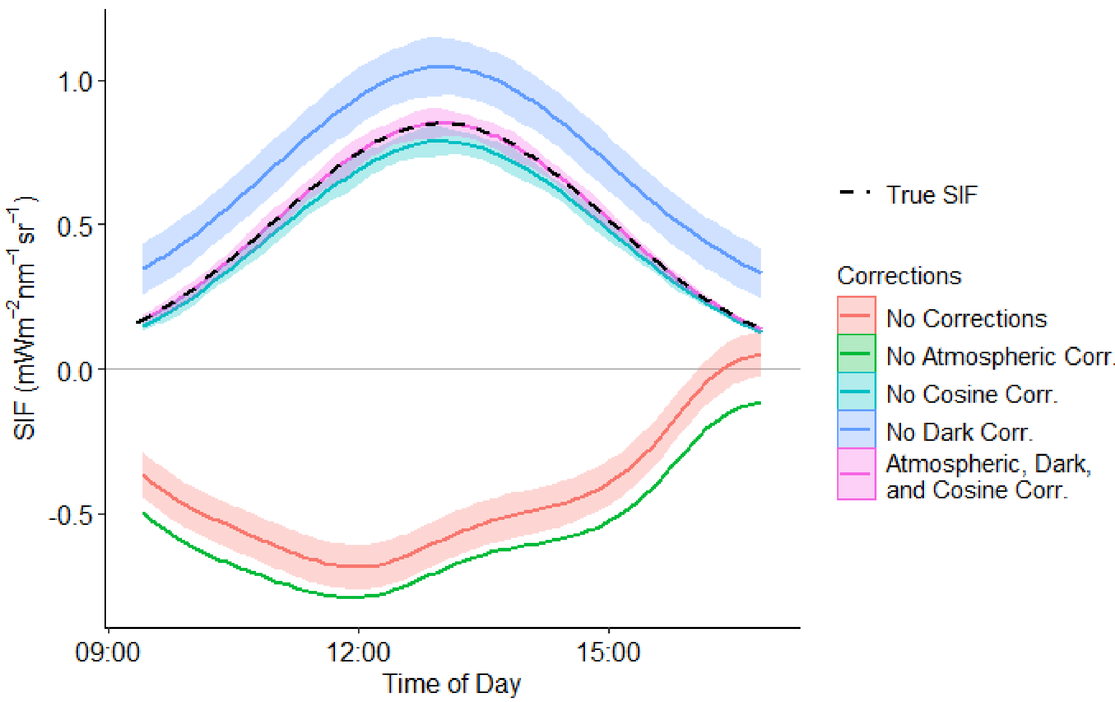

Figure 9. Uncertainty Estimation. True SIF (dotted line) values from a Monte Carlo uncertainty estimation are compared to SIF retrievals performed after applying different combinations of corrections (colored lines) and the uncertainties around these retrievals (colored error ribbons). Error ribbons represent ± 1 standard deviation.

The atmospheric correction applied in Figure 9 was calculated with the assumption of a 100 m distance between target and spectrometer (Table 2). However, the effects of atmospheric O_2 absorbance vary with path length, as well as with ambient temperature, relative humidity, and atmospheric pressure, as described in Sabater et al. (2018). Figure 10 shows the distance-dependence of atmospheric corrections at constant environmental conditions. Values were calculated using atmospheric conditions measured as closely as possible to solar noon on 6 September 2018; air temperature was 32.8ºC with 53 % relative humidity and 1.01 bars of atmospheric pressure. Along the 100 m from our telescope to the branch being measured at the treeline, approximately 9.5 % of the signal inside the O_2-A feature is lost. Since this is the exact spectral window in which the FLD method measures in-filling from SIF emission, this is a crucial consideration. The rug plot at the base of the curve in Figure 10 shows distances between instrumentation and target specified in papers in our meta-analysis. While some researchers are working at very short distances where atmospheric absorbance introduces very small errors, several papers describe SIF retrievals made from towers or small aircraft dozens or hundreds of meters from targeted vegetation, but do not discuss how this signal was corrected for atmospheric absorption along the path back to their instrumentation.

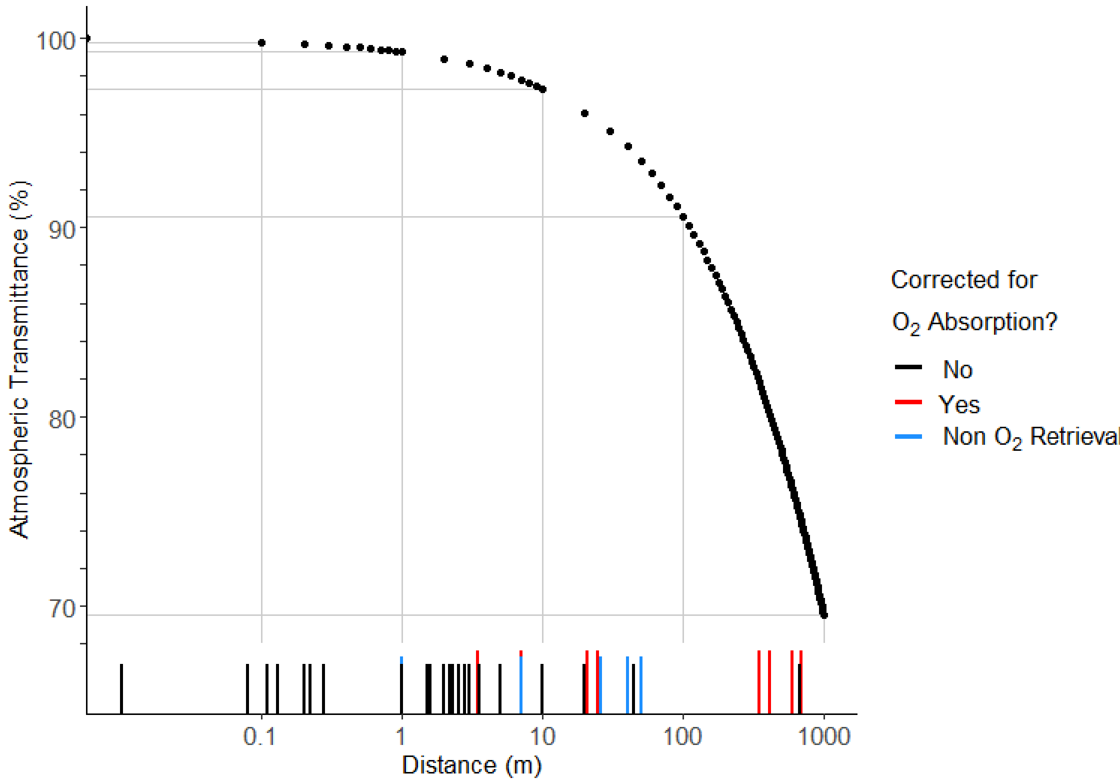

Figure 10. Effects of Atmospheric O_2-A Absorption. Points represent the decline in atmospheric transmittance within the O_2-A feature as path length between sensor and target decreases, as predicted by calculations from Sabater et al. (2018). Rug plot represents distances at which field measurements were made, as reported in papers from a literature meta-analysis. Rug plot is color coded to differentiate cases in which measurements were or were not corrected for O_2 absorption effects, as well as cases where correction was unnecessary because of SIF retrievals performed outside O_2 absorption features.

Discussion & Conclusions

Intermediate-scale SIF retrievals performed on unstressed vegetation under high-light conditions span a wide range of magnitudes. We have documented differences in hardware specifications, calibration methodologies, vegetation type, and retrieval methods, as well as environmental parameters, that are major drivers of the variability in these published SIF values (Table S1). An OSSE simulation of uncertainties introduced by calibrations and corrections applied during SIF retrievals shows that SIF magnitudes, and the uncertainties around them, may vary widely depending on correction methodology. The impact of applying these corrections when making SIF retrievals in the field is dependent on careful site characterization in terms of sun-sensor-target geometry, atmospheric conditions, and environmental variability. Instrument and hardware specifications play a similarly important role and must be characterized in field conditions in order to account for limitations to the insight that laboratory characterizations can provide about sources of measurement noise under real-world conditions.

For example, we see that SNR varies dramatically based on sky conditions, sun angle, and target illumination. This mismatch is important beyond simply revealing that controlled laboratory experiments have limitations: the larger SNR values measured in the laboratory suggest that we may have more confidence in our ability to measure the SIF signal than is truly merited in the field. The Mission Advisory Group for the European Space Agency's FLuorescence EXplorer mission state in a recent report (Moreno et al., 2015) that SNR of at least 1015 in wavelengths outside the O_2-A feature, and 115 within it, is necessary to reliably measure a faint signal like SIF. Of the 91 papers examined in our meta-analysis, only seven discuss SNR values specific to different wavelengths and/or integration times, indicating that many systems may be limited by greater uncertainties in SIF retrievals than laboratory characterizations would suggest.

Accessory hardware and fore-optics, such as cosine correctors, are another often overlooked but crucial source of error in SIF retrievals. Underestimations of downwelling irradiance may not be obvious when making measurements in the field, but we show that significant discrepancies between true and measured irradiance may be introduced by cosine correctors, especially at more extreme sun angles. The magnitude of underestimation depends on the diffusive material, and its implications when making SIF retrievals depend on the retrieval method employed. In the case of the FLD SIF retrieval method, a single correction factor accounting for solar zenith angle would be applied in both the numerator and denominator. This factor would thus cancel out, resulting in the same SIF value as before the correction. Small differences in correction factors for in-band and out-of-band wavelengths (Figure S12) are responsible for changes in retrieved SIF when using the FLD retrieval method. It should be noted that the results of our cosine corrector characterizations capture only the effects of diffusive material under direct illumination. We did not attempt to characterize additional effects of diffuse light, although other ongoing research has examined this important consideration (e.g. Chang et al., 2020a). Depending on the formulation of other retrieval methods, angle and wavelength dependence may affect final SIF retrievals to a greater or lesser degree. On the other hand, atmospheric O_2 absorption has a dramatic effect on measured SIF. Even the 100 m distance between our instrumentation and target introduced sufficient O_2 absorbance to mask all chlorophyll fluorescence emission before it reached the spectrometer. Both atmospheric and cosine corrector effects can be corrected post-measurement, but this requires careful characterization of sun-sensor-target geometry.

Broadly, our findings on the effects of hardware and instrumentation-associated uncertainties, namely those related to radiometric characterization and cosine corrector effects in a laboratory setting, are consistent with uncertainties modeled by Pacheco-Laborador and colleagues (2019). Our field results demonstrate that large errors can be introduced if atmospheric and angular corrections are not taken into account. It is likely that the varying implementation of these and other corrections across the published literature, along with differences in retrieval method, data filtering and averaging, and target type contribute to the wide range of published SIF values. Overall, the current SIF literature does not provide a clear consensus on SIF signal magnitudes or required instrument calibrations and corrections. Published SIF values vary beyond what might be expected from differences in species, season, or location. It is likely that the SIF instrumentation variability across the literature explains the lack of a strong relationship between mean SIF and mean GPP values at the tower scale. This finding stands in stark contrast to the close relationships observed at the satellite scale, where one set of carefully characterized instrumentation (per satellite platform) is used to make repeated measurements at a larger spatiotemporal scale that allows for linearization of the SIF-GPP relationship (Gu et al., 2019a). Nonetheless, more robust intermediate-scale SIF measurements are needed to make reliable inferences about photosynthetic rates or landscape-level primary productivity. Although important advances have been made in characterizing uncertainties within individual systems (Frankenberg et al., 2018; Grossmann et al., 2018; Gu et al., 2019b; Pacheco-Labrador et al., 2019), improvements are still needed, for example in developing improved atmospheric corrections for tower-based SIF retrievals. In the next steps of our work, we plan to continue characterizing stray light effects, following the methods described by Zong et al. (2006), as well as detector nonlinearity and temperature and humidity effects. Perhaps because of the difficulty of making such measurements, these are among the more frequently neglected corrections in the literature. In summary, there is a crucial need for best practice guidelines for characterization of spectrometers, hardware, and site characteristics in airborne and tower-based systems. Improving the reliability of intermediate-scale measurements will increase the utility of SIF as a parameter in models of primary productivity and help to further our understanding of methodologies to remotely monitor plant physiology.

CHAPTER FOUR: DRIVERS OF VARIABILITY IN SOLAR-INDUCED FLUORESCNECE AND LEAF-LEVEL ENERGY PARTITIONING ACROSS TEMPORAL SCALES

Abstract

Over the last two decades, observations of solar-induced chlorophyll fluorescence (SIF) have increasingly been used to constrain global models of terrestrial gross primary productivity (GPP), with strong, direct SIF-GPP relationships reported at satellite scales. However, the SIF signal originates from a pathway competing with photochemistry at the leaf scale, and thus the magnitude and sign the slope of the relationship between fluorescence yield (ΦF) : photochemical yield (ΦP) at the leaf level may change depending on environmental conditions. A recently developed camera-coupled spectrometer system (known as Cameron), capable of repeatable pointing to continuously monitor multiple targets, was designed to persistently measure SIF and the photochemical reflectance index (PRI) in order to enable investigations of dynamic energy partitioning among fluorescence, photochemistry, and energy dissipation as heat across temporal scales. Cameron observations capture a nonlinear, seasonally varying SIF-PRI relationship that persists even after controlling for canopy escape probability and seasonal-scale changes in daylength and maximum illumination. SIF and PRI also capture diurnal trends in energy partitioning regimes, as well as high temporal frequency variability in SIF retrieval magnitude associated with transient environmental effects such as cloud cover and wind speed. Complementary measurements of leaf-level gas exchange and leaf pigment content mirror these changes, suggesting that greater knowledge of leaf physiology and energy

partitioning offer the opportunity to enhance the utility of SIF-measuring platforms currently in orbit and better constrain models of GPP.

Introduction

The quantification of carbon (C) fluxes in and out of the terrestrial biosphere is central to understanding the current and future status of numerous human, ecological, and planetary processes (Le Quéré et al., 2018). However, challenges to direct measurements of such fluxes have resulted in large uncertainties surrounding terrestrial carbon fluxes in estimated global carbon budgets (Huntzinger et al., 2017; Rotach et al., 2014). These uncertainties arise in part because global models of gross primary productivity (GPP), or total C uptake by vegetation photosynthesis, show significant disagreement in their predictions due to insufficient data to fully constrain model outputs (Anav et al., 2015). Over the last two decades, observations of solar-induced chlorophyll fluorescence (SIF) have increasingly been used to address these data gaps. There have so far been seven SIF-measuring satellites launched, with multiple upcoming SIF-capable missions currently in progress (Ryu et al., 2019). Despite strong, direct relationships between satellite SIF retrievals and upscaled GPP model outputs (e.g. Sun et al., 2017), as well as flux tower GPP estimates across biomes (Verma et al., 2017; Xiao et al., 2019), there remain crucial questions regarding linearity in the SIF-GPP relationship across scales (Magney et al., 2020) and about the use of SIF to track leaf-level carbon assimilation at fine spatial scales (Helm et al., 2020; Marrs et al., 2020).

SIF-GPP Relationships

Typical models of remotely estimated GPP, such as that proposed by Monteith (1972) and shown in Equation 6, relate primary productivity to the amount of incident photosynthetically active radiation (PAR) that is absorbed by leaves (APAR) and the light use efficiency of photochemistry (ΦP), or the fraction of absorbed photosynthetically active photons which are used to power photochemical electron transport.

$$\text{GPP} = \text{APAR} \bullet \Phi\text{P} \tag{6}$$

Similarly, SIF can be formulated, as shown in Equation 7, as the product of APAR, light use efficiency of fluorescence (ΦF), or fraction of absorbed photons that are ultimately lost as fluorescent light, and the probability of an emitted SIF photon escaping the vegetation canopy to be measured by a sensor (f_{esc}) (Berry et al., 2013; Guanter et al., 2014; Yoshida et al., 2015).

$$\text{SIF} = \text{APAR} \bullet \Phi\text{F} \bullet f_{esc} \tag{7}$$

If we assume ΦF and ΦP to be proportional and to co-vary across time and environmental conditions, SIF must then exhibit a linear relationship with GPP. In many circumstances, this may in fact be true; numerous satellite-scale studies report direct, linear SIF-GPP relationships. Furthermore, recent work on canopy-scale SIF measurements shows strong relationships between SIF and APAR (Du et al., 2017; Miao et al., 2018; Wieneke et al., 2018), indicating that in these cases, APAR drives variation in SIF more so than changes in ΦF : ΦP. However, SIF originates from a set of competing biochemical and biophysical pathways by which energy absorbed by the leaves of illuminated vegetation is used in photochemistry or lost via alternative pathways, of which chlorophyll fluorescence is one (Baker, 2008; Porcar-Castell et al., 2014).

Energy Partitioning Dynamics

SIF competes with both photochemistry and the dissipation of energy as heat through a process mediated by carotenoid pigments of the xanthophyll cycle (Demmig-Adams and Adams, 2006). Because these multiple pathways compete for absorbed photons, the magnitude and sign of the slope of the ΦF : ΦP relationship at the leaf level may change depending on environmental conditions. Under low illumination, where photochemistry uses up the majority available photons before they can be lost as fluorescence, increasing ΦP leads to decreased ΦF. However, under moderate illumination conditions, ΦP may show a direct relationship with ΦF as surplus photons are lost as fluorescence or heat alongside high photosynthetic rate (Magney et al., 2020; Maguire et al., 2020; Porcar-Castell et al., 2008). Leaf-level energy partitioning dynamics may account for the non-linearity in the SIF-GPP relationship observed at finer spatial scales, but become less apparent when averaging over many observations, many angles, and/or areas of vegetation with differential illumination and physiological states (Gu et al., 2019a; Yao Zhang et al., 2018; Zhaoying Zhang et al., 2018). Thus, temporal and spatial scaling effects are crucial considerations when evaluating any SIF data. Even satellite SIF data from satellites with a finer spatial resolution, like Snapshot Area Maps (SAMs) from the Orbiting Carbon Observatory-3 (OCO-3) with a spatial resolution of approximately 3.5 km^2, exhibit high spatial variability, including over large areas of intact forest with homogeneous LAI, greenness, and productivity (see Figure 11). While some of the variability is likely related to canopy structural effects and to the inherent challenges of measuring the faint and dynamic SIF signal (Meroni et al., 2009), it is likely that energy partitioning dynamics contribute and should be considered.

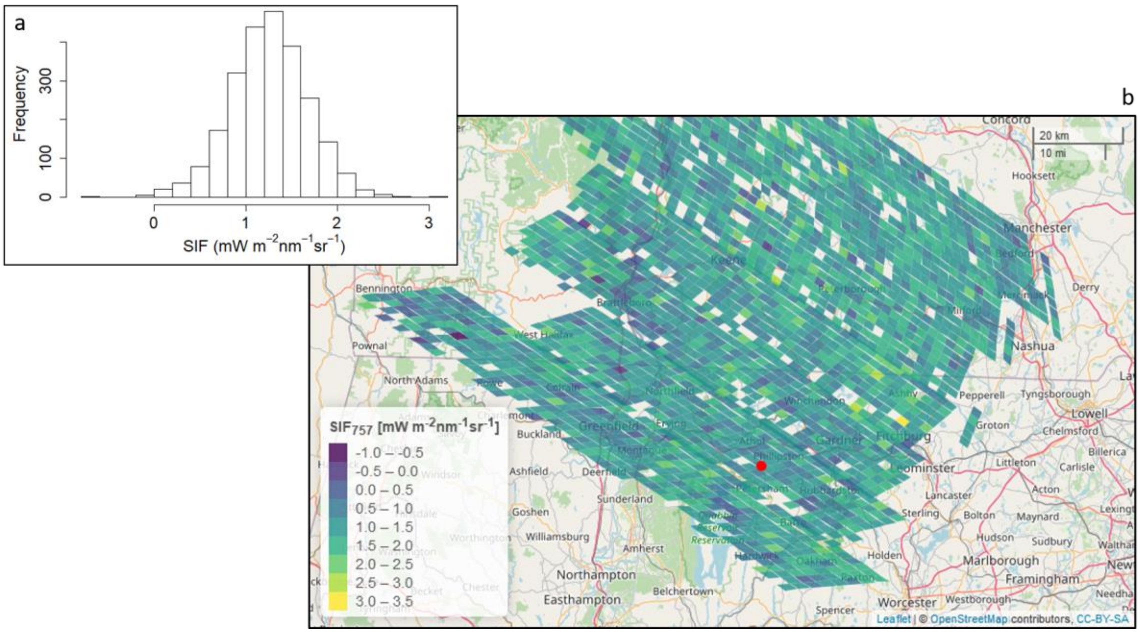

Figure 11. OCO-3 SAM covering the Harvard Forest. Panel b shows OCO-3 SIF retrievals from 20 August 2020, and panel a summarizes them as a histogram. Red dot in Panel b denotes the approximate location of the Harvard Forest.

Despite this variability, the SIF signal can be useful in predicting GPP; to contextualize SIF data and improve GPP models, it is critical to fully account for energy partitioning, including energy dissipated as heat. Use of the reflectance-based photochemical reflectance index (PRI) (Gamon et al., 1992), which provides insight into the thermal energy dissipation pathway that competes with both SIF and photochemistry for absorbed light, has been shown to improve SIF-GPP relationships across scales (Chang et al., 2020b; Middleton et al., 2016; Wang et al., 2020). SIF and PRI show dynamic responses to transient environmental changes, as well as diurnal variability and seasonal trends in response to other co-varying factors.

Low Temporal Frequency Variability

In addition to spatial gradients determining species composition and growth conditions for vegetation, leaf-level energy partitioning dynamics change over diurnal to seasonal temporal scales. Both SIF and PRI measurements vary over diurnal cycles (Campbell et al., 2019; Middleton et al., 2017; Paul-Limoges et al., 2018), with PRI generally showing positive correlations with ΦP (Cheng et al., 2013). At intermediate spatial scales, SIF and PRI have also been shown to vary with sustained nutrient (Watt et al., 2020) and water limitation (Alonso et al., 2017; Buddenbaum et al., 2015; Gerhards et al., 2018; Wieneke et al., 2018; Xu et al., 2018), providing insight into photosynthetic capacity during periods of stress. Likewise, SIF and PRI offer complementary information on phenological changes in energy partitioning (Liu et al., 2017; Nichol et al., 2019). Such seasonal trends are driven in part by the conversion state of xanthophyll cycle pigments, which play a key role in wintertime energy dissipation in evergreen species (Adams et al., 2004; Magney et al., 2019a), and in photoprotection in deciduous species during periods of leaf senescence and declining leaf chlorophyll content (Demmig-Adams, 1990; Demmig-Adams and Adams, 1992). These changes can be tracked using PRI data (Cheng et al., 2013; Middleton et al., 2017), which also offer insight into diurnal cycling in xanthophyll conversion with changing illumination (Evain et al., 2004; Paul-Limoges et al., 2018).

High Temporal Frequency Variability

In addition to the sustained changes described above, rapid xanthophyll conversions respond to dynamic adjustments in the instantaneous rates of absorbed energy usage across energy partitioning pathways; for example, changes on the order of seconds have been recorded in response to sunflecks transiently illuminating leaves in the forest understory (Adams et al., 1999). These changes, too, can be monitored with PRI, which exhibits rapid variability in response to brief shading events (Atherton et al., 2016; Evain et al., 2004). Remote measurements of vegetation canopies must be interpreted in the context of other causal or co-varying environmental factors. SIF shows distance- and retrieval method-dependent changes in response to shifting light intensity and to the proportion of direct : diffuse illumination (Chang et al., 2020a). In addition to rapid modulations with light intensity, field-measured PRI has been shown to be well correlated with diffuse illumination fraction (Jimenez et al., 2018). Increased wind speed and wind gusts often result in changes to branch orientation and leaf angle, altering within-canopy scattering and absorption effects (Van Wittenberghe et al., 2015). These considerations are doubly important given that wind events may expose to the sensor the abaxial sides (undersides) of leaves, which typically emit proportionally less SIF in red wavelengths and more SIF in near-infrared (NIR) wavelengths than do adaxial (upper) sides due to within-leaf re-absorption of red fluorescent photons (Atherton et al., 2016; Van Wittenberghe et al., 2013).

These considerations are particularly important for measurements made at small or intermediate spatial scales; the differential angle, illumination, and canopy position of each leaf within a satellite pixel integrating over a large area has far less impact on the value of the final SIF retrieval than it would on the value of SIF retrieved from a tower-based SIF system with a smaller field of view. For this reason, tower platforms present an ideal opportunity to investigate the leaf- and branch-level environmental and physiological drivers of variation in the SIF signal. The identification of such factors will provide insights into the mechanism by which SIF tracks GPP at larger scales and may help to identify additional parameters that can be incorporated into global productivity models in order to enhance the utility of existing satellite datasets.

A recently developed camera-coupled spectrometer system (known as Cameron), capable of repeatable pointing to continuously monitor multiple targets, was designed to investigate these factors. Spectra collected with the Cameron system enable SIF retrievals and the calculation of reflectance-based vegetation indices, and the corresponding camera images can be analyzed to quantify factors affecting vegetation (shadowing effects, canopy structure, fill factor, wind), and sky targets (sky condition, cloud cover). Here, we present data from a Cameron system deployed overlooking a vegetated area of Boston, Massachusetts. SIF and PRI data collected with Cameron were combined with leaf-level gas exchange and pulse amplitude modulated (PAM) fluorescence, data on leaf pigment content, stem-level sapflow measurements, and auxiliary data on environmental and illumination conditions. Our findings highlight several key ways in which the Cameron system offers the opportunity to examine SIF retrievals in the context of leaf-level energy partitioning and to improve the utility of the satellite record in tracking vegetation productivity.

Methods

Cameron Spectrometer System

The Cameron spectrometer system uses Ocean Insight QE Pro and Flame-S-VIS-NIR-ES (hereafter abbreviated to Flame) fiber-coupled grating spectrometers, identical to those specified for the widely used PhotoSpec system (Grossmann et al., 2018). Specifications for both spectrometers can be found in Table 4.

Spectrometer	**QE Pro**	**Flame**
Spectral Range	730 nm to 787 nm	350 nm to 1 μm
Spectral Resolution	0.07 nm	1.33 nm
Slit Size	200 μm	25 μm

Table 4. Cameron Spectrometer Specifications. Spectral range, spectral resolution, and slit size for QE Pro and Flame spectrometers.

In the Cameron system, the bifurcated fiber leading from the spectrometers was coupled to a 30 m, 400 μm core, multimode extension fiber. This fiber was then connected to an adjustable lens tube where it was fed by a Thorlabs AC508-150-B 2 in diameter achromatic doublet lens (Thorlabs Inc., Newton, New Jersey, United States). This lens had a focal length of 150 mm and an anti-reflective coating rated for 650 nm to 1050 nm. The optics were housed in an adjustable box mounted atop an AXIS Q8689-E PTZ-controlled security camera (AXIS Communications, Lund, Sweden). Once deployed in the field, the extension fiber was back-illuminated by a Thorlabs MINTF4 fiber-coupled light-emitting diode source, and the optics box was adjusted to align the center of the 0.7º spectrometer field of view with the center of the AXIS camera image. The spectrometers and fore optics were radiometrically calibrated using a Gooch & Housego 455-12U integrating sphere (Gooch & Housego PLC, Dowlish Ford, Illminster, United Kingdom).

Areas identified by PTZ coordinates were passed to the custom Python code used to run the Cameron system to specify a duty cycle of targets at which Cameron repeatedly pointed. Under sunny conditions, the Cameron system took less than 1 s to observe a vegetative target, however integration times could take as long as 1 min in the presence of dark clouds. The system was programmed to observe each target for a minimum of 30 s (or longer if needed for at least one full integration time), completing a cycle through all targets every 5 min to 10 min, depending on individual integration times. Photographs of the Cameron system and a representative image of vegetation fields of view can be found in Figure S13.

Cameron Data Processing

Data collected with the QE Pro spectrometer were processed following the differential optical absorption spectroscopy (DOAS) method (Grossmann et al., 2018; Stutz and Platt, 1996), focusing on the far-red SIF retrieval window spanning 729 nm to 784 nm. Spectra collected with the Flame spectrometer were used to calculate reflectance-based vegetation indices, using measurements of the white diffuser target as the reference spectra. Across all equations below, ρ indicates reflectance, meaning vegetation spectra normalized by reference spectra. Among these was PRI (Gamon et al., 1992), calculated as in Equation 7, which quantifies changes to the xanthophyll cycle pigments using reflectance values at 531 nm and 570 nm. PRI values range from -1 to 1 and show an inverse relationship with heat dissipation, becoming smaller or more negative as heat dissipation increases.

$$PRI = (\rho_{531} - \rho_{570})/ (\rho_{531} + \rho_{570}) \tag{7}$$

Recent work has demonstrated correlation between the near-infrared reflectance of vegetation (NIR_v) and f_{esc} (Kim et al., 2021; Zeng et al., 2019). Flame data were also used to calculate NIR_v by multiplying the normalized difference vegetation index (NDVI, calculated as in Equation 8) (Tucker, 1979) by total near-infrared reflectance (Equation 9) (Badgley et al., 2017), where ρ_{red} spans 620 nm to 670 nm and ρ_{NIR} spans 830nm to 860 nm.

$$NDVI = (\rho_{NIR} - \rho_{red})/ (\rho_{NIR} + \rho_{red}) \tag{8}$$

$$NIR_v = NDVI \cdot \rho_{NIR} \tag{9}$$

For easier intercomparison, SIF values and vegetation indices were aggregated to 15 min means in order to match the timestamps of the sapflow data. For most analyses, data were separated into two-week bins in order to showcase changes across the 2020 growing season.

Leaf-level Gas Exchange

Four healthy, intact leaves were selected for gas exchange on the first measurement day of the season, and were tagged for use in all subsequent measurements. Two leaves were on the lower left and two were on the lower right sides of the canopy, corresponding to the field of view of two targets monitored by the Cameron spectrometer system described above.

Gas exchange measurements were collected using a LI-COR 6800 photosynthesis analyzer with a 6800-01A fluorometer head and a PAR sensor. For all measurements, chamber CO_2 was set to 400 parts per million. Chamber temperature was set to approximately 1 ºC higher than ambient air temperature measured in the shade at ground level. Relative humidity was set to 60 %, except when high ambient humidity posed challenges to maintaining this level, in which case chamber relative humidity was increased to slightly below ambient levels. Chamber PAR was set based on a reading of ambient PAR at leaf height and angle; the LI-COR 6800 head was held at the angle of the leaf to be measured, slightly away from the canopy in order to prevent shadowing effects. Triplicate gas exchange measurements were collected for each leaf at each measurement time. Gas exchange measurements were made approximately bi-weekly over the partial growing season, at approximately solar noon (13:00 EDT). On 10 August 2020 and 3 October 2020, diurnal timeseries of gas exchange measurements were collected, starting pre-dawn (approximately 06:00) and ending when the tree was fully shaded by nearby buildings (approximately 16:30).

Leaf Pigment Content

Samples of leaf tissue were collected using a 0.5 cm^2 leaf punch at approximately the same time as leaf-level gas exchange measurements were collected, with the goal of collecting the punches under as near to identical PAR conditions as the gas exchange measurements. Immediately after collection, punches were sealed in aluminum foil envelopes and placed into a dewar of liquid nitrogen. Punches were transferred to a -80 ºC freezer immediately following the end of field data collection for the day. Leaf pigments were extracted from these stored samples in acetone according to Adams and Demmig‐Adams (1992) modified as described by de Viller et al. (2017). Following extraction, leaf pigments were quantified by high‐performance liquid chromatography (HPLC) as described by de Viller et al. (2017).

Sapflow

A ribbon-style sap flow sensor (Jones et al., 2020) was installed in the stem of the tree. These sensors work by injecting pulses of heat into the sapwood and tracking the advection of that heat by sap moving up the tree. Sensors were installed in August 2020 and operated until 15 October 2020. Sap flow measurements were collected every 15 min during this period.

Auxiliary Datasets

Data on environmental parameters including temperature, humidity, and atmospheric pressure were obtained using a Davis Vantage Pro2 weather station (Davis Instruments, Davis, California, United States) mounted on a roof approximately 100 m from the Cameron mounting site, and were supplemented by additional data from the Automated Surface Observing Systems monitoring station at Boston Logan Airport.

The AXIS camera records data in 3 visible-light channels, the red channel (RC), green channel (GC), and blue channel (BC). This RGB imagery was used to track sky condition using calculated blue chromatic coordinate (BCC, shown in Equation 10).

$$BCC = BC / (BC + GC + RC) \tag{10}$$

The mean (μ) and standard deviation (σ) in the BCC calculated for each pixel in the image were used to classify images into one of four sky conditions, as shown in Table 5. The red crosshairs overlaid on AXIS imagery are saved as part of the image, and so were removed before calculating BCC values. An example timeseries of sky images and sky condition classifications can be found in Figure S14.

Sky Condition	Mean (μ)	Coefficient of variation (CV)
Clear	μ >= 0.44	CV <= 0.1
Even clouds	μ < 0.44	CV < 0.06
Hazy	μ < 0.44	0.06 <= CV <= 0.096
Rolling Clouds	--	CV >= 0.096

Table 5. Sky condition classification thresholds. Sky condition category was assigned based on a combination of mean BCC and the coefficient of variation (CV = μ / σ) in BCC.

Statistics

Segmented models were fit to bi-weekly subsets of Cameron data using the segmented package in R (Muggeo, 2008). The segmented function was used to iteratively identify breakpoints in SIF and PRI data, and to create two linear models for each two-week subset data points, one on each side of the breakpoint. All settings within the segmented function were left as defaults. Before model fitting, outliers in 15 min aggregated data were removed. These outliers included SIF retrievals with non-physical negative values, seven SIF retrievals across the season that fell above an empirically determined threshold (0.35 W m^{-2} nm^{-1} sr^{-1}) and three additional SIF retrievals from within the time period between 20 August 2020 to 2 September 2020, which fell sufficiently far from all other points in this period to prevent satisfactory segmented model fits.

Phenological changes in leaf physiology co-vary with numerous other factors over seasonal timescale. In order to disentangle these effects, some data were transformed. For some analyses, we normalized our SIF retrievals by NIR_v in order to capture changes in f_{esc}. To rule out the possibility that changes in the slope of the SIF-PRI relationship were driven by declining maximum PAR intensity or shortening daylength over the course of the season, SIF and PRI data were filtered to include only those observations made between

10:00 and 16:00 (within three hours of solar noon at 13:00) each day. These filtered observations were further separated by PAR intensity at the time of observation (bins were defined as 500 μmol m^{-2} s^{-1} to 1000 μmol m^{-2} s^{-1} and 1000 μmol m^{-2} s^{-1} to 1500 μmol m^{-2} s^{-1}).

Results

Seasonal-scale Variability

We observed seasonally shifting non-linear relationships between SIF and PRI, captured by segmented linear models (Figure 12). Across all weeks, observations collected under low-light conditions show variable PRI and near-zero SIF, falling into the lower, shallower slope shown on each plot. Observations collected under moderate and high light conditions are captured by the upper slope of each model. Across the course of the growing season, these slopes became increasingly negative. Additionally, PRI values shifted toward smaller and more negative values over the course of the season. During high light hours, SIF and sapflow data generally showed a direct correlation. After normalizing SIF data by NIR_v to account for changes in f_{esc} across the season, no changes were observed in point clustering or SIF-PRI relationship slopes over the season (Figure S15). When examining midday observations binned by PAR value at the time of observation, the trend in changing SIF-PRI slopes over the course of the season again persisted (Figure S16).

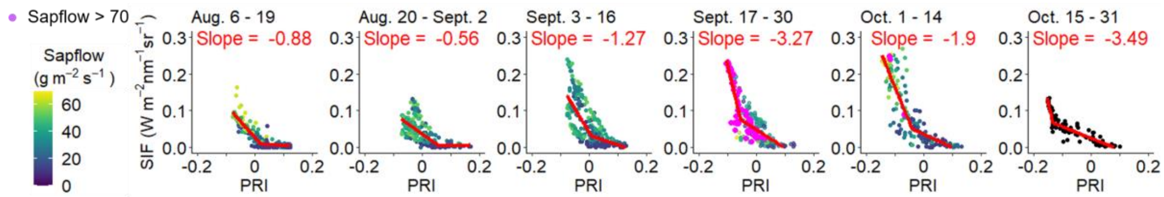

Figure 12. SIF-PRI relationships. SIF and PRI data from the 2020 growing season, aggregated to 15 min intervals. Measurements are separated into two-week bins to highlight the changing slope of the SIF-PRI relationship during high light hours. Red lines indicate segmented models fit to SIF and PRI data. Slopes printed in red indicate the slope of the uppermost portion of each segmented model. Point color ramp indicates sapflow value, and magenta points indicate sapflow values higher than 70 g m^{-2} s^{-1}.

Leaf chlorophyll concentrations quantified from leaf punches declined steadily over the course of the growing season (Figure 13a). The mild temperatures in fall 2020 corresponded to persistent leaf greenness until the first snow of the season on 30 October 2020. Leaves senesced quickly after the snowfall. Chlorophyll concentrations at the end of the growing season were roughly 50 % of the maximum observed value from August 2020. Leaf zeaxanthin content per unit chlorophyll remained nearly constant in August and September, then increased abruptly at the beginning of October (Figure 13b).

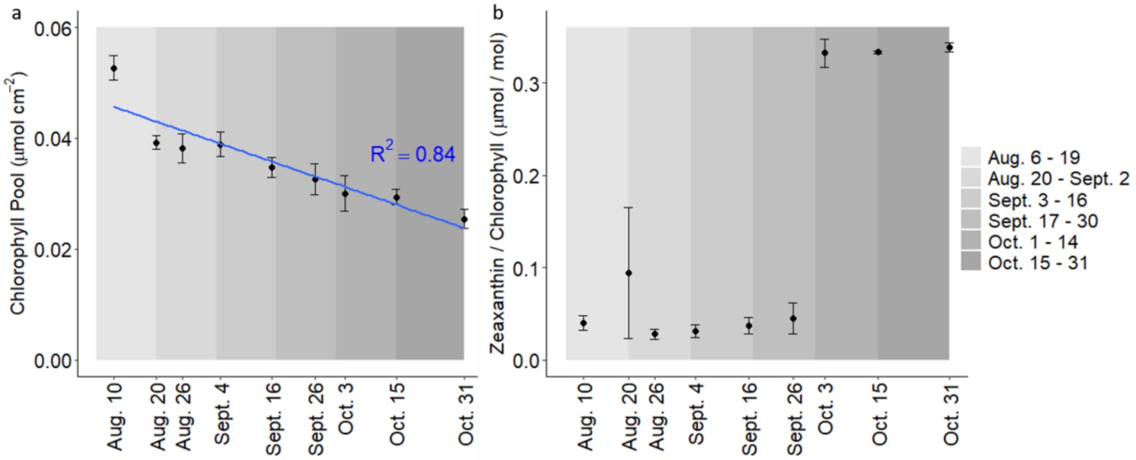

Figure 13. Leaf pigment content. Error bars represent standard errors around mean values from *n* = 4 leaves per time point. Blue lines represent linear models of change in pigment content by day of year, and the R^2 value printed in panel a was significant ($p < 0.05$). For ease of comparison, background color corresponds to the two-week bins used to separate data in Figure 1.

Diurnal Variability

The BCC-based cloud cover index revealed clustering of points based on sky condition, with many clear-sky observations showing higher SIF and NIR_v with lower PRI values than those collected during evenly cloudy or hazy conditions (Figure 14). Within the clear-sky observations, however, a subset showed the opposite trend: lower SIF and NIR_v alongside higher PRI values. These two clusters represent distinct energy partitioning regimes. The observations with higher SIF retrieval values (Cluster A), were generally taken during midday and, since they were all collected during clear-sky conditions, under higher PAR conditions (Figures 14c-d). In contrast, observations that fell into the other cluster (Cluster B) were collected exclusively during early morning or late afternoon, with lower incident PAR.

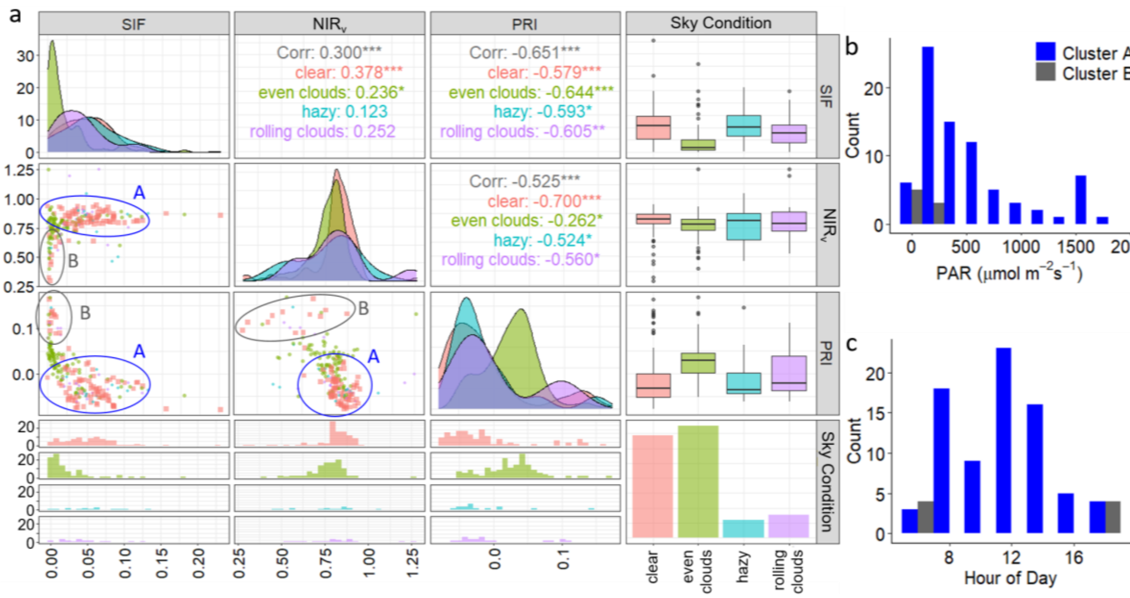

Figure 14. Point clustering by sky condition. Panel a shows pairs plots, density plots, histograms, and box plots summarizing distributions of NIR_v, SIF, and PRI data categorized by sky condition. Circled points indicate the clusters examined in panels b and c. All data shown here are from a representative 2-week time period (20 August 2020 to 2 September 2020).

Similar patterns can be found in PAM fluorescence data, all of which were collected simultaneously with leaf-level gas exchange data, on days with as clear skies as possible. While the majority of PAM fluorescence data were collected during the midday spot measurements, the two diurnal campaigns provided additional data from low-light hours in the early morning and late afternoon. In order to examine energy partitioning dynamics over these changing light conditions, ΦPSII was used to represent ΦP, and F_s, normalized to maximum F_s value on the day of measurement as by Maguire et al. (2020), was used to represent ΦF (Figure 15). Slopes from linear models fit to the PAM fluorescence data show a positive slope in high light conditions (PAR > 400 μmol m^{-2} s^{-1}) and a negative slope under low light conditions (PAR <= 400 μmol m^{-2} s^{-1}).

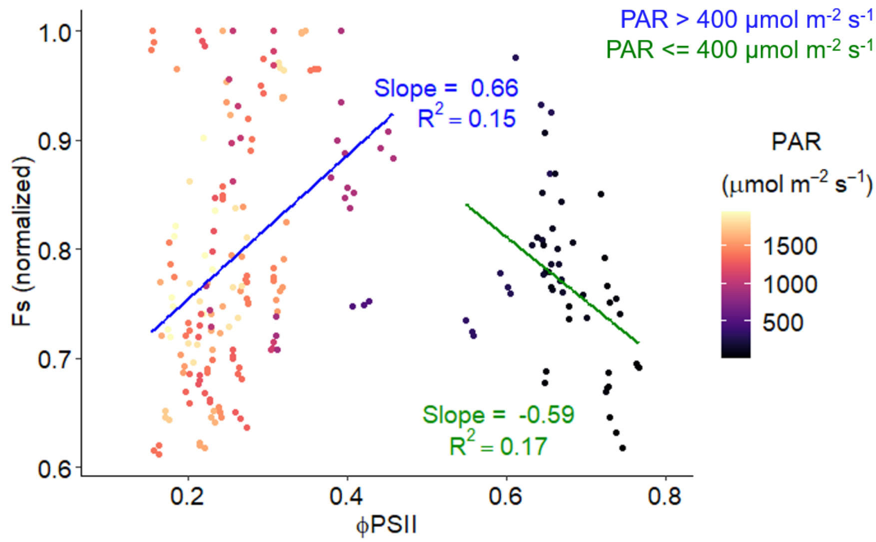

Figure 15. PAM fluorescence data. Light use efficiency of PSII (ΦPSII) and steady-state fluorescence (F_s) normalized by maximum F_s on the day of measurement are shown. Slopes from linear models fit to data collected during high light conditions (blue slope) and low light conditions (green slope). Both slopes were significant (p < 0.05). Point color ramp shows PAR at time of measurement.

High Temporal Frequency Variability

A subset of SIF retrievals were unexpectedly low on 30 September 2020. These data included SIF retrievals corresponding to high sapflow values and midday hours, typically a period when higher SIF values were observed (circled in magenta in Figure 16a). These observations were collected during a windstorm, with mean wind speeds of 10.4 m s^{-1}, in comparison to a mean of 3.87 m s^{-1} on the day preceding the storm (Figure 16b). Cameron images collected during the windstorm revealed that the high winds exposed the abaxial side of many leaves within the field of view; a representative image can be seen in Figure 16d, which clearly shows the differential reflectance from abaxial sides of these silver linden leaves, as compared with the image collected under typical winds, shown in Figure 16c.

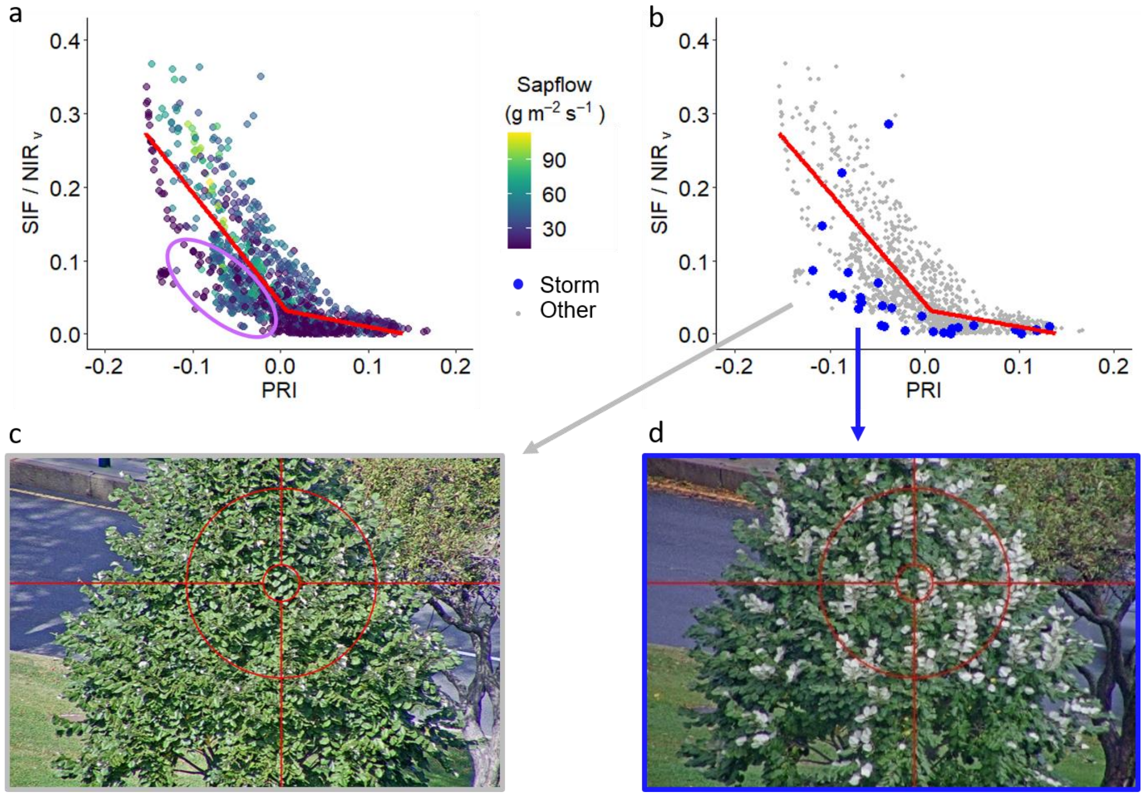

Figure 16. Effects of high winds. Panel a shows the full season of SIF retrievals, normalized to NIR_v, as well as PRI data, aggregated to 15 min intervals. The color ramp represents sapflow measurements. Magenta circle indicates points with relatively high sapflow, observed during midday hours, but which nevertheless show lower SIF / NIR_v than expected. Panel b highlights points in blue during a windstorm on 30 September 2020. Panels c and d show representative Cameron images of the silver linden tree before the storm on 29 September 2020, and during the wind storm, respectively.

Discussion

Seasonal-scale Trends

Cameron observations capture a nonlinear, seasonally varying SIF-PRI relationship. Across the study, the shallower slope on the lower range of the y-axis is associated with measurements made in low light conditions, including early mornings, late afternoons, and periods of heavy cloud cover. The upper, steeper slope of each segmented model captures higher-light observations, and variations across the season are suggestive of changes in the energy partitioning pathways underlying measured SIF and PRI. However, a number of other potential drivers co-vary along the same seasonal timescale. From August to October, many deciduous trees begin to lose leaves, leading to changes in branch and canopy structure, and thus to altered f_{esc}. However, the nearly-identical distribution of raw SIF retrievals and SIF retrievals normalized by NIR_v (Figure S15) demonstrate that no such effects were observed during the mild fall of 2020. This finding is supported by Cameron imagery of the targeted vegetation, which shows no significant declines in leaf fill within the field of view. Changes in the slope of the SIF-PRI relationship also persist after controlling for maximum PAR and daylength, which vary over the same time period (Figure S16), indicating that these changes are not solely the result of illumination changing with time of year.

Given that these changes persist even after controlling for relevant external effects, changes in SIF-PRI slopes, as well as the increasingly negative PRI data over the course of the season, suggest changing leaf physiology and altered energy partitioning as the drivers of this phenomenon. The results of HPLC analyses of leaf pigment content support this hypothesis. Steady declines in leaf chlorophyll pool size over the course of the season (Figure 13a) indicate a gradual loss of leaf photosynthetic capacity, reducing photochemical yield during high-light hours. With a declining capacity to utilize absorbed photons for photochemistry, leaves experience a greater need for photoprotection. Figure 13b shows an increase in the zeaxanthin : chlorophyll ratio that corresponds with the timing of the greatest increase in SIF-PRI slope from Figure 12 around the beginning of October 2020. The dramatic increase in zeaxanthin : chlorophyll ratio suggests that novel zeaxanthin synthesis, in addition to loss of chlorophyll, may have driven the changes in energy partitioning we observed remotely.

Diurnal Variability in Energy Partitioning

In addition to the broader, seasonal trends in observed in SIF and PRI due to this gradual (low temporal frequency) change in energy partitioning, Cameron data revealed diurnal variations in SIF, PRI, and NIR_v. Categorizing points by sky condition helps to explain clustering of observations in the context of underlying energy partitioning dynamics. Clear-sky observations from midday hours (like those shown in Cluster A from Figure 14) come from irrigated and well-illuminated vegetation, where the predominant factor limiting plant productivity is the rate of photochemistry. This is consistent with the higher SIF and lower PRI values, indicating the engagement of alternative pathways to dissipate absorbed photons not used to power photosynthesis. However, during low-light hours (as shown in Cluster B from Figure 14), vegetation is likely light-limited, with a greater proportion of absorbed photons being used in photochemistry, and fewer being lost as heat or fluorescence. During these low-light hours, more extreme solar zenith angles and higher proportions of diffuse illumination may help to explain the much larger variability in NIR_v than in SIF or PRI.

Similarly, different regimes capturing variability in PAM fluorescence data can be separated out by illumination levels. Figure 15 resembles a conceptual diagram presented by Magney et al. (2020), as well as other researchers' field-collected data on photochemical and fluorescence yields (Maguire et al., 2020; Porcar-Castell et al., 2014, 2008). These leaf-level data complement remote measurements made with the Cameron system, and suggest that SIF and PRI data collected with this system are in fact capturing energy partitioning dynamics at the branch scale.

High Temporal Frequency Variability

Environmental effects that may vary over short time scales, including illumination and wind speed, capture additional variability in SIF, PRI, and NIR_v data. Many SIF observations that were unexpectedly low correspond to periods of wind-mediated change in leaf orientation, leaf reflectance, and branch structure. Although this effect was discovered only during the data processing stage of this analysis, and thus the exact mechanism of this effect could not be examined in detail, the silvery undersides of leaves blown back toward the rest of the canopy may have emitted fewer fluorescent photons than the typically measured adaxial side, or may have differentially scattered incident radiation before it could be absorbed. Cameron images also reveal that high winds caused changes to branch orientation and overall canopy structure, likely altering within-canopy SIF scattering and f_{esc} during this period. Contrary to the results seen over the rest of the season, SIF / NIR_v values did show differential distribution than SIF alone during these periods of high wind, and are thus used in Figure 16 to provide additional insight into these factors. Aside from structural explanations, it should also be noted that the many of the sapflow values above 70 g m^{-2} s^{-1} also correspond to the period of this windstorm, likely due to changes in the leaf boundary layer under high winds. Thus, it is possible that altered energy partitioning due to this increased ΦP could explain the lower SIF values recorded during the wind storm.

Conclusions

The majority of the satellite-scale SIF-GPP relationships reported in the scientific literature are derived from sun-synchronous SIF-measuring satellites, which have overpass times in the late morning or early afternoon, and typically only retrieve and report SIF values collected under minimal cloud cover. This measurement regime, while necessary for the temporal continuity of satellite datasets, means that satellites are limited in their ability to represent leaf-level productivity and energy partitioning under other environmental or illumination conditions. Some researchers find strong relationships between SIF and primary productivity measured from individual towers or drones after temporal aggregation (Magney et al., 2019a; Yang et al., 2017; Zarco-Tejada et al., 2016). However, when looking across the intermediate-scale literature, published mean SIF retrieval values span several orders of magnitude and do not show significant relationships with mean GPP values measured from the same sites (Marrs et al., 2021). This wide range of variability indicates that, in addition to instrumentation and measurement challenges inherent in capturing a faint and temporally dynamic signal, there likely are structural, temporal, and environmental factors that are not being taken into account.

Here, we add to a growing body of literature illustrating the utility of PRI data in improving intermediate-scale SIF-GPP relationships by more fully capturing the underlying energy partitioning controls on ΦF, ΦP, and the non-linear relationship between them. Data presented here illustrate that the Cameron system is capable of capturing these dynamics at small spatial and temporal scales, and suggest that the insights provided by combining data on SIF, PRI, canopy structure, and primary productivity are crucially important to enhancing the utility of SIF datasets across spatiotemporal scales. For example, these factors may help to contextualize and interpret the heterogeneity in SIF retrieved from satellites like OCO-3 (Figure 11), with finer spatial resolution and variable measurement times and angles. In heat and moisture stressed regions, as well as highly fragmented urban landscapes, SIF-GPP relationships may be even more prone to non-linearity (Helm et al., 2020; Marrs et al., 2020; Parazoo et al., n.d. in press; van der Tol et al., 2014), indicating that a greater knowledge of energy partitioning dynamics offered by a synthesis of SIF and PRI offers the opportunity to enhance the utility of SIF-measuring platforms currently in orbit and better constrain models of GPP.

CHAPTER FIVE: CONCLUSIONS

The strong relationships between satellite-scale SIF and GPP have captured the interest of the carbon cycling community (Mohammed et al., 2019; Ryu et al., 2019), and SIF has often been described as a proxy for photosynthesis (Yang et al., 2015; Yongguang Zhang et al., 2018). Findings from the PAM fluorescence literature, however, demonstrate that chlorophyll fluorescence is just one part of the complex biophysical processes involved in leaf-level energy partitioning, and that the universal assumption of a linear SIF-GPP relationship would be an oversimplification in many cases. In my first chapter, I explored this apparent contradiction by examining measurements collected from experimentally manipulated tree branches, finding that SIF retrievals did not track the significant alterations to leaf-level A_{net} and energy partitioning induced by our experimental treatments (Marrs et al., 2020). Results from this experiment suggest that, if used as a standalone parameter for monitoring changes in primary productivity as is typically done at the satellite scale, SIF data would not have provided sufficient insight into alterations in leaf-level C assimilation and energy partitioning. While this result stands in contrast to findings at the satellite scale, the two interpretations of the SIF signal are not necessarily contradictory; they simply emphasize the need for additional knowledge of energy partitioning and environmental factors surrounding the use of SIF data to monitor and predict primary productivity.

There remain several plausible mechanisms that may explain why SIF could be linearly related to GPP at large spatiotemporal scales but exhibit a non-linear relationship with primary productivity at finer scales. It may be the case that many intermediate-scale measurements, including those made in my first chapter, are limited by the temporal mismatch between stress responses seen in the SIF signal and those seen in leaf physiology (see Figure 1c, Magney et al., 2020). It is also possible that strong SIF-GPP relationships at larger scales may be the result of their shared driver, APAR (Du et al., 2017; Miao et al., 2018; Wieneke et al., 2018), which may drive the broad trends in variability of ΦF and ΦP that can be captured at the satellite scale. Finally, discrepancies in the direction and strength of SIF-GPP relationships across scales may be an artifact of the sun-synchronous orbit of most SIF-measuring satellites, which collect SIF data only at midday and under clear sky conditions, where ΦF and ΦP are directly correlated (Magney et al., 2020). During low-light conditions, where photochemistry and fluorescence more directly compete for photons, ΦF and ΦP show in inverse relationship. Thus, non-linear SIF-GPP relationships found from platforms that measure across illumination conditions may simply be capturing a more complete picture of SIF-GPP relationships, rather than contradicting satellite-scale findings.

SIF retrievals made at finer spatial scales, such as from tower and airborne platforms, are complicated by additional considerations, including environmental and hardware-related sources of variability in recorded spectra. My second chapter regarding the sensitivity of the SIF signal to instrumentation and calibration effects suggests that the challenges of measuring faint and temporally dynamic variations of SIF in a field setting may contribute to the lack of clarity in SIF-GPP relationships at intermediate scales (Marrs et al., 2021). The diversity of field-deployed instrumentation and associated hardware, particularly cosine correctors used to measure downwelling irradiance, as well as variability in the accuracy of laboratory calibrations and corrections, may serve to obscure otherwise informative trends in SIF measured at intermediate scales. The findings from our field and laboratory calibration work, as well as from a meta-analysis of published papers on SIF data collected at intermediate scales, point to the urgent need for standardization in field-deployed instrumentation types and in the calibration and characterization of these sensors and associated hardware. Sensor intercomparison campaigns should become a priority for the SIF community, and would have the double benefit of enabling comparisons among the many field sites now collecting data and of enhancing the utility of these sites for ground validation of satellite SIF retrievals.

Though the detectors and hardware used for SIF measurements in the field greatly contribute to variability in absolute SIF retrieval magnitude, the OSSE simulation run in my second chapter showed that the largest single source of uncertainty among all factors tested was the correction for atmospheric O_2 absorption. The atmospheric correction depends on SIF retrieval method and distance between target and sensor, but also on ambient temperature, humidity, and atmospheric pressure, and thus this finding demonstrates the importance of environmental variability when measuring SIF in field settings. This is consistent with many of the results presented in my third chapter, where transient environmental effects such as cloud cover and wind speed exerted a great deal of influence over retrieved SIF values. Interpretation of the variable SIF values retrieved over the 2020 growing season was aided by including PRI data, which capture information on heat dissipation via the xanthophyll pigment cycle and allow for a fuller picture of leaf-level energy partitioning dynamics. SIF-PRI relationships varied on diurnal and seasonal timescales, and findings from leaf-level gas exchange measurements and leaf pigment content quantification suggested that seasonally shifting energy partitioning dynamics, along with environmental variability on shorter temporal scales, drove these changes in our remotely sensed measurements. These findings make a clear case for the necessity of contextualizing tower-based SIF measurements within knowledge of environmental conditions at the time of measurement, a factor which likely contributes to heterogeneity in SIF retrievals within single satellite overpasses.

Satellite SIF measurements offer useful physiological information and great promise for improvements to global GPP modelling efforts. In order to take full advantage of SIF data to create more reliable models of global productivity, it will be necessary to better characterize the spatiotemporal boundaries required to relate a leaf-level phenomenon like chlorophyll fluorescence to global estimates of productivity. Some currently operating satellite platforms may be useful in this effort. For example, the Deutsches Zentrum für Luft- und Raumfahrt (DLR, meaning German Aerospace Center) Earth Sensing Imaging Spectrometer (DESIS) is a hyperspectral satellite platform currently deployed on the International Space Station (ISS), measuring in the wavelengths needed to calculated PRI. Similarly, the Ecosystem Spaceborne Thermal Radiometer Experiment on Space Station (ECOSTRESS) satellite, also currently measuring from the ISS, provides thermal measurements that may be useful in characterizing plant water stress. Such satellite data must be paired with data collection and synthesis at finer spatiotemporal scales in order to obtain a fuller picture of energy partitioning on the ground, and SIF retrievals across scales should be interpreted in the broader context of biological and environmental controls. SIF offers tremendous promise for improving the characterization of terrestrial carbon exchange, and a fuller understanding of the boundaries on its utility and interpretation will help to enhance the utility of SIF-measuring platforms currently in orbit and create more reliable models of global productivity.

APPENDIX A: SUPPLEMENTARY FIGURES

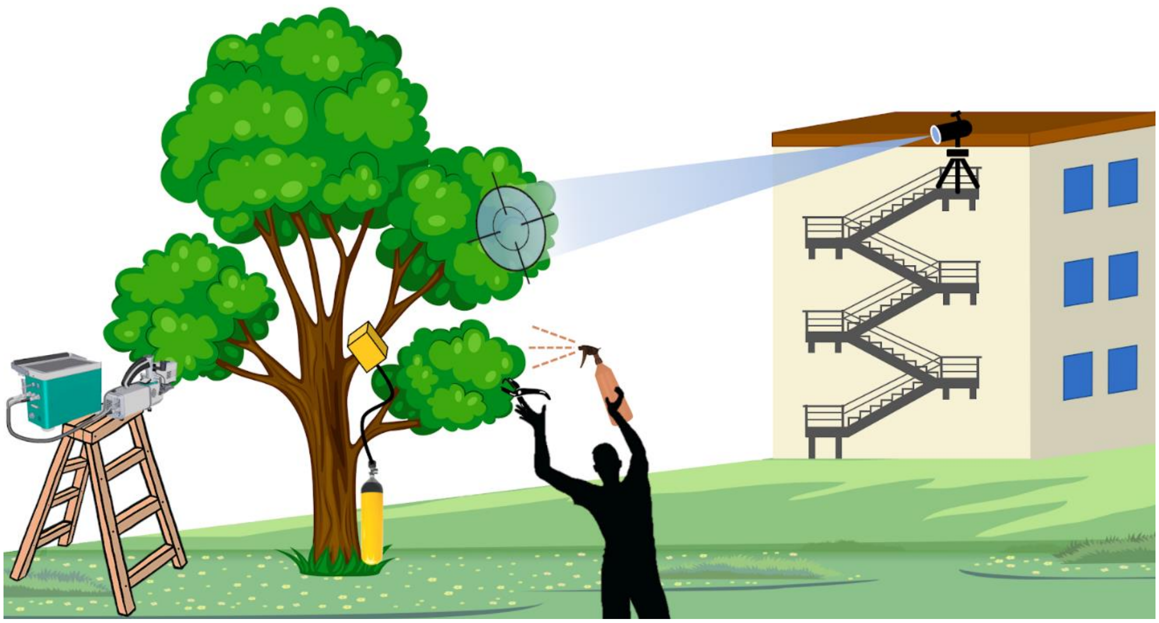

Figure S1. Experimental Design Schematic. Schematic shows approximate geometries for remote SIF measurements on a sample tree on the FOREST treeline, with three neighboring branches being pressurized, ABA-treated, or left as control. Leaf punches for pigment characterization, and LI-COR 6800 measurements of gas exchange and PAM fluorescence parameters are represented.

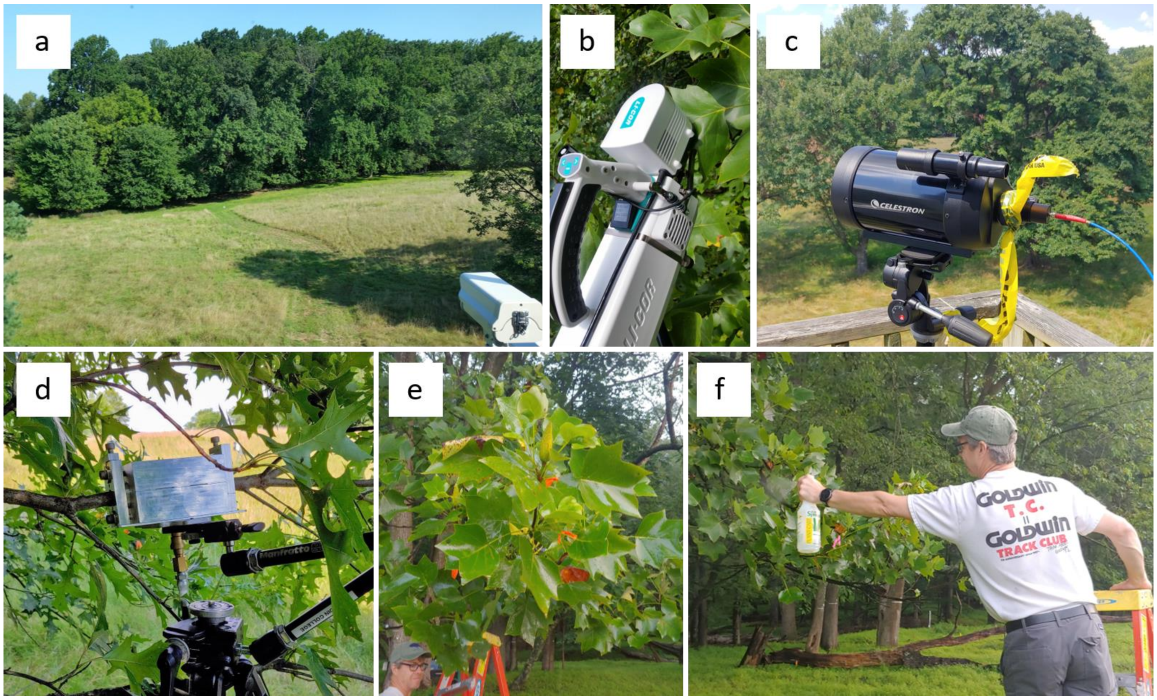

Figure S2. Field Photographs of the FOREST Site. a: View of the treeline from the field building balcony. **b:** The LI-COR 6800 clamped to a leaf. **c:** The SIF-measuring telescope. **d:** The pressure cuff in place around a branch. **e:** Field tape marking an experimental branch. **f:** Abscisic acid application with a spray bottle.

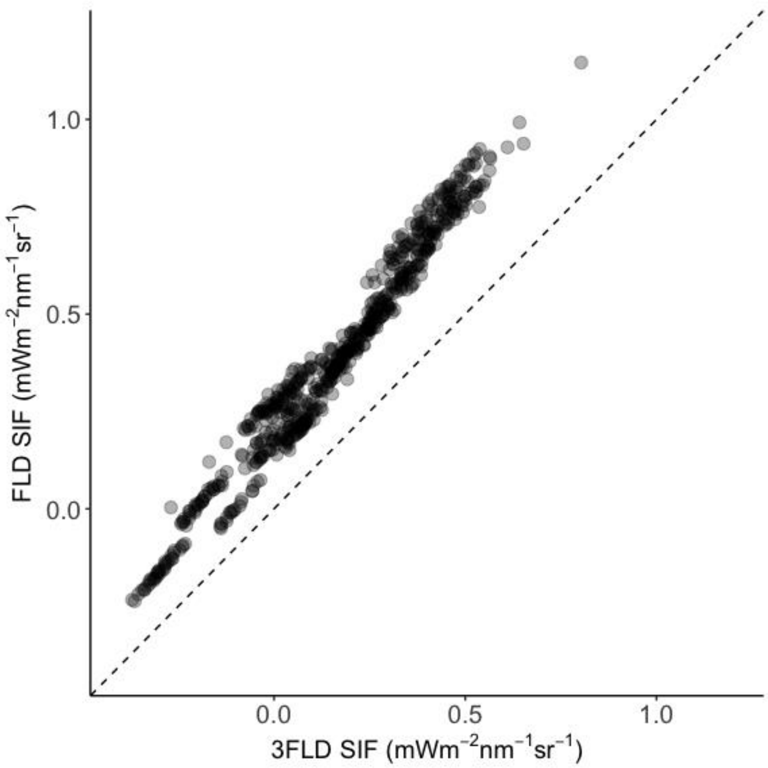

Figure S3. SIF Retrieval Method Intercomparison. Plot shows retrievals made using the Fraunhofer line depth (FLD) and 3FLD SIF retrieval methods. SIF retrievals are linearly related (R^2 = 0.97), with FLD retrievals being of slightly larger magnitude.

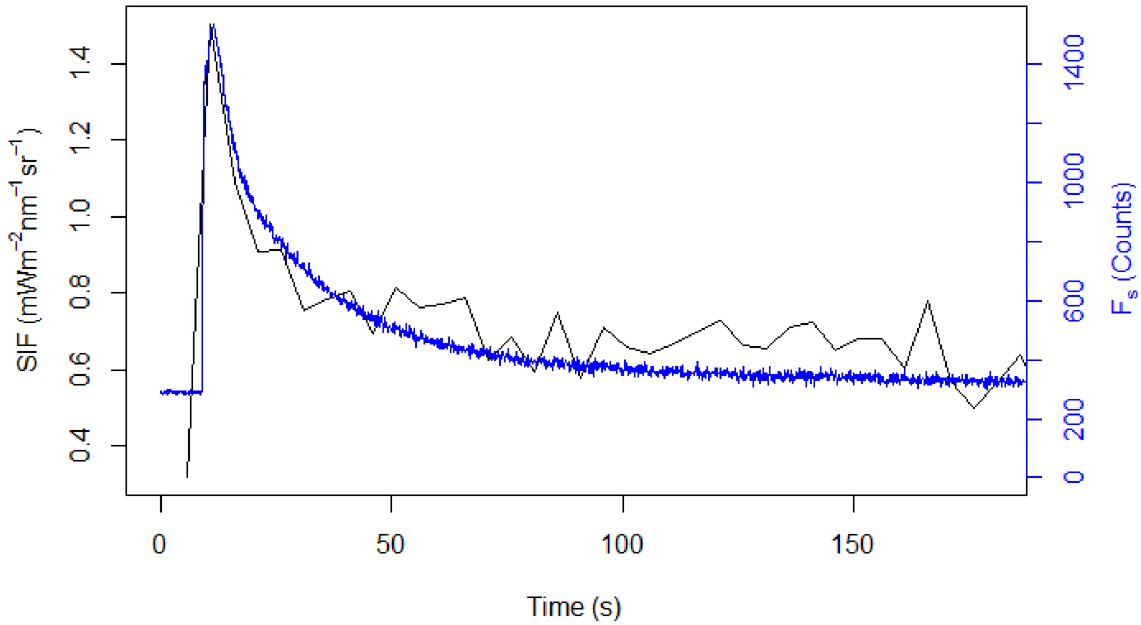

Figure S4. Kautsky Curve. SIF and F_s time series measured simultaneously show the characteristic Kautsky effect, with close temporal matching between the two data streams. SIF measurements were made on a white oak branch at approximately 100 m distance; F_s measurements were made at leaf level.

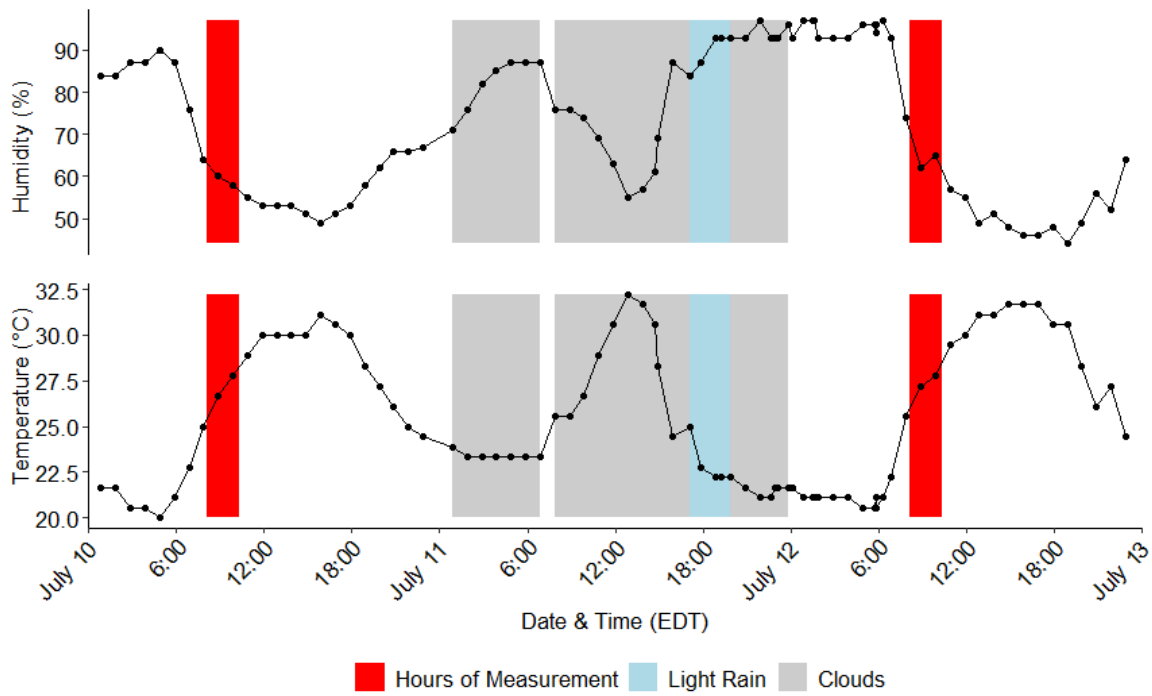

Figure S5. Local Meteorological Data. Data are from the historical archive of the Weather Underground station at Washington Dulles International Airport in Chantilly, Virginia, United States. Measurements were collected from 8:09 AM EDT to 10:18 AM EDT on 10 July 2019 and from 8:09 AM EDT to 10:20 AM EDT on 12 July 2019.

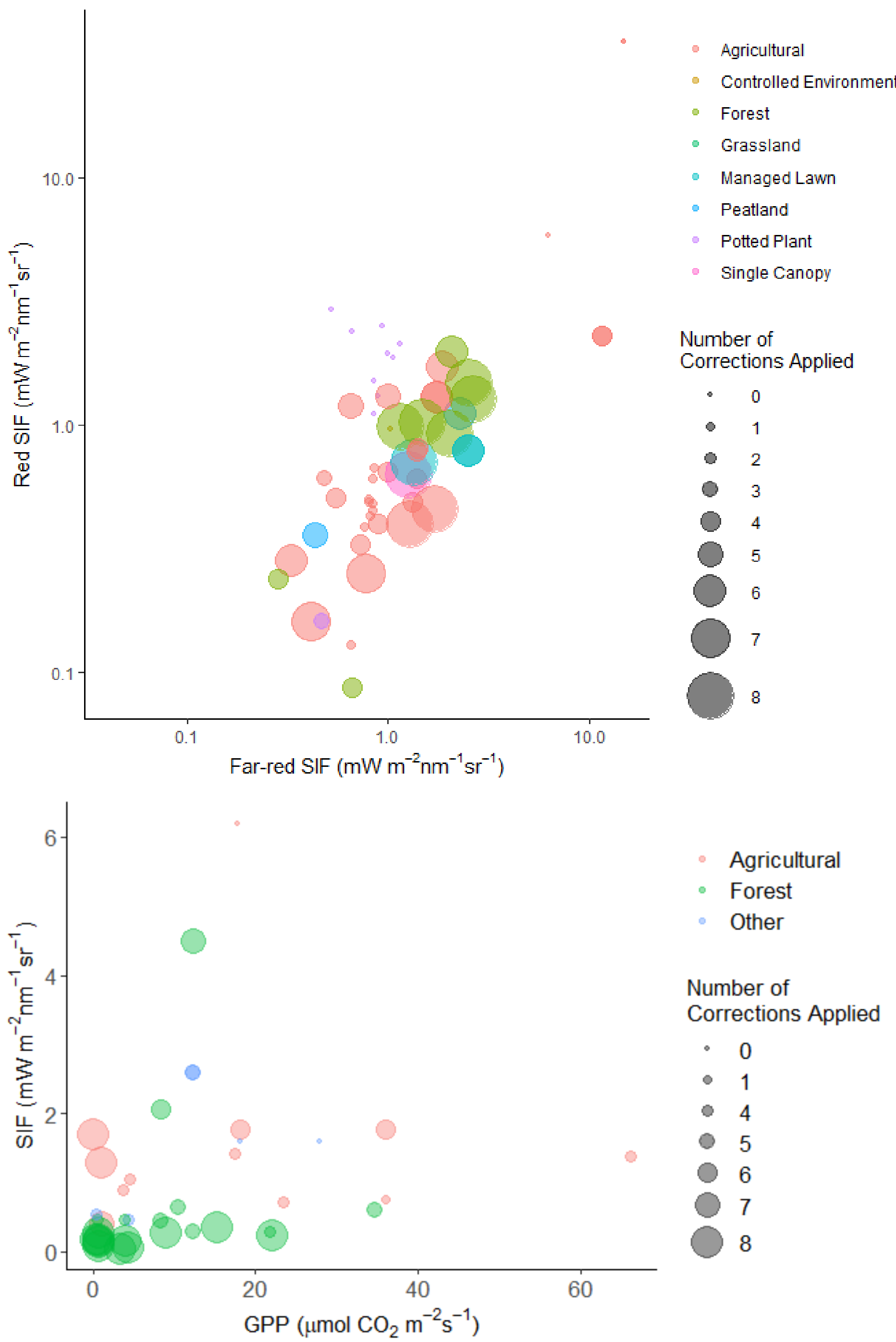

Figure S6. Number of Corrections Applied. (a) Mean far-red SIF values plotted against mean red SIF values from the same vegetated targets. Both axes are shown on a log scale. (b) Mean far-red SIF values plotted against mean gross primary productivity (GPP) values, where available. In both panels, points are color-coded by land cover type and point size shows the number of corrections applied to the SIF-measuring system used to make each retrieval.

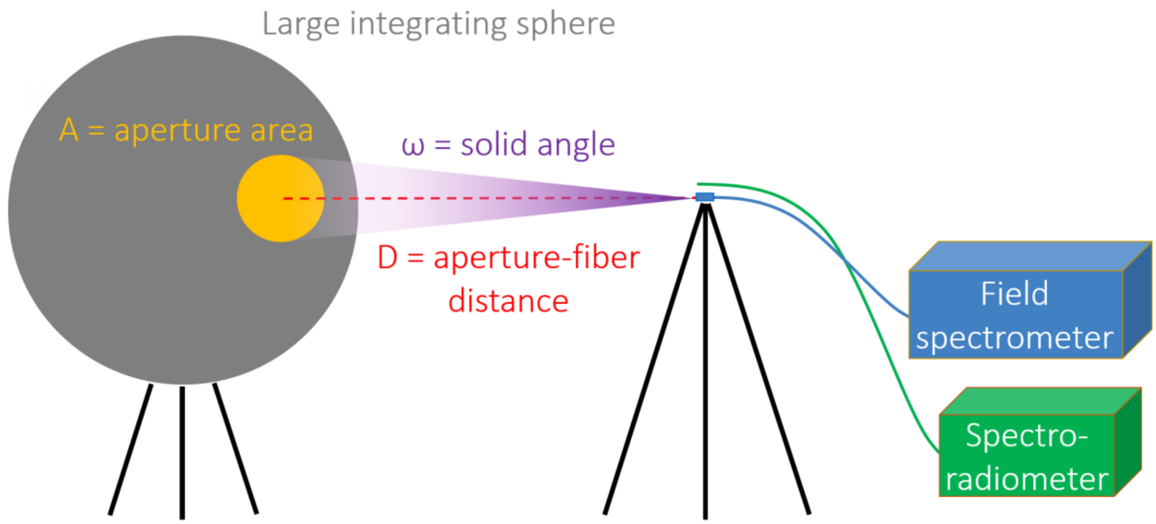

Figure S7. Radiometric Responsivity Laboratory Configuration. Idealized instrument configuration during laboratory measurements of radiometric responsivity for irradiance-measuring instruments.

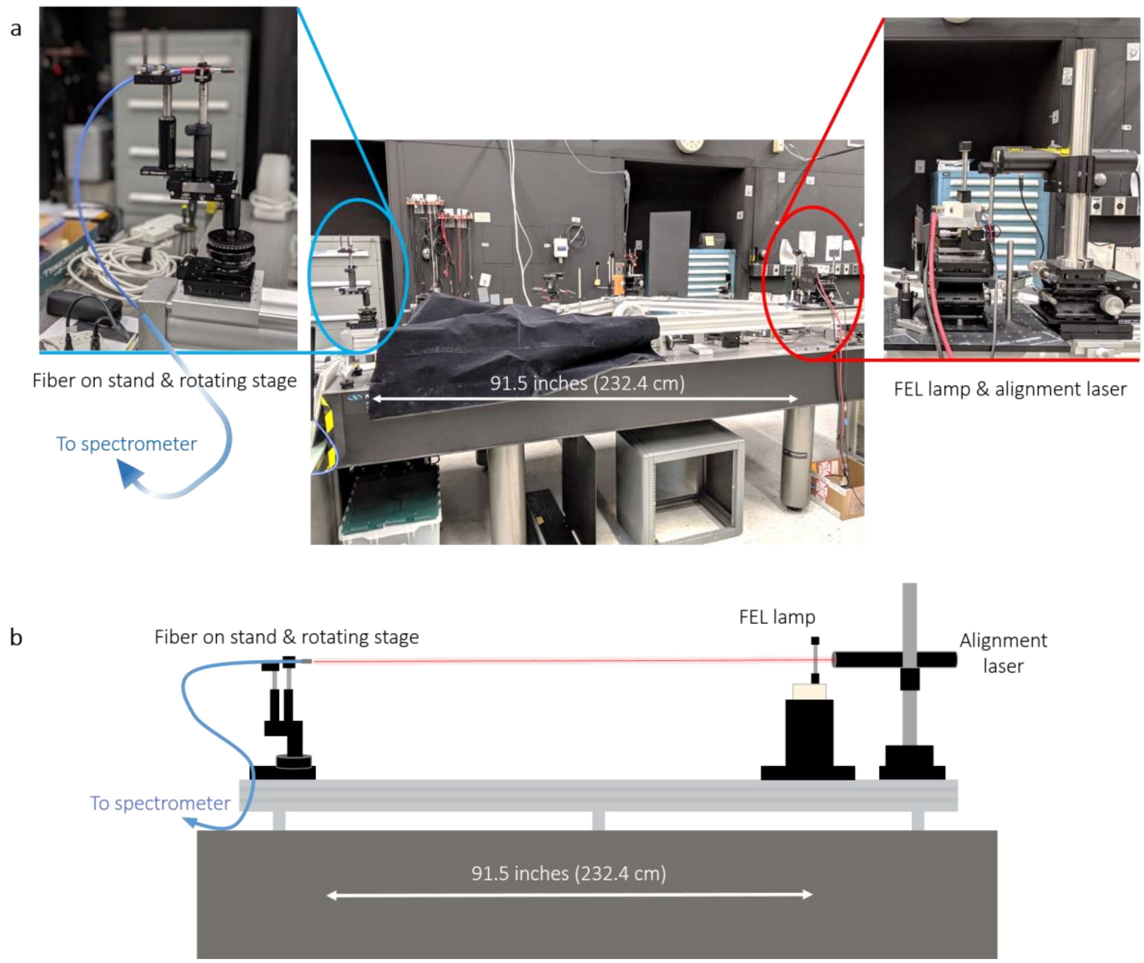

Figure S8. Cosine Corrector Characterization Laboratory Configuration. (a) Photographs of cosine corrector connected to fiber optic cable and spectrometer was mounted on a rotating stage (left), directly opposite a 1000 W FEL lamp and alignment laser (right). Lamp and cosine corrector were separated across a laboratory bench (center), on which a post (not shown) was placed during measurements of diffuse reflectance. (b) Simplified diagram of cosine corrector characterization laboratory configuration.

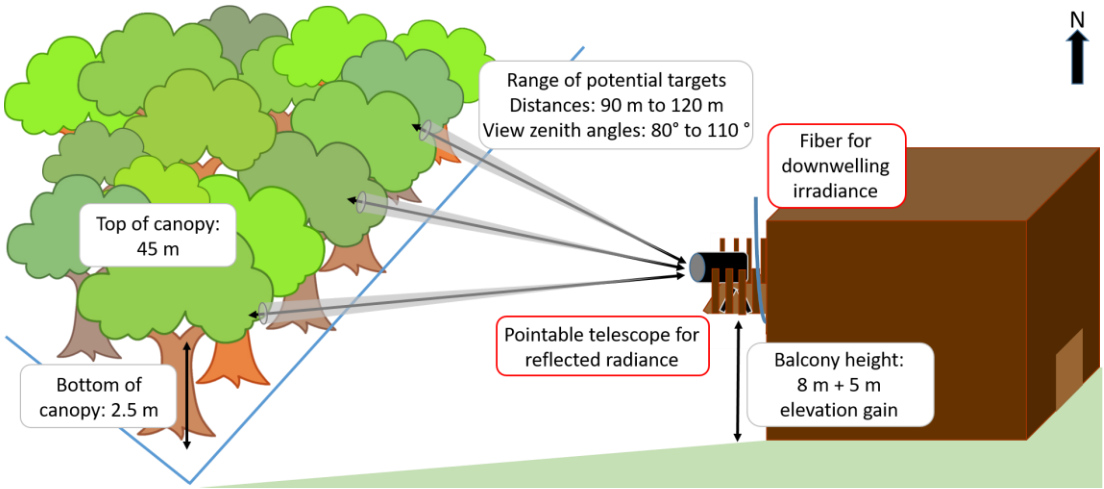

Figure S9. FOREST Site Schematic. The pointable telescope used for radiance measurements and fiber optic cable used for irradiance measurements are mounted on a building nearby the FOREST treeline, atop a small hill. Approximate heights, distances, and angles between sensor and vegetation are given as annotations.

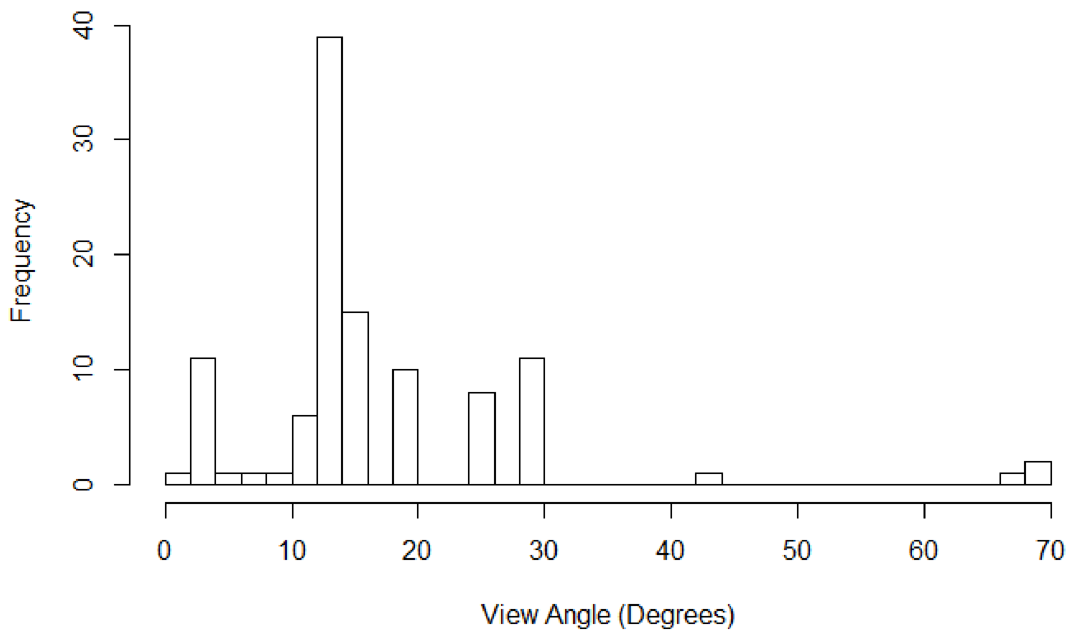

Figure S10. Range of View Zenith Angles. Values shown here were calculated from specifications provided from papers in the meta-analysis. View zenith angle values were obtained with one of three methods: [1] angles were taken directly from each paper where given, [2] angles were calculated using sensor height and swath width values, using the most extreme value along the swath for plotting, [3] angles were calculated based on angular field of view around measurements taken at nadir, with the plotted value being the most extreme angle at which light was collected from the field of view. These values illustrate a wide range of viewing angles used from tower-based and airborne SIF platforms. View angle values with a higher frequency are those repeated across papers that use the same sensor platform. Data to produce this figure can be found in Column BI of Table S1. Values in that column are marked with a number in brackets, corresponding to those above, to indicate the method by which the value was obtained.

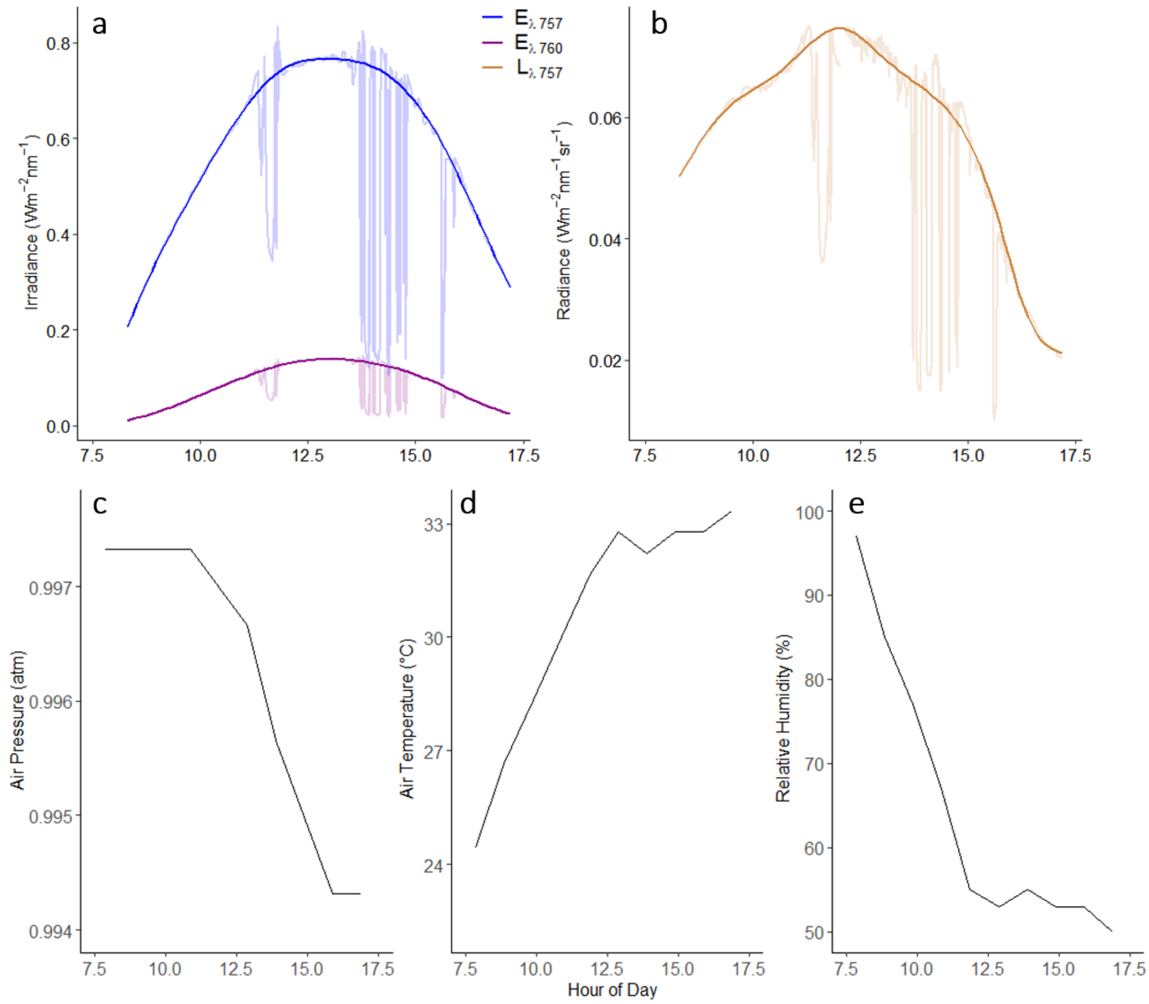

Figure S11. Inputs for Uncertainty Estimation. Smoothed time series of field-collected irradiance (a) and radiance (b) used as simulated data for uncertainty estimation. Time series of air pressure (c), air temperature (d), and relative humidity (e) were obtained from the Weather Underground historical data record from the Washington Dulles International Airport Station in Chantilly, Virginia, United States (Weather Underground, n.d.). All data are from 6 September 2018.

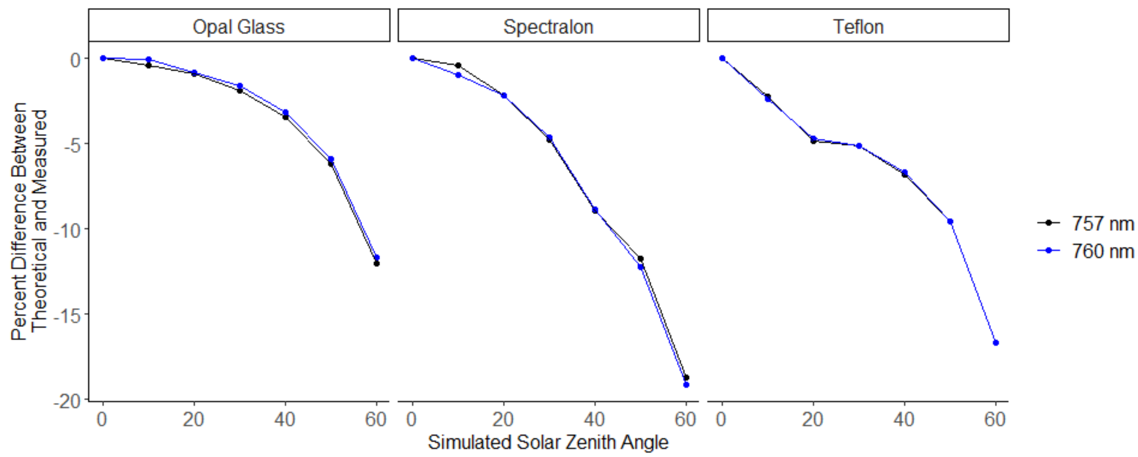

Figure S12. Wavelength Dependence of Cosine Corrector Effects. Percent difference between theoretical cosine function describing decrease in measured light intensity at increasing angles for three diffusive materials. Slight variation performance presented for two wavelengths (inside and outside of the atmospheric O_2-A absorption feature) relevant for FLD retrievals of solar-induced fluorescence.

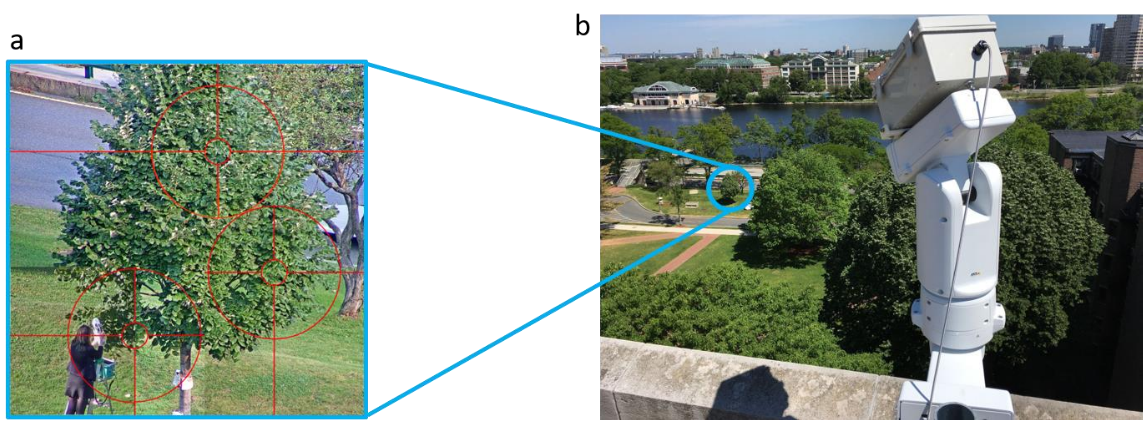

Figure S13. Cameron System and Fields of View. Overview of urban area in Boston, Massachusetts targeted with Cameron system, with AXIS camera and optics box mounted in foreground (panel b). Blue circled tree and panel a show silver linden tree from which data presented in this manuscript were collected, with level gas exchange measurements in progress (lower left side) and sapflow sensor visible (white box mid-stem). Fields of view (red crosshairs) are shown superimposed on panel a.

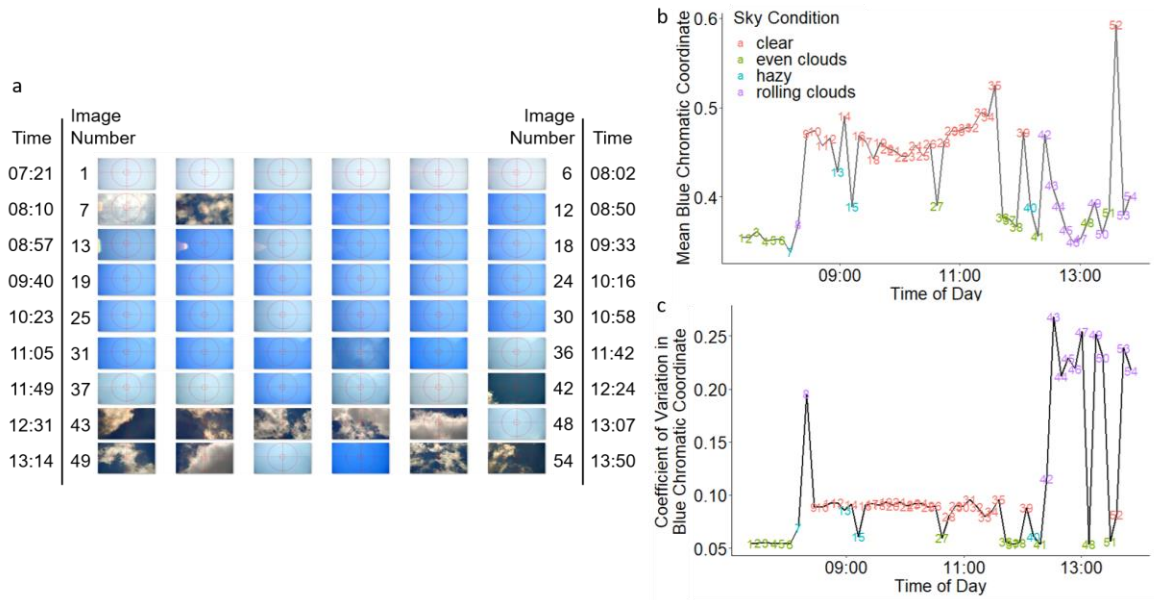

Figure S14. Sky Condition Index. Representative timeseries of sky images collected with Cameron system on 10 August 2020, along with timestamps and image numbers along left and right sides (panel a). Panels b and c show timeseries of mean blue chromatic coordinate (BCC) and coefficient of variation in BCC, respectively. Image numbers printed in plots correspond to image numbers from panel a, and are color coded based on sky condition category, following the legend in panel b.

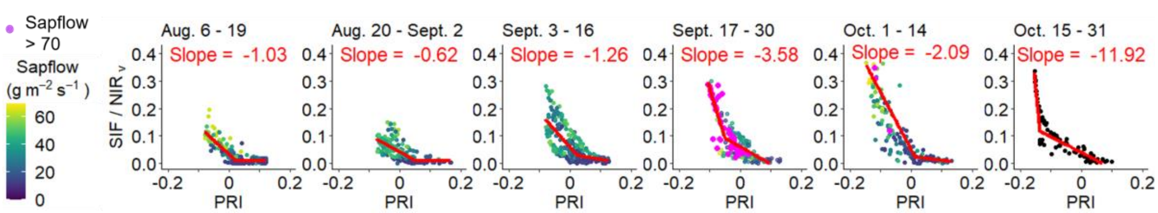

Figure S15. SIF/NIR$_v$-PRI Relationships. SIF / NIR$_v$ and PRI data from the 2020 growing season, aggregated to 15 min intervals. Red lines indicate segmented models fit to SIF and PRI data. Slopes printed in red indicate the slope of the uppermost portion of each segmented model. Point color ramp indicates sapflow value, and magenta points indicate sapflow values higher than 70 g m^{-2} s^{-1}.

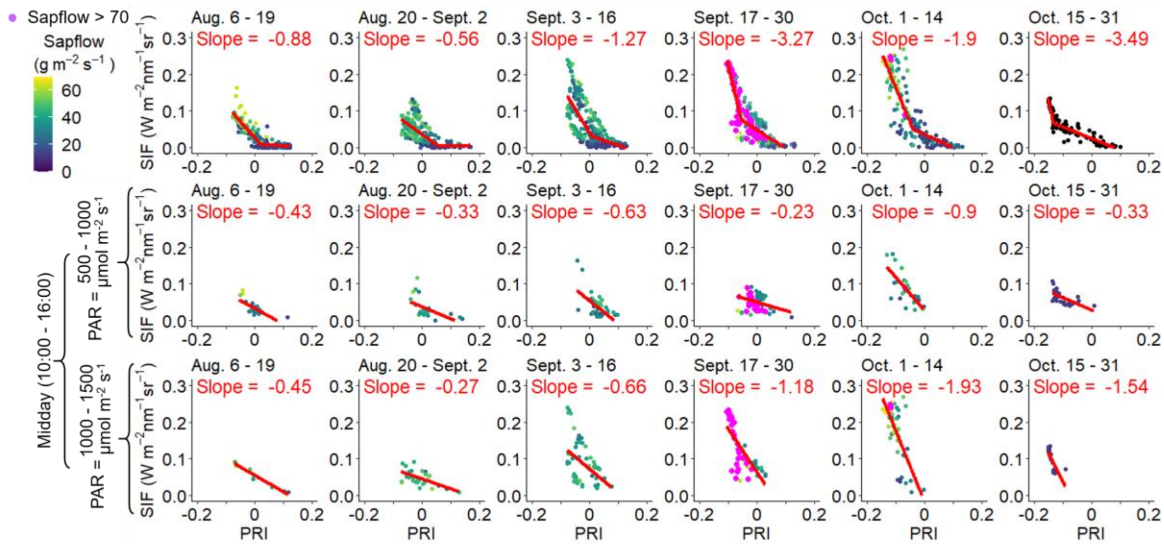

Figure S16. Midday SIF-PRI Relationships. For ease of reference, top row is identical to Figure 1, showing all available observations of SIF and PRI, aggregated to 15 min intervals over the 2020 growing season. Plots in top and middle rows show subsets of these data, limited to observations collected between 10:00 and 16:00 on each day, and where PAR fell between 500 umol m^{-2} s^{-1} to 1000 umol m^{-2} s^{-1} or 1000 umol m^{-2} s^{-1} to 1500 umol m^{-2} s^{-1}, respectively. Slopes printed in red in the top row indicate the slope of the uppermost portion of segmented models fit to SIF and PRI data. Slopes printed in red in middle and bottom rows indicate the slope of linear models fit to SIF and PRI data. Point color ramp indicates sapflow value, and magenta points indicate sapflow values higher than 70 g m^{-2} s^{-1}.

APPENDIX B: SUPPLEMENTARY TABLE

Paper Number	Title	Authors
1	Diurnal Cycle Relationships between Passive Fluorescence, PRI and NPQ of Vegetation in a Controlled Stress Experiment	Alonso, Luis; Van Wittenberghe, Shari; Amoros-Lopez, Julia; Vila-Frances, Joan; Gomez-Chova, Luis; Moreno, Jose
2	Study of the diurnal cycle of stressed vegetation for the improvement of fluorescence remote sensing	Amoros-Lopez, Julia; Gomez-Chova, Luis; Vila-Frances, Joan; Calpe, Javier; Alonso, Luis; Moreno, Jose; del Valle-Tascon, Secundino
3	Using spectral chlorophyll fluorescence and the photochemical reflectance index to predict physiological dynamics	Atherton, J.; Nichol, C. J.; Porcar-Castell, A.
4	Hyplant-Derived Sun-Induced Fluorescence-A New Opportunity to Disentangle Complex Vegetation Signals from Diverse Vegetation Types	Bandopadhyay, Subhajit; Rastogi, Anshu; Rascher, Uwe; Rademske, Patrick; Schickling, Anke; Cogliati, Sergio; Julitta, Tommaso; Mac Arthur, Alasdair; Hueni, Andreas; Tomelleri, Enrico; Celesti, Marco; Burkart, Andreas; Strozecki, Marcin; Sakowska, Karolina; Gabka, Maciej; Rosadzinski, Stanislaw; Sojka, Mariusz; Iordache, Marian-Daniel; Reusen, Ils; Van der Tol, Christiaan; Damm, Alexander; Schuettemeyer, Dirk; Juszczak, Radoslaw
5	Measuring Stress Reactions of Beech Seedlings with PRI, Fluorescence, Temperatures and Emissivity from VNIR and Thermal Field Imaging Spectroscopy	Buddenbaum, Henning; Rock, Gilles; Hill, Joachim; Werner, Willy
6	Diurnal and Seasonal Variations in Chlorophyll Fluorescence Associated with Photosynthesis at Leaf and Canopy Scales	Campbell, Petya K. E.; Huemmrich, Karl F.; Middleton, Elizabeth M.; Ward, Lauren A.; Julitta, Tommaso; Daughtry, Craig S. T.; Burkart, Andreas; Russ, Andrew L.; Kustas, William P.

Truncated table; full version can be downloaded from:
https://www.sciencedirect.com/science/article/pii/S0034425721001310

Table S1. **Intermediate-scale SIF Literature Meta-analysis Results** Meta-analysis data, column names and acronyms are below.

A: Paper number, assigned alphabetically by lead author surname
B: Paper title
C: Full list of authors
D: Year of publication
E: Journal name, volume, issue, and page numbers
F: Duration of measurements summarized in each row
G: Measurements made in indoor or outdoor environments
H: Season during which measurements were made
I: Time of day or time range over which measurements were made
J: Spatial scale of measurement
K: Measurements made at the leaf scale (Leaf) or a larger scale (Canopy)
L: Vegetation type
M: Geographic location for measurements
N: Plant name, species, and, where available, cultivar on which measurements were made
O: Distance or distance range from sensor to target (m)
P: Distance from sensor to target (m), with ranges from column O converted to a single mean value
Q: Method for measuring downwelling irradiance
R: Frequency of downwelling measurements
S: Frequency with which measurements of vegetation were made
T: Specification of whether measurements of vegetation were made as radiance (L) or reflectance (R)
U: Data averaging for each experiment
V: Spectrometer or device for measurements
W: Specification of whether measurement device was a commercial product or custom made in-house
X: Specification of whether device optics were dispersive and/or used filters during measurement
Y: Wavelength position(s) or range(s) in nm, used for far-red solar-induced fluorescence (SIF) retrievals
Z: Wavelength position(s) or range(s) in nm, used for red SIF retrievals
AA: Full width at half maximum (FWHM) [1], spectral resolution (SR) [2], or spectral sampling interval (SSI) [3] of measurement device in the wavelength range used for far-red SIF retrievals
AB: Full width at half maximum (FWHM) [1], spectral resolution (SR) [2], or spectral sampling interval (SSI) [3] of measurement device in the wavelength range used for red SIF retrievals
AC: Name of SIF retrieval method employed, using the following abbreviations: DOAS = differential optical absorption spectroscopy (Platt and Stutz, 2008), FLD = Fraunhofer line depth (Plascyk and Gabriel, 1975), 3FLD = 3-band FLD (Maier et al., 2003), Damm method = modified 3FLD (Damm et al., 2014), iFLD = improved FLD (Alonso et al., 2008), nFLD = n-band FLD (Daumard et al., 2010), pFLD = principal component analysis-based FLD (Liu and Liu, 2015), RHM = reflectance height method (Hu et al., 2017), SFM = spectral fitting methods (Meroni and Colombo, 2006), F-SFM = full-spectrum SFM (Liu et al., 2015). Full citations for references in this column can be found in the Bibliography.
AD: Simplified version of column AC
AE: Number of channels or wavelengths or windows used in far-red SIF retrieval
AF: Number of channels or wavelengths or windows used in red SIF retrieval
AG: Reflectance assumption within SIF spectral windows

AH: Fluorescence assumption within SIF spectral windows
AI: Study objective
AJ: Where appropriate, type of stress experienced by or manipulation applied to stressed vegetation
AK: Name of parameter used to quantify fluorescence
AL: Original reported fluorescence units
AM: Maximum far-red fluorescence value from stressed vegetation
AN: Mean far-red fluorescence value from stressed vegetation
AO: Maximum far-red fluorescence value from control vegetation
AP: Mean far-red fluorescence value from control vegetation
AQ: Maximum red fluorescence value from stressed vegetation
AR: Mean red fluorescence value from stressed vegetation
AS: Maximum red fluorescence value from control vegetation
AT: Mean red fluorescence value from control vegetation
AU: Maximum gross primary productivity (GPP) value from stressed vegetation
AV: Mean GPP value from stressed vegetation
AW: Maximum GPP value from control vegetation
AX: Mean GPP value from control vegetation
AY: Original units in which GPP data were reported. [*] indicates that values were originally reported as gross ecosystem productivity, net assimilation, or net photosynthesis.
AZ: Methods and/or equipment used to perform spectral alignment correction on measurement devices
BA: Methods used to perform electronic dark signal correction on measurement devices
BB: Cosine corrector specifications
BC: Methods used to perform atmospheric absorbance correction for SIF retrievals
BD: Target field equipment temperatures, temperature ranges, and protocols
BE: Signal-to-noise ratios (SNR) for measurement devices
BF: Methods used to quantify and correct detector nonlinearity
BG: Methods used to quantify and correct for stray light in measurement devices
BH: Methods and/or equipment used to perform radiometric calibration of measurement devices
BI: View zenith angle (VZA) between detector optics and target. Bracketed numbers indicate the method by which VZA was calculated. More detail on these methods is given in the caption to Figure S10.
BJ: Notes, including assumptions made while summarizing publication details and additional relevant citations in which instrumentation details can be found. Full citations for references cited in this column can be found in the Bibliography.

BIBLIOGRAPHY

Adams, W.W., Demmig-Adams, B., 1992. Operation of the xanthophyll cycle in higher plants in response to diurnal changes in incident sunlight. Planta 186, 390–398. https://doi.org/10.1007/BF00195320

Adams, W.W., Demmig-Adams, B., Logan, B.A., Barker, D.H., Osmond, C.B., 1999. Rapid changes in xanthophyll cycle-dependent energy dissipation and photosystem II efficiency in two vines, Stephania japonica and Smilax australis, growing in the understory of an open Eucalyptus forest. Plant, Cell & Environment 22, 125–136. https://doi.org/10.1046/j.1365-3040.1999.00369.x

Adams, W.W., Zarter, C.R., Ebbert, V., Demmig-Adams, B., 2004. Photoprotective Strategies of Overwintering Evergreens. Bioscience 54, 41–49. https://doi.org/10.1641/0006-3568(2004)054[0041:psooe]2.0.co;2

Albert, L., Cushman, K.C., Allen, D.W., Zong, Y., Alonso, L., Kellner, J.R., 2019. Stray light characterization in a high-resolution imaging spectrometer designed for solar-induced fluorescence, in: Proceedings of SPIE 10986, Algorithms, Technologies, and Applications for Multispectral and Hyperspectral Imagery XXV. p. 15. https://doi.org/10.1117/12.2519395

Allen, M.R., de Coninck, H., Dube, O.P., Hoegh-Guldberg, O., Jacob, D., Jiang, K., Revi, A., Rogelj, J., Roy, J., Shindell, D., Solecki, W., Taylor, M., Tschakert, P., Waisman, H., Halim, S.A., Antwi-Agyei, P., Aragón-Durand, F., Babiker, M., Bertoldi, P., Bindi, M., Brown, S., Buckeridge, M., Camilloni, I., Cartwright, A., Cramer, W., Dasgupta, P., Diedhiou, A., Djalante, R., Dong, W., Ebi, K.L., Engelbrecht, F., Fifita, S., Ford, J., Forster, P., Fuss, S., Ginzburg, V., Guiot, J., Handa, C., Hayward, B., Hijioka, Y., Hourcade, J.-C., Humphreys, S., Kainuma, M., Kala, J., Kanninen, M., Kheshgi, H., Kobayashi, S., Kriegler, E., Ley, D., Liverman, D., Mahowald, N., Mechler, R., Mehrotra, S., Mulugetta, Y., Mundaca, L., Newman, P., Okereke, C., Payne, A., Perez, R., Pinho, P.F., Revokatova, A., Riahi, K., Schultz, S., Séférian, R., Seneviratne, S.I., Steg, L., Suarez Rodriguez, A.G., Sugiyama, T., Thomas, A., Vilariño, M.V., Wairiu, M., Warren, R., Zickfeld, K., Zhou, G., 2018. Technical Summary, in: Masson-Delmotte, V., Zhai, P., Pörtner, H.-O., Roberts, D., Skea, J., Shukla, P.R., Pirani, A., Moufouma-Okia, W., Péan, C., Pidcock, R., Connors, S., Matthews, J.B.R., Chen, Y., Zhou, X., Gomis, M.I., Lonnoy, E., Maycock, T., Tignor, M., Waterfield, T. (Eds.), Global Warming of 1.5°C. An IPCC Special Report on the Impacts of Global Warming of 1.5°C above Pre-Industrial Levels and Related Global Greenhouse Gas Emission Pathways, in the Context of Strengthening the Global Response to the Threat of Climate Change,. pp. 1–22.

Alonso, L., Gómez-Chova, L., Vila-Francés, J., Amorós-López, J., Guanter, L., Calpe, J., Moreno, J., 2008. Improved Fraunhofer line discrimination method for vegetation fluorescence quantification. IEEE Geoscience and Remote Sensing Letters 5, 620–624. https://doi.org/10.1109/LGRS.2008.2001180

Alonso, L., Van Wittenberghe, S., Amoros-Lopez, J., Vila-Frances, J., Gomez-Chova, L., Moreno, J., 2017. Diurnal Cycle Relationships between Passive Fluorescence, PRI and NPQ of Vegetation in a Controlled Stress Experiment. Remote Sensing 9, 1–16. https://doi.org/10.3390/rs9080770

Amoros-Lopez, J., Gomez-Chova, L., Vila-Frances, J., Calpe, J., Alonso, L., Moreno, J., del Valle-Tascon, S., 2006. Study of the diurnal cycle of stressed vegetation for the improvement of fluorescence remote sensing, in: Owe, M and DUrso, G and Neale, CMU and Gouweleeuw, B. (Ed.), Proceedings of SPIE 6359, Remote Sensing for Agriculture, Ecosystems, and Hydrology VIII, Proceedings of SPIE. SPIE-INT SOC OPTICAL ENGINEERING, pp. 1–11. https://doi.org/10.1117/12.690036

Anav, A., Friedlingstein, P., Beer, C., Ciais, P., Harper, A., Jones, C., Murray-Tortarolo, G., Papale, D., Parazoo, N.C., Peylin, P., Piao, S., Sitch, S., Viovy, N., Wiltshire, A., Zhao, M., 2015. Spatiotemporal patterns of terrestrial gross primary production: A review. Reviews of Geophysic 53, 785–817. https://doi.org/10.1002/2015RG000483

Asner, G.P., Nepstad, D., Cardinot, G., Ray, D., 2004. Drought stress and carbon uptake in an Amazon forest measured with spaceborne imaging spectroscopy. Proceedings of the National Academy of Sci. 101, 6039–44. doi.org/10.1073/pnas.0400168101

Atherton, J., Nichol, C.J., Porcar-Castell, A., 2016. Using spectral chlorophyll fluorescence and the photochemical reflectance index to predict physiological dynamics. Remote Sensing of Environment 176, 17–30. https://doi.org/10.1016/j.rse.2015.12.036

Badgley, G., Field, C.B., Berry, J.A., 2017. Canopy near-infrared reflectance and terrestrial photosynthesis. Science Advances 3, 1–5. doi.org/10.1126/sciadv.1602244

Baker, N.R., 2008. Chlorophyll Fluorescence: A Probe of Photosynthesis In Vivo. Annual Review of Plant Biology 59, 89–113. https://doi.org/10.1146/annurev.arplant.59.032607.092759

Bandopadhyay, S., Rastogi, A., Rascher, U., Rademske, P., Schickling, A., Cogliati, S., Julitta, T., Mac Arthur, A., Hueni, A., Tomelleri, E., Celesti, M., Burkart, A., Strozecki, M., Sakowska, K., Gabka, M., Rosadzinski, S., Sojka, M., Iordache, M.-D., Reusen, I., der Tol, C., Damm, A., Schuettemeyer, D., Juszczak, R., 2019. Hyplant-Derived Sun-Induced Fluorescence-A New Opportunity to Disentangle Complex Vegetation Signals from Diverse Vegetation Types. Remote Sensing 11, 1–26. https://doi.org/10.3390/rs11141691

Bates, D., Maechler, M., Bolker, B., Walker, S., 2015. Fitting Linear Mixed-Effects

Models Using lme4. Journal of Statistical Software 67, 1–48.

Berry, J.A., Frankenberg, C., Wennberg, P. 2013. New Methods for Measurements of Photosynthesis from Space. California Institute of Technology.

Buddenbaum, H., Rock, G., Hill, J., Werner, W., 2015. Measuring Stress Reactions of Beech Seedlings with PRI, Fluorescence, Temperatures and Emissivity from VNIR and Thermal Field Imaging Spectroscopy. Europen Journal of Remote Sensing 48, 263–282. https://doi.org/10.5721/EuJRS20154815

Burkart, A., Schickling, A., Mateo, M.P.C., Wrobel, T.J., Rossini, M., Cogliati, S., Julitta, T., Rascher, U., 2015. A Method for Uncertainty Assessment of Passive Sun-Induced Chlorophyll Fluorescence Retrieval Using an Infrared Reference Light. IEEE Sensors Journal 15, 4603–4611. https://doi.org/10.1109/JSEN.2015.2422894

Campbell, P.K.E., Huemmrich, K.F., Middleton, E.M., Ward, L.A., Julitta, T., Daughtry, C.S.T., Burkart, A., Russ, A.L., Kustas, W.P., 2019. Diurnal and Seasonal Variations in Chlorophyll Fluorescence Associated with Photosynthesis at Leaf and Canopy Scales. Remote Sensing 11, 1–27. https://doi.org/10.3390/rs11050488

Cecchi, G., Lognoli, D., Mochi, I., Palombi, L., Petrini, E., Raimondi, V., 2003. A high spectral resolution sensor for active and passive remote sensing of vegetation fluorescence, in: IGARSS 2003: IEEE International Geoscience and Remote Sensing Symposium, Vols I - VII, Proceedings: Learning from Earth’s Shapes and Sizes, IEEE International Symposium on Geoscience and Remote Sensing (IGARSS). IEEE, pp. 591–593.

Cecchi, G., Mazzinghi, P., Pantani, L., Valentini, R., Tirelli, D., De Angelis, P., 1994. Remote sensing of chlorophyll a fluorescence of vegetation canopies: 1. Near and far field measurement techniques. Remote Sensing of Environment 47, 18–28. https://doi.org/10.1016/0034-4257(94)90123-6

Cendrero-Mateo, M.P., Bennertz, S., Burkart, A., Julitta, T., Cogliati, S., Scharr, H., Rademske, P., Alonso, L., Pinto, F., Rascher, U., 2018. Sun induced fluorescence calibration and validation for field phenotyping, in: IGARSS 2018 - IEEE International Geoscience and Remote Sensing Symposium, IEEE International Symposium on Geoscience and Remote Sensing IGARSS. IEEE, pp. 8248–8251.

Cendrero-Mateo, M.P., Wieneke, S., Damm, A., Alonso, L., Pinto, F., Moreno, J., Guanter, L., Celesti, M., Rossini, M., Sabater, N., Cogliati, S., Julitta, T., Rascher, U., Goulas, Y., Aasen, H., Pacheco-Labrador, J., Mac Arthur, A., 2019. Sun-Induced Chlorophyll Fluorescence III: Benchmarking Retrieval Methods and Sensor Characteristics for Proximal Sensing. Remote Sensing 11, 1–28. https://doi.org/10.3390/rs11080962

Chang, C.Y., Guanter, L., Frankenberg, C., Köhler, P., Gu, L., Magney, T.S., Grossmann, K., Sun, Y., 2020a. Systematic Assessment of Retrieval Methods for Canopy Far-Red Solar-Induced Chlorophyll Fluorescence Using High-Frequency Automated Field Spectroscopy. Journal of Geophysical Research. Biogeosciences 125, 1–26. https://doi.org/10.1029/2019JG005533

Chang, C.Y., Zhou, R., Kira, O., Marri, S., Skovira, J., Gu, L., Sun, Y., 2020b. An Unmanned Aerial System (UAS) for concurrent measurements of solar-induced chlorophyll fluorescence and hyperspectral reflectance toward improving crop monitoring. Agricultural and Forest Meteorology 294, 108145. https://doi.org/10.1016/j.agrformet.2020.108145

Cheng, Y.-B., Middleton, E.M., Zhang, Q., Huemmrich, K.F., Campbell, P.K.E., Corp, L.A., Cook, B.D., Kustas, W.P., Daughtry, C.S., 2013. Integrating solar induced fluorescence and the photochemical reflectance index for estimating gross primary production in a cornfield. Remote Sensing 5, 6857–6879. https://doi.org/10.3390/rs5126857

Cogliati, S., Colombo, R., Celesti, M., Tagliabue, G., Rascher, U., Schickling, A., Rademske, P., Alonso, L., Sabater, N., Schuettemeyer, D., Drusch, M., 2018. Red and far-red fluorescence emission retrieval from airborne high-resolution spectra collected by the HyPlant-FLUO sensor, in: IGARSS 2018 - IEEE International Geoscience and Remote Sensing Symposium, IEEE International Symposium on Geoscience and Remote Sensing IGARSS. IEEE, pp. 3935–3938.

Cogliati, S., Colombo, R., Rossini, M., Meroni, M., Julitta, T., Panigada, C., 2012. Retrieval of vegetation fluorescence from ground-based and airborne high resolution measurements, in: International Geoscience and Remote Sensing Symposium (IGARSS). IEEE, Munich, Germany, pp. 7129–7132. https://doi.org/10.1109/IGARSS.2012.6352019

Colombo, R., Meroni, M., Rossini, M., 2016. Development of fluorescence indices to minimise the effects of canopy structural parameters. Annali di Botanica 6, 93–99. https://doi.org/10.4462/annbotrm-13273

Corp, L.A., Middleton, E.M., Daughtry, C.S.T., Campbell, P.K.E., 2006. Solar Induced Fluorescence and Reflectance Sensing Techniques for Monitoring Nitrogen Utilization in Corn, in: 2006 IEEE International Geoscience and Remote Sensing Symposium, Vols 1-8, IEEE International Symposium on Geoscience and Remote Sensing IGARSS. IEEE, p. 2267+. https://doi.org/10.1109/IGARSS.2006.586

Damm, A., Elbers, J., Erler, A., Gioli, B., Hamdi, K., Hutjes, R., Kosvancova, M., Meroni, M., Miglietta, F., Moersch, A., Moreno, J., Schickling, A., Sonnenschein, R., Udelhoven, T., van der Linden, S., Hostert, P., Rascher, U., 2010. Remote sensing of sun-induced fluorescence to improve modeling of diurnal courses of gross primary production (GPP). Global Change Biology 16, 171–186. https://doi.org/10.1111/j.1365-2486.2009.01908.x

Damm, A., Guanter, L., Laurent, V.C.E., Schaepman, M.E., Schickling, A., Rascher, U., 2014. FLD-based retrieval of sun-induced chlorophyll fluorescence from medium spectral resolution airborne spectroscopy data. Remote Sensing of Environment 147, 256–266. https://doi.org/10.1016/j.rse.2014.03.009

Daumard, F., Champagne, S., Fournier, A., Goulas, Y., Ounis, A., Hanocq, J.-F., Moya, I., 2010. A field platform for continuous measurement of canopy fluorescence. IEEE Transactions on Geoscience and Remote Sensing 48, 3358–3368. https://doi.org/10.1109/TGRS.2010.2046420

Daumard, F., Goulas, Y., Champagne, S., Fournier, A., Ounis, A., Olioso, A., Moya, I., 2012. Continuous Monitoring of Canopy Level Sun-Induced Chlorophyll Fluorescence During the Growth of a Sorghum Field. IEEE Transactions on Geosci. and Remote Sensing 50, 4292–4300. https://doi.org/10.1109/TGRS.2012.2193131

Daumard, F., Goulas, Y., Ounis, A., Pedros, R., Moya, L., 2016. Measurement and correction of atmospheric effects in O-2-Band O-2-A absorption bands in the context of sun-induced fluorescence remote sensing, in: 2014 6th Workshop on Hyperspectral Image and Signal Processing: Evolution in Remote Sensing (WHISPERS), Workshop on Hyperspectral Image and Signal Processing. IEEE.

de Viller, J.A., Reblin, J.S., Logan, B.A., 2017. Needle properties of host white spruce (Picea glauca [Moench] Voss) experiencing eastern dwarf mistletoe (Arceuthobium pusillum Peck) infections of differing severity. Botany 95, 295–305. https://doi.org/dx.doi.org/10.1139/cjb-2016-0254

Dechant, B., Ryu, Y., Badgley, G., Zeng, Y., Berry, J.A., Zhang, Y., Goulas, Y., Li, Z., Zhang, Q., Kang, M., Li, J., Moya, I., 2020. Canopy structure explains the relationship between photosynthesis and sun-induced chlorophyll fluorescence in crops. Remote Sensing and Environment 241. https://doi.org/10.1016/j.rse.2020.111733

Demmig-Adams, B., 1998. Survey of thermal energy dissipation and pigment composition in sun and shade leaves. Plant & Cell Physiology 39, 474–482. https://doi.org/10.1093/oxfordjournals.pcp.a029394

Demmig-Adams, B., 1990. Carotenoids and photoprotection in plants: A role for the xanthophyll zeaxanthin. Biochimica et Biophysica Acta 1020, 1–24. https://doi.org/10.1016/0005-2728(90)90088-L

Demmig-Adams, B., Adams, W.W., 2006. Photoprotection in an ecological context: The remarkable complexity of thermal energy dissipation. New Phytologist 172, 11–21. https://doi.org/10.1111/j.1469-8137.2006.01835.x

Demmig-Adams, B., Adams, W.W., 1992. Photoprotection and Other Responses of Plants to High Light Stress. Annual Review of Plant Physiology and Plant Molecular Biology 43, 599–626. https://doi.org/10.1146/annurev.pp.43.060192.003123

Ding, W., Zhao, F., Yang, L., 2017. Analyzing the Impact of Sensor Characteristics on Retrieval Methods of Solar-Induced Fluorescence, in: Asundi, P. (Ed.), Proceedings of SPIE 10250, International Conference on Optical and Photonics Engineering (IcOPEN 2016), Proceedings of SPIE. SPIE-INT SOC OPTICAL ENGINEERING, pp. 1–5. https://doi.org/10.1117/12.2266734

Drolet, G., Wade, T., Nichol, C.J., MacLellan, C., Levula, J., Porcar-Castell, A., Nikinmaa, E., Vesala, T., 2014. A temperature-controlled spectrometer system for continuous and unattended measurements of canopy spectral radiance and reflectance. International Journal of Remote Sensing 35, 1769–1785. https://doi.org/10.1080/01431161.2014.882035

Du, S., Liu, L., Liu, X., Guo, J., Hu, J., Wang, S., Zhang, Y., 2019. SIFSpec: Measuring Solar-Induced Chlorophyll Fluorescence Observations for Remote Sensing of Photosynthesis. Sensors 19, 1–21. https://doi.org/10.3390/s19133009

Du, S., Liu, L., Liu, X., Hu, J., 2017. Response of canopy solar-induced chlorophyll fluorescence to the absorbed photosynthetically active radiation absorbed by chlorophyll. Remote Sensing 9, 1–19. https://doi.org/10.3390/rs9090911

Duveiller, G., Cescatti, A., 2016. Spatially downscaling sun-induced chlorophyll fluorescence leads to an improved temporal correlation with gross primary productivity. Remote Sensing of Environment 182, 72–89. https://doi.org/10.1016/j.rse.2016.04.027

Evain, S., Flexas, J., Moya, I., 2004. A new instrument for passive remote sensing: 2. Measurement of leaf and canopy reflectance changes at 531 nm and their relationship with photosynthesis and chlorophyll fluorescence. Remote Sensing of Environment 91, 175–185. https://doi.org/10.1016/j.rse.2004.03.012

Field, C.B., Lobell, D.B., Peters, H.A., Chiariello, N.R., 2007. Feedbacks of terrestrial ecosystems to climate change. Annual Review of Environment and Resources 32, 1–29. https://doi.org/10.1146/annurev.energy.32.053006.141119

Fox, J., Weisber, S., 2019. An R Companion to Applied Regression, 3rd ed. SAGE Publications, Inc., Thousand Oaks, CA.

Frankenberg, C., Fisher, J.B., Worden, J., Badgley, G., Saatchi, S.S., Lee, J.-E., Toon, G.C., Butz, A., Jung, M., Kuze, A., Yokota, T., 2011. New global observations of the terrestrial carbon cycle from GOSAT: Patterns of plant fluorescence with gross primary productivity. Geophysical Research Letters 38, 1–6.

https://doi.org/10.1029/2011GL048738

Frankenberg, C., Kohler, P., Magney, T.S., Geier, S., Lawson, P., Schwochert, M., McDuffie, J., Drewry, D.T., Pavlick, R., Kuhnert, A., 2018. The Chlorophyll Fluorescence Imaging Spectrometer (CFIS), mapping far red fluorescence from aircraft. Remote Sensing of Environment 217, 523–536. https://doi.org/10.1016/j.rse.2018.08.032

Fraser, G.T., Gibson, C.E., Yoon, H.W., Parr, A.C., 2007. "Once is enough" in radiometric calibrations. Journal of Research of the National Institute of Standards and Technology 112, 39–51. https://doi.org/10.6028/jres.112.003

Gamon, J., Hmimina, G., Miao, G., Guan, K., Springer, K., Wang, R., Yu, R., Gholizadeh, H., Moore, R., Walter-Shea, E., Arkebauer, T., Suyker, A., Franz, T., Wardlow, B., Wedin, D., 2018. Imaging spectrometry and fluorometry in support of FLEX: What can we learn from multi-scale experiments?, in: IGARSS 2018 - IEEE International Geoscience and Remote Sensing Symposium, IEEE International Symposium on Geoscience and Remote Sensing IGARSS. IEEE, pp. 3931–3934.

Gamon, J.A., Field, C.B., Goulden, M.L., Griffin, K.L., Anne, E., Applications, S.E., Feb, N., Gamon, J.A., Field, C.B., Goulden, M.L., Griffin, K.L., Hartley, A.E., Joel, G., Penuelas, J., Valentini, R., 1995. Relationships Between NDVI, Canopy Structure, and Photosynthesis in Three Californian Vegetation Types. Ecological Applications 5, 28–41.

Gamon, J.A., Penuelas, J., Field, C.B., 1992. A Narrow-Waveband Spectral Index That Tracks Diurnal Changes in Photosynthetic Efficiency. Remote Sensing of Environment 41, 35–44. https://doi.org/10.1016/0034-4257(92)90059-S

Garzonio, R., Di Mauro, B., Colombo, R., Cogliati, S., 2017. Surface Reflectance and Sun-Induced Fluorescence Spectroscopy Measurements Using a Small Hyperspectral UAS. Remote Sensing 9, 1–24. doi.org/10.3390/rs9050472

Gerhards, M., Schlerf, M., Rascher, U., Udelhoven, T., Juszczak, R., Alberti, G., Miglietta, F., Inoue, Y., 2018. Analysis of Airborne Optical and Thermal Imagery for Detection of Water Stress Symptoms. Remote Sensing 10, 1–23. https://doi.org/10.3390/rs10071139

GomezChova, L., AlonsoChorda, L., Amoros Lopez, J., Vila Frances, J., Del ValleTascon, S., Calpe, J., Moreno, J., 2006. Solar induced fluorescence measurements using a field spectroradiometer, in: DUrso, G and Jochum, MAO and Moreno, J. (Ed.), AIP Conference Proceedings, AIP Conference Proceedings. American Institute of Physics, pp. 274–281. https://doi.org/10.1063/1.2349354

Goulas, Y., Fournier, A., Daumard, F., Champagne, S., Ounis, A., Marloie, O., Moya, I.,

2017. Gross Primary Production of a Wheat Canopy Relates Stronger to Far Red Than to Red Solar-Induced Chlorophyll Fluorescence. Remote Sensing 9, 1–31. https://doi.org/10.3390/rs9010097

Grossmann, K., Frankenberg, C., Magney, T.S., Hurlock, S.C., Seibt, U., Stutz, J., 2018. PhotoSpec: A new instrument to measure spatially distributed red and far-red Solar-Induced Chlorophyll Fluorescence. Remote Sensing of Environment 216, 311–327. https://doi.org/10.1016/j.rse.2018.07.002

Gu, L., Han, J., Wood, J.D., Chang, C.Y.Y., Sun, Y., 2019a. Sun-induced Chl fluorescence and its importance for biophysical modeling of photosynthesis based on light reactions. New Phytologist 223, 1179–91. doi.org/10.1111/nph.15796

Gu, L., Wood, J.D., Chang, C.Y.Y., Sun, Y., Riggs, J.S., 2019b. Advancing Terrestrial Ecosystem Science With a Novel Automated Measurement System for Sun-Induced Chlorophyll Fluorescence for Integration With Eddy Covariance Flux Networks. Journal of Geophysical Research. Biogeosciences 124, 127–146. https://doi.org/10.1029/2018JG004742

Guanter, L., Zhang, Y., Jung, M., Joiner, J., Voigt, M., Berry, J.A., Frankenberg, C., Huete, A.R., Zarco-Tejada, P., Lee, J.-E., Moran, M.S., Ponce-Campos, G., Beer, C., Camps-Valls, G., Buchmann, N., Gianelle, D., Klumpp, K., Cescatti, A., Baker, J.M., Griffis, T.J., 2014. Global and time-resolved monitoring of crop photosynthesis with chlorophyll fluorescence. Proceedings of the National Academy of Sciences USA 111, E1327–E1333. https://doi.org/10.1073/pnas.1320008111

Heimann, M., Reichstein, M., 2008. Terrestrial ecosystem carbon dynamics and climate feedbacks. Nature 451, 289–292. https://doi.org/10.1038/nature06591

Helm, L.T., Shi, H., Lerdau, M.T., Yang, X., 2020. Solar-induced chlorophyll fluorescence and short-term photosynthetic response to drought. Ecological Applications. 30, 1–12. https://doi.org/10.1002/eap.2101

Hernandez-Clemente, R., North, P.R.J., Hornero, A., Zarco-Tejada, P.J., 2017. Assessing the effects of forest health on sun-induced chlorophyll fluorescence using the FluorFLIGHT 3-D radiative transfer model to account for forest structure. Remote Sensing of Environment 193, 165–179. doi.org/10.1016/j.rse.2017.02.012

Hu, J., Liu, L., Guo, J., Du, S., Liu, X., 2018. Upscaling Solar-Induced Chlorophyll Fluorescence from an Instantaneous to Daily Scale Gives an Improved Estimation of the Gross Primary Productivity. Remote Sensing 10, 1–20. https://doi.org/10.3390/rs10101663

Hu, J., Liu, L., Liu, X., 2017. Improving the retrieval of solar-induced chlorophyll fluorescence at canopy level by modeling the relative peak height of the apparent reflectance. Journal of Applied Remote Sensing 11, 026032–1–026032–15. https://doi.org/10.1117/1.JRS.11.026032

Hubbard, R.M., Ryan, M.G., Stiller, V., Sperry, J.S., 2001. Stomatal conductance and photosynthesis vary linearly with plant hydraulic conductance in ponderosa pine. Plant, Cell Environ. 24, 113–121. https://doi.org/10.1046/j.1365-3040.2001.00660.x

Huntzinger, D.N., Michalak, A.M., Schwalm, C., Ciais, P., King, A.W., Fang, Y., Schaefer, K., Wei, Y., Cook, R.B., Fisher, J.B., Hayes, D., Huang, M., Ito, A., Jain, A.K., Lei, H., Lu, C., Maignan, F., Mao, J., Parazoo, N., Peng, S., Poulter, B., Ricciuto, D., Shi, X., Tian, H., Wang, W., Zeng, N., Zhao, F., 2017. Uncertainty in the response of terrestrial carbon sink to environmental drivers undermines carbon-climate feedback predictions. Scientific Reports 7, 1–8. https://doi.org/10.1038/s41598-017-03818-2

Huwaldt, J.A., 2015. Plot Digitizer [WWW Document]. URL plotdigitizer.sourceforge.net

JB-Hyperspectral Devices UG, 2019. The Fluorescence Box, a hyperspectral instrument for unattended observation of chlorophyll fluorescence and reflectance. Manual for Installation and Operation.

Jimenez, M., Moncholi, A., Salido, E., de Miguel, E., 2018. Testing the measurability of sun induced fluorescence under optimal and non-optimal sky conditions, in: IGARSS 2018 - IEEE International Geoscience and Remote Sensing Symposium. IEEE, pp. 3505–3508.

Jones, T.S., Winbourne, J.B., Hutyra, L.R., 2020. Ribbonized sap flow: an emerging technology for the integration of sap flow sensor components onto a single platform. Ecosphere 11, 1–15. https://doi.org/10.1002/ecs2.3135

Jülich Research Centre, 2014. Technical Assistance for the Deployment of an Advanced Hyperspectral Imaging Sensor during HYFLEX.

Julitta, T., Corp, L.A., Rossini, M., Burkart, A., Cogliati, S., Davies, N., Hom, M., Arthur, A. Mac, Middleton, E.M., Rascher, U., Schickling, A., Colombo, R., 2016. Comparison of sun-induced chlorophyll fluorescence estimates obtained from four portable field spectroradiometers. Remote Sensing 8, 1–14. https://doi.org/10.3390/rs8020122

Kautsky, H., Hirsch, A., 1931. Neue Versuche zur Kohlensäureassimilation. Naturwissenschaften 19, 964. https://doi.org/https://doi.org/10.1007/BF01516164

Kim, J., Ryu, Y., Dechant, B., Lee, H., Kim, H.S., Kornfeld, A., Berry, J.A., 2021. Solar-induced chlorophyll fluorescence is non-linearly related to canopy photosynthesis in a temperate evergreen needleleaf forest during the fall transition. Remote Sensing of Environment 258, 112362. https://doi.org/10.1016/j.rse.2021.112362

Krause, G.H., Weis, E., 1991. Chlorophyll fluorescence and photosynthesis: The basics. Annual Review of Plant Physiology and Plant Molecular Biology 42, 313–349. https://doi.org/10.1002/9780470122563.ch3

Le Quéré, C., Andrew, R.M., Friedlingstein, P., Sitch, S., Pongratz, J., Manning, A.C., Korsbakken, J.I., Peters, G.P., Canadell, J.G., Jackson, R.B., Boden, T.A., Tans, P.P., Andrews, O.D., Arora, V.K., Bakker, D.C.E., Barbero, L., Becker, M., Betts, R.A., Bopp, L., Chevallier, F., Chini, L.P., Ciais, P., Cosca, C.E., Cross, J., Currie, K., Gasser, T., Harris, I., Hauck, J., Haverd, V., Houghton, R.A., Hunt, C.W., Hurtt, G., Ilyina, T., Jain, A.K., Kato, E., Kautz, M., Keeling, R.F., Klein Goldewijk, K., Körtzinger, A., Landschützer, P., Lefèvre, N., Lenton, A., Lienert, S., Lima, I., Lombardozzi, D., Metzl, N., Millero, F., Monteiro, P.M.S., Munro, D.R., Nabel, J.E.M.S., Nakaoka, S.-I., Nojiri, Y., Padin, X.A., Peregon, A., Pfeil, B., Pierrot, D., Poulter, B., Rehder, G., Reimer, J., Rödenbeck, C., Schwinger, J., Séférian, R., Skjelvan, I., Stocker, B.D., Tian, H., Tilbrook, B., Tubiello, F.N., Van Der Laan-Luijkx, I.T., Van Der Werf, G.R., Van Heuven, S., Viovy, N., Vuichard, N., Walker, A.P., Watson, A.J., Wiltshire, A.J., Zaehle, S., Zhu, D., 2018. Global Carbon Budget 2017. Earth System Science Data 10, 405–448. doi.org/10.5194/essd-10-405-2018

Li, L., Dai, C., Wu, Z., Wang, Y., 2018. Temperature correction method for commercial CCD array spectrometers used in spectral radiometry measurement. Journal of Physics. Conference Series 972, 0–6. doi.org/10.1088/1742-6596/972/1/012020

Li, X., Xiao, J., He, B., 2018. Chlorophyll fluorescence observed by OCO-2 is strongly related to gross primary productivity estimated from flux towers in temperate forests. Remote Sensing of Environment 204, 659–671. https://doi.org/10.1016/j.rse.2017.09.034

Lin, X., Chen, B., Zhang, H., Wang, F., Chen, J., Guo, L., Kong, Y., 2019. Effects of the temporal aggregation and meteorological conditions on the parameter robustness of OCO-2 SIF-based and LUE-based GPP models for croplands. Remote Sensing 11. https://doi.org/10.3390/rs11111328

Liu, L., Liu, X., Hu, J., Guan, L., 2017. Assessing the wavelength-dependent ability of solar-induced chlorophyll fluorescence to estimate the GPP of winter wheat at the canopy level. International Journal of Remote Sensing 38, 4396–4417. https://doi.org/10.1080/01431161.2017.1320449

Liu, L., Zhang, Y., Wang, J., Zhao, C., 2005. Detecting solar-induced chlorophyll fluorescence from field radiance spectra based on the Fraunhofer line principle. IEEE Transactions on Geoscience and Remote Sensing. 43, 827–832. https://doi.org/10.1109/TGRS.2005.843320

Liu, X., Liu, L., 2015. Improving Chlorophyll Fluorescence Retrieval Using Reflectance Reconstruction Based on Principal Components Analysis. IEEE Geoscience and Remote Sensing Letters 12, 1645–49. https://doi.org/10.1109/LGRS.2015.2417857

Liu, X., Liu, L., Zhang, S., Zhou, X., 2015. New spectral fitting method for full-spectrum solar-induced chlorophyll fluorescence retrieval based on principal components analysis. Remote Sensing 7, 10626–10645. https://doi.org/10.3390/rs70810626

Logan, B.A., Adams, W.W., Demmig-Adams, B., 2007. Avoiding common pitfalls of chlorophyll fluorescence analysis under field conditions. Functional Plant Biology 34, 853–859. https://doi.org/10.1071/FP07113

Logan, B.A., Grace, S.C., Adams, W.W., Demmig-Adams, B., 1998. Seasonal differences in xanthophyll cycle characteristics and antioxidants in Mahonia repens growing in different light environments. Oecologia 116, 9–17. https://doi.org/10.1007/s004420050558

Lu, X., Liu, Z., An, S., Miralles, D.G., Maes, W.H., Liu, Y., Tang, J., 2018. Potential of solar-induced chlorophyll fluorescence to estimate transpiration in a temperate forest. Agricultural and Forest Meteorology 252, 75–87. https://doi.org/10.1016/j.agrforrnet.2018.01.017

Lucieer, A., Malenovský, Z., Veness, T., Wallace, L., 2014. HyperUAS—Imaging Spectroscopy from a Multirotor Unmanned Aircraft System. Journal of Field Robotics 31, 571–590. https://doi.org/10.1002/rob.21508

Magney, T.S., Barnes, M.L., Yang, X., 2020. On the Covariation of Chlorophyll Fluorescence and Photosynthesis Across Scales. Geophysical Research Letters 47, 1–7. https://doi.org/10.1029/2020GL091098

Magney, T.S., Bowling, D.R., Logan, B.A., Grossmann, K., Stutz, J., Blanken, P.D., Burns, S.P., Cheng, R., Garcia, M.A., Kohler, P., Lopez, S., Parazoo, N.C., Raczka, B., Schimel, D., Frankenberg, C., 2019a. Mechanistic evidence for tracking the seasonality of photosynthesis with solar-induced fluorescence. Proc. Natl. Acad. Sci. U. S. A. 116, 11640–11645. https://doi.org/10.1073/pnas.1900278116

Magney, T.S., Frankenberg, C., Fisher, J.B., Sun, Y., North, G.B., Davis, T.S., Kornfeld, A., Siebke, K., 2017. Connecting active to passive fluorescence with photosynthesis: a method for evaluating remote sensing measurements of Chl fluorescence. New Phytologist 215, 1594–1608. https://doi.org/10.1111/nph.14662

Magney, T.S., Frankenberg, C., Kohler, P., North, G., Davis, T.S., Dold, C., Dutta, D., Fisher, J.B., Grossmann, K., Harrington, A., Hatfield, J., Stutz, J., Sun, Y., Porcar-Castell, A., 2019b. Disentangling Changes in the Spectral Shape of Chlorophyll Fluorescence: Implications for Remote Sensing of Photosynthesis. J. Geophys. Res.

- Biogeosciences 124, 1491–1507. https://doi.org/10.1029/2019JG005029

Maguire, A.J., Eitel, J.U.H., Griffin, K.L., Magney, T.S., Long, R.A., Vierling, L.A., Schmiege, S.C., Jennewein, J.S., Weygint, W.A., Boelman, N.T., Bruner, S.G., 2020. On the Functional Relationship Between Fluorescence and Photochemical Yields in Complex Evergreen Needleleaf Canopies. Geophysical Research Letters 47, 1–9. https://doi.org/10.1029/2020GL087858

Maier, S.W., Günther, K.P., Stellmes, M., 2003. Sun-Induced Fluorescence: A New Tool for Precision Farming, in: Schepers, J., VanToai, T. (Eds.), Digital Imaging and Spectral Techniques: Applications to Precision Agriculture and Crop Physiology . American Society of Agronomy, Madison, USA, pp. 209–222. https://doi.org/10.2134/asaspecpub66.c16

Makisara, K., Meinander, M., Rantasuo, M., Okkonen, J., Aikio, M., Sipola, K., Pylkko, P., Braam, B., 1993. Airborne imaging spectrometer for applications (AISA). International Geoscience and Remote Sensing Symposium Series. 2, 479–481. https://doi.org/10.1109/igarss.1993.322291

Marrs, J.K., Hutyra, L.R., Allen, D.W., 2019. Solar-induced fluorescence retrievals in the context of physiological, environmental, and hardware-based sources of uncertainty, in: Proceedings of SPIE 10986, Algorithms, Technologies, and Applications for Multispectral and Hyperspectral Imagery XXV. pp. 1–14. https://doi.org/10.1117/12.2520457

Marrs, J.K., Jones, T.S., Allen, D.W., Hutyra, L.R., 2021. Instrumentation sensitivities for tower-based solar-induced fluorescence measurements. Remote Sensing of Environment 259, 112413. https://doi.org/10.1016/j.rse.2021.112413

Marrs, J.K., Reblin, J.S., Logan, B.A., Allen, D.W., Reinmann, A.B., Bombard, D.M., Tabachnik, D., Hutyra, L.R., 2020. Solar-induced fluorescence does not track photosynthetic carbon assimilation following induced stomatal closure. Geophysical Research Letters 47, 1–11. https://doi.org/10.1029/2020GL087956

Maxwell, K., Johnson, G.N., 2000. Chlorophyll fluorescence—a practical guide. Journal of Experimental Botany 51, 659–668. https://doi.org/10.1093/jxb/51.345.659

Meroni, M., Barducci, A., Cogliati, S., Castagnoli, F., Rossini, M., Busetto, L., Migliavacca, M., Cremonese, E., Galvagno, M., Colombo, R., Di Cella, U.M., 2011. The hyperspectral irradiometer, a new instrument for long-term and unattended field spectroscopy measurements. Review of Scientific Instruments 82, 043106. https://doi.org/10.1063/1.3574360

Meroni, M., Colombo, R., 2006. Leaf level detection of solar induced chlorophyll fluorescence by means of a subnanometer resolution spectroradiometer. Remote

Sensing of Environment 103, 438–448. https://doi.org/10.1016/j.rse.2006.03.016

Meroni, M., Rossini, M., Guanter, L., Alonso, L., Rascher, U., Colombo, R., Moreno, J., 2009. Remote sensing of solar-induced chlorophyll fluorescence: Review of methods and applications. Remote Sensing of Environment 113, 3. https://doi.org/10.1016/j.rse.2009.05.003

Miao, G., Guan, K., Yang, X., Bernacchi, C.J., Berry, J.A., DeLucia, E.H., Wu, J., Moore, C.E., Meacham, K., Cai, Y., Peng, B., Kimm, H., Masters, M.D., 2018. Sun-Induced Chlorophyll Fluorescence, Photosynthesis, and Light Use Efficiency of a Soybean Field from Seasonally Continuous Measurements. Journal of Geophysical Research - Biogeosciences 123, 610–623. https://doi.org/10.1002/2017JG004180

Middleton, E.M., Corp, L.A., Campbell, P.K.E., 2007. Canopy level solar induced fluorescence for vegetation in controlled experiments, in: IGARSS: 2007 IEEE International Geoscience and Remote Sensing Symposium, Vols 1-12: Sensing and Understanding Our Planet, IEEE International Symposium on Geoscience and Remote Sensing IGARSS. IEEE, pp. 3760–3764.

Middleton, E.M., Huemmrich, K.F., Landis, D.R., Black, T.A., Barr, A.G., McCaughey, J.H., 2016. Photosynthetic efficiency of northern forest ecosystems using a MODIS-derived Photochemical Reflectance Index (PRI). Remote Sensing of Environment 187, 345–366. https://doi.org/10.1016/j.rse.2016.10.021

Middleton, E.M., Rascher, U., Corp, L.A., Huemmrich, K.F., Cook, B.D., Noormets, A., Schickling, A., Pinto, F., Alonso, L., Damm, A., Guanter, L., Colombo, R., Campbell, P.K.E., Landis, D.R., Zhang, Q., Rossini, M., Schuettemeyer, D., Bianchi, R., 2017. The 2013 FLEX-US Airborne Campaign at the Parker Tract Loblolly Pine Plantation in North Carolina, USA. Remote Sensing 9, 1–31. https://doi.org/10.3390/rs9060612

Migliavacca, M., Perez-Priego, O., Rossini, M., El-Madany, T.S., Moreno, G., van der Tol, C., Rascher, U., Berninger, A., Bessenbacher, V., Burkart, A., Carrara, A., Fava, F., Guan, J.-H., Hammer, T.W., Henkel, K., Juarez-Alcalde, E., Julitta, T., Kolle, O., Pilar Martin, M., Musavi, T., Pacheco-Labrador, J., Perez-Burgueno, A., Wutzler, T., Zaehle, S., Reichstein, M., 2017. Plant functional traits and canopy structure control the relationship between photosynthetic CO2 uptake and far-red sun-induced fluorescence in a Mediterranean grassland under different nutrient availability. New Phytologist 214, 1078–1091. https://doi.org/10.1111/nph.14437

Mohammed, G.H., Colombo, R., Middleton, E.M., Rascher, U., van der Tol, C., Nedbal, L., Goulas, Y., Pérez-Priego, O., Damm, A., Meroni, M., Joiner, J., Cogliati, S., Verhoef, W., Malenovský, Z., Gastellu-Etchegorry, J.P., Miller, J.R., Guanter, L., Moreno, J., Moya, I., Berry, J.A., Frankenberg, C., Zarco-Tejada, P.J., 2019. Remote sensing of solar-induced chlorophyll fluorescence (SIF) in vegetation:

50 years of progress. Remote Sensing of Environment 231, 111177. https://doi.org/10.1016/j.rse.2019.04.030

Monteith, J.L.L., 1972. Solar Radiation and Productivity in Tropical Ecosystems. Journal of Applied Ecology 9, 747–766.

Moreno, J., Goulas, Y., Huth, A., Middleton, E., Miglietta, F., Mohammed, G., Nedbal, L., Rascher, U., Verhoef, W., 2015. Report for Mission Selection: FLEX (ESA SP-1330/2, June 2015). Noordwijk, Netherlands.

Moya, I., Daumard, F., Moise, N., Ounis, A., Goulas, Y., 2006. First airborne multiwavelength passive chlorophyll fluorescence measurements over La Mancha (Spain) fields, in: 2nd International Symposium on Recent Advances in Quantitative Remote Sensing: RAQRS'II. Torrent (Valencia), Spain, pp. 1–6.

Muggeo, V.M.R., 2008. segmented: an R Package to Fit Regression Models with Broken-Line Relationships. R News 8, 20–25.

Ni, Z., Liu, Z., Li, Z.-L., Nerry, F., Huo, H., Sun, R., Yang, P., Zhang, W., 2016. Investigation of Atmospheric Effects on Retrieval of Sun-Induced Fluorescence Using Hyperspectral Imagery. Sensors 16, 1–19. https://doi.org/10.3390/s16040480

Nichol, C.J., Drolet, G., Porcar-Castell, A., Wade, T., Sabater, N., Middleton, E.M., MacLellan, C., Levula, J., Mammarella, I., Vesala, T., Atherton, J., 2019. Diurnal and Seasonal Solar Induced Chlorophyll Fluorescence and Photosynthesis in a Boreal Scots Pine Canopy. Remote Sensing 11, 1–22. https://doi.org/10.3390/rs11030273

Pacheco-Labrador, Hueni, Mihai, Sakowska, Julitta, Kuusk, Sporea, Alonso, Burkart, Cendrero-Mateo, Aasen, Goulas, Mac Arthur, 2019. Sun-Induced Chlorophyll Fluorescence I: Instrumental Considerations for Proximal Spectroradiometers. Remote Sensing 11, 1–30. https://doi.org/10.3390/rs11080960

Pan, Y., Birdsey, R.A., Fang, J., Houghton, R., Kauppi, P.E., Kurz, W.A., Phillips, O.L., Shvidenko, A., Lewis, S.L., Canadell, J.G., Ciais, P., Jackson, R.B., Pacala, S.A., McGuire, D., Shilong Piao, 2, Rautiainen, A., Sitch, S., Hayes, D., 2011. A Large and Persistent Carbon Sink in the World's Forests. Science 333, 988–993. https://doi.org/10.1126/science.1201609

Parazoo, N.C., Coleman, R.W., Yadav, V., Stavros, E.N., Hulley, G., Hutyra, L.R., 2022 Estimating biological carbon fluxes in a mixed urban Mediterranean landscape using high resolution thermal and optical remote sensing constraints. Science of the Total Environment 806, 151335.

Paul-Limoges, E., Damm, A., Hueni, A., Liebisch, F., Eugster, W., Schaepman, M.E., Buchmann, N., 2018. Effect of environmental conditions on sun-induced fluorescence in a mixed forest and a cropland. Remote Sensing of Environment 219, 310–323. https://doi.org/10.1016/j.rse.2018.10.018

Perez-Priego, O., Guan, J., Rossini, M., Fava, F., Wutzler, T., Moreno, G., Carvalhais, N., Carrara, A., Kolle, O., Julitta, T., Schrumpf, M., Reichstein, M., Migliavacca, M., 2015. Sun-induced chlorophyll fluorescence and photochemical reflectance index improve remote-sensing gross primary production estimates under varying nutrient availability in a typical Mediterranean savanna ecosystem. Biogeosciences 12, 6351–6367. https://doi.org/10.5194/bg-12-6351-2015

Pinto, F., Celesti, M., Acebron, K., Alberti, G., Cogliati, S., Colombo, R., Juszczak, R., Matsubara, S., Miglietta, F., Palombo, A., Panigada, C., Pignatti, S., Rossini, M., Sakowska, K., Schickling, A., Schüttemeyer, D., Stróżecki, M., Tudoroiu, M., Rascher, U., 2020. Dynamics of sun-induced chlorophyll fluorescence and reflectance to detect stress-induced variations in canopy photosynthesis. Plant, Cell & Environment 1–18. https://doi.org/10.1111/pce.13754

Pinto, F., Muller-Linow, M., Schickling, A., Cendrero-Mateo, M.P., Ballvora, A., Rascher, U., 2017. Multiangular Observation of Canopy Sun-Induced Chlorophyll Fluorescence by Combining Imaging Spectroscopy and Stereoscopy. Remote Sensing 9, 1–21. https://doi.org/10.3390/rs9050415

Plascyk, J.A., Gabriel, F.C., 1975. The Fraunhofer Line Discriminator MKII-An Airborne Instrument for Precise and Standardized Ecological Luminescence Measurement. IEEE Transactions on Instrumentation and Measurement 24, 306–313. https://doi.org/10.1109/TIM.1975.4314448

Platt, U., Stutz, J., 2008. Differential Optical Absorption Spectroscopy: Principles and Applications, 1st ed. Springer-Verlag, Berlin, Germany; Heidelberg, Germany. https://doi.org/10.1007/978-3-540-75776-4

Porcar-Castell, A., Pfündel, E., Korhonen, J.F.J., Juurola, E., 2008. A new monitoring PAM fluorometer (MONI-PAM) to study the short- and long-term acclimation of photosystem II in field conditions. Photosynthesis Research 96, 173–179. https://doi.org/10.1007/s11120-008-9292-3

Porcar-Castell, A., Tyystjärvi, E., Atherton, J., van der Tol, C., Flexas, J., Pfuendel, E.E., Moreno, J., Frankenberg, C., Berry, J.A., 2014. Linking chlorophyll a fluorescence to photosynthesis for remote sensing applications: mechanisms and challenges. Journal of Experimental Botany 65, 4065–4095. https://doi.org/10.1093/jxb/eru191

Qiu, B., Xue, Y., Fisher, J.B., Guo, W., Berry, J.A., Zhang, Y., 2018. Satellite Chlorophyll Fluorescence and Soil Moisture Observations Lead to Advances in the Predictive Understanding of Global Terrestrial Coupled Carbon-Water Cycles. Global Biogeochemical Cycles 32, 360–375. https://doi.org/10.1002/2017GB005744

R Core Team, 2018. R: A language and environment for statistical computing. R Foundation for Statistical Computing.

Raczka, B., Porcar-Castell, A., Magney, T., Lee, E., Kohler, P., Frankenberg, C., Grossmann, K., Logan, B.A., Stutz, J., Blanken, P.D., Burns, S.P., Duarte, H., Yang, X., Lin, J.C., Bowling, D.R., 2019. Sustained Nonphotochemical Quenching Shapes the Seasonal Pattern of Solar-Induced Fluorescence at a High-Elevation Evergreen Forest. Journal of Geophysical Research - Biogeosciences 124, 2005–2020. https://doi.org/10.1029/2018JG004883

Rascher, U., Agati, G., Alonso, L., Cecchi, G., Champagne, S., Colombo, R., Damm, A., Daumard, F., de Miguel, E., Fernandez, G., Franch, B., Franke, J., Gerbig, C., Gioli, B., Gomez, J.A., Goulas, Y., Guanter, L., Gutierrez-de-la-Camara, O., Hamdi, K., Hostert, P., Jimenez, M., Kosvancova, M., Lognoli, D., Meroni, M., Miglietta, F., Moersch, A., Moreno, J., Moya, I., Neininger, B., Okujeni, A., Ounis, A., Palombi, L., Raimondi, V., Schickling, A., Sobrino, J.A., Stellmes, M., Toci, G., Toscano, P., Udelhoven, T., van der Linden, S., Zaldei, A., 2009. CEFLES2: The remote sensing component to quantify photosynthetic efficiency from the leaf to the region by measuring sun-induced fluorescence in the oxygen absorption bands. Biogeosciences 6, 1181–1198. https://doi.org/10.5194/bg-6-1181-2009

Rascher, U., Alonso, L., Burkart, A., Cilia, C., Cogliati, S., Colombo, R., Damm, A., Drusch, M., Guanter, L., Hanus, J., Hyvarinen, T., Julitta, T., Jussila, J., Kataja, K., Kokkalis, P., Kraft, S., Kraska, T., Matveeva, M., Moreno, J., Muller, O., Panigada, C., Pikl, M., Pinto, F., Prey, L., Pude, R., Rossini, M., Schickling, A., Schurr, U., Schuttemeyer, D., Verrelst, J., Zemek, F., 2015. Sun-induced fluorescence - a new probe of photosynthesis: First maps from the imaging spectrometer HyPlant. Global Change Biology 21, 4673–4684. https://doi.org/10.1111/gcb.13017

Rossini, M., Meroni, M., Celesti, M., Cogliati, S., Julitta, T., Panigada, C., Rascher, U., van der Tol, C., Colombo, R., 2016. Analysis of red and far-red sun-induced chlorophyll fluorescence and their ratio in different canopies based on observed and modeled data. Remote Sensing 8, 1–16. https://doi.org/10.3390/rs8050412

Rossini, M., Meroni, M., Migliavacca, M., Manca, G., Cogliati, S., Busetto, L., Picchi, V., Cescatti, A., Seufert, G., Colombo, R., 2010. High resolution field spectroscopy measurements for estimating gross ecosystem production in a rice field. Agricultural and Forest Meteorol. 150, 1283–96. doi.org/10.1016/j.agrformet.2010.05.011

Rossini, M., Nedbal, L., Guanter, L., Ac, A., Alonso, L., Burkart, A., Cogliati, S., Colombo, R., Damm, A., Drusch, M., Hanus, J., Janoutova, R., Julitta, T., Kokkalis, P., Moreno, J., Novotny, J., Panigada, C., Pinto, F., Schickling, A., Schuettemeyer, D., Zemek, F., Rascher, U., 2015. Red and far red Sun-induced chlorophyll fluorescence as a measure of plant photosynthesis. Geophysical Research Letters 42, 1632–1639. https://doi.org/10.1002/2014GL062943

Rotach, M.W., Wohlfahrt, G., Hansel, A., Reif, M., Wagner, J., Gohm, A., 2014. The World is Not Flat: Implications for the Global Carbon Balance. Bulletin of the American Meteorological Soc. 95, 1021–28. doi.org/10.1175/BAMS-D-13-00109.1

RStudio Team, 2015. RStudio: Integrated Development for R.

Ryu, Y., Berry, J.A., Baldocchi, D.D., 2019. What is global photosynthesis? History, uncertainties and opportunities. Remote Sensing of Environment 223, 95–114. https://doi.org/10.1016/j.rse.2019.01.016

Sabater, N., Vicent, J., Alonso, L., Verrelst, J., Middleton, E.M., Porcar-Castell, A., Moreno, J., 2018. Compensation of oxygen transmittance effects for proximal sensing retrieval of canopy-leaving sun-induced chlorophyll Fluorescence. Remote Sensing 10, 1–29. https://doi.org/10.3390/rs10101551

Shan, N., Ju, W., Migliavacca, M., Martini, D., Guanter, L., Chen, J., Goulas, Y., Zhang, Y., 2019. Modeling canopy conductance and transpiration from solar-induced chlorophyll fluorescence. Agricultural and Forest Meteorology 268, 189–201. https://doi.org/10.1016/j.agrformet.2019.01.031

Sims, D.A., Rahman, A.F., Cordova, V.D., El-Masri, B.Z., Baldocchi, D.D., Bolstad, P. V., Flanagan, L.B., Goldstein, A.H., Hollinger, D.Y., Misson, L., Monson, R.K., Oechel, W.C., Schmid, H.P., Wofsy, S.C., Xu, L., 2008. A new model of gross primary productivity for North American ecosystems based solely on the enhanced vegetation index and land surface temperature from MODIS. Remote Sensing of Environment 112, 1633–1646. https://doi.org/10.1016/j.rse.2007.08.004

Smith, I.A., Hutyra, L.R., Reinmann, A.B., Thompson, J.R., Allen, D.W., 2019. Evidence for Edge Enhancements of Soil Respiration in Temperate Forests. Geophysical Research Letters 46, 4278–4287. https://doi.org/10.1029/2019GL082459

Springer, K.R., Wang, R., Gamon, J.A., 2017. Parallel Seasonal Patterns of Photosynthesis, Fluorescence, and Reflectance Indices in Boreal Trees. Remote Sensing 9. https://doi.org/10.3390/rs9070691

Stutz, J., Platt, U., 1996. Numerical analysis and estimation of the statistical error of differential optical absorption spectroscopy measurements with least-squares methods. Applied Optics 35, 6041–6053. https://doi.org/10.1364/AO.35.006041

Sun, Y., Frankenberg, C., Jung, M., Joiner, J., Guanter, L., Köhler, P., Magney, T., 2018. Overview of Solar-Induced chlorophyll Fluorescence (SIF) from the Orbiting Carbon Observatory-2: Retrieval, cross-mission comparison, and global monitoring for GPP. Remote Sensing of Environment 209, 808–823. https://doi.org/10.1016/j.rse.2018.02.016

Sun, Y., Frankenberg, C., Wood, J.D., Schimel, D.S., Jung, M., Guanter, L., Drewry, D.T., Verma, M., Porcar-Castell, A., Griffis, T.J., Gu, L., Magney, T.S., Köhler, P., Evans, B., Yuen, K., 2017. OCO-2 advances photosynthesis observation from space via solar-induced chlorophyll fluorescence. Science 358, 1–6. https://doi.org/10.1126/science.aam5747

Thieurmel, B., Elmarhraoui, A., 2019. suncalc.

Thompson, S.D., Nelson, T.A., Coops, N.C., Wulder, M.A., Lantz, T.C., 2017. Global Spatial–Temporal Variability in Terrestrial Productivity and Phenology Regimes between 2000 and 2012. Annals of the American Association of Geographers. 107, 1519–1537. https://doi.org/10.1080/24694452.2017.1309964

Tsai, B.K., Allen, D.W., Hanssen, L.M., Wilthan, B., Zeng, J., 2008. A Comparison of Optical Properties between High Density and Low Density Sintered PTFE. Proceedings of SPIE 7065: Reflection, Scattering and Diffraction from Surfaces 70650Y, 1–9. https://doi.org/10.1117/12.798138

Tucker, C.J., 1979. Red and Photographic Infrared Linear Combinations for Monitoring Vegetation. Greenbelt, USA.

van der Tol, C., Berry, J.A., Campbell, P.K.E., Rascher, U., 2014. Models of fluorescence and photosynthesis for interpreting measurements of solar-induced chlorophyll fluorescence. Journal of Geophysical Research – Biogeosciences 119, 2312–2327. https://doi.org/10.1002/2014JG002713

Van Wittenberghe, S., Alonso, L., Verrelst, J., Hermans, I., Delegido, J., Veroustraete, F., Valcke, R., Moreno, J., Samson, R., 2013. Upward and downward solar-induced chlorophyll fluorescence yield indices of four tree species as indicators of traffic pollution in Valencia. Environmental Pollution 173, 29–37. https://doi.org/10.1016/j.envpol.2012.10.003

Van Wittenberghe, S., Alonso, L., Verrelst, J., Moreno, J., Samson, R., 2015. Bidirectional sun-induced chlorophyll fluorescence emission is influenced by leaf structure and light scattering properties - A bottom-up approach. Remote Sensing of Environment 158, 169–179. https://doi.org/10.1016/j.rse.2014.11.012

Verhoeven, A.S., Adams, W.W., Demmig-Adams, B., 1999. The xanthophyll cycle and acclimation of Pinus ponderosa and Malva neglecta to winter stress. Oecologia 118, 277–287. https://doi.org/10.1007/s004420050728

Verma, M., Schimel, D., Evans, B., Frankenberg, C., Beringer, J., Drewry, D.T., Magney, T., Marang, I., Hutley, L., Moore, C., Eldering, A., 2017. Effect of environmental conditions on the relationship between solar-induced fluorescence and gross primary productivity at an OzFlux grassland site. J. Geophyiscal Research - Biogeosciences

122, 716–733. https://doi.org/10.1002/2016JG003580

Verrelst, J., Pablo Rivera, J., van der Tol, C., Magnani, F., Mohammed, G., Moreno, J., 2015. Global sensitivity analysis of the SCOPE model: What drives simulated canopy-leaving sun-induced fluorescence? Remote Sensing of Environment 166, 8–21. https://doi.org/10.1016/j.rse.2015.06.002

von Hebel, C., Matveeva, M., Verweij, E., Rademske, P., Kaufmann, M.S., Brogi, C., Vereecken, H., Rascher, U., van der Kruk, J., 2018. Understanding Soil and Plant Interaction by Combining Ground-Based Quantitative Electromagnetic Induction and Airborne Hyperspectral Data. Geophysical Research Letters 45, 7571–7579. https://doi.org/10.1029/2018GL078658

Wang, X., Chen, J.M., Ju, W., 2020. Photochemical reflectance index (PRI) can be used to improve the relationship between gross primary productivity (GPP) and sun-induced chlorophyll fluorescence (SIF). Remote Sensing of Environment 246, 111888. https://doi.org/10.1016/j.rse.2020.111888

Watt, M.S., Buddenbaum, H., Leonardo, E.M.C., Estarija, H.J., Bown, H.E., Gomez-Gallego, M., Hartley, R.J.L., Pearse, G.D., Massam, P., Wright, L., Zarco-Tejada, P.J., 2020. Monitoring biochemical limitations to photosynthesis in N and P-limited radiata pine using plant functional traits quantified from hyperspectral imagery. Remote Sensing of Environment 248, 112003. doi.org/10.1016/j.rse.2020.112003

Weather Underground, n.d. Chantilly, VA Weather History [WWW Document]. URL https://www.wunderground.com/history/daily/us/md/gaithersburg/KIAD (accessed 5.4.20).

Wickham, H., Averick, M., Bryan, J., Chang, W., McGowan, L.D., François, R., Grolemund, G., Hayes, A., Henry, L., Hester, J., Kuhn, M., Pederson, T.L., Miller, E., Bache, S.M., Müller, K., Ooms, J., Robinson, D., Seidel, D.P., Spinu, V., Takahashi, K., Vaughan, D., Wilke, C., Woo, K., Yutani, H., 2019. Welcome to the tidyverse. Journal of Open Source Software 4, 1–1686.

Wieneke, S., Burkart, A., Cendrero-Mateo, M.P., Julitta, T., Rossini, M., Schickling, A., Schmidt, M., Rascher, U., 2018. Linking photosynthesis and sun-induced fluorescence at sub-daily to seasonal scales. Remote Sensing of Environment 219, 247–258. https://doi.org/10.1016/j.rse.2018.10.019

Wohlfahrt, G., Gerdel, K., Migliavacca, M., Rotenberg, E., Tatarinov, F., Muller, J., Hammerle, A., Julitta, T., Spielmann, F.M., Yakir, D., 2018. Sun-induced fluorescence and gross primary productivity during a heat wave. Scientific Reports 8, 1–9. https://doi.org/10.1038/s41598-018-32602-z

Wolf, J., West, T.O., Le Page, Y., Kyle, G.P., Zhang, X., Collatz, G.J., Imhoff, M.L.,

2015. Biogenic carbon fluxes from global agricultural production and consumption. Global Biogeochemical Cycles 29, 1617–1639. doi.org/10.1002/2015GB005119

Wood, J.D., Griffis, T.J., Baker, J.M., Frankenberg, C., Verma, M., Yuen, K., 2017. Multiscale analyses of solar-induced fluorescence and gross primary production. Geophysical Researcj Letters 44, 533–541. https://doi.org/10.1002/2016GL070775

Wyber, R., Malenovský, Z., Ashcroft, M.B., Osmond, B., Robinson, S.A., 2017. Do daily and seasonal trends in leaf solar induced fluorescence reflect changes in photosynthesis, growth or light exposure? Remote Sensing 9, 1–19. https://doi.org/10.3390/rs9060604

Xiao, J., Li, X., He, B., Arain, M.A., Beringer, J., Desai, A.R., Emmel, C., Hollinger, D.Y., Krasnova, A., Mammarella, I., Noe, S.M., Serrano Ortiz, P., Rey-Sanchez, C., Rocha, A. V., Varlagin, A., 2019. Solar-induced chlorophyll fluorescence exhibits a universal relationship with gross primary productivity across a wide variety of biomes. Global Change Biology 1–4. https://doi.org/10.1111/gcb.14565

Xu, S., Liu, Z., Zhao, L., Zhao, H., Ren, S., 2018. Diurnal Response of Sun-Induced Fluorescence and PRI to Water Stress in Maize Using a Near-Surface Remote Sensing Platform. Remote Sensing 10, 1–17. https://doi.org/10.3390/rs10101510

Yang, H., Yang, X., Zhang, Y., Heskel, M.A., Lu, X., Munger, J.W., Sun, S., Tang, J., 2017. Chlorophyll fluorescence tracks seasonal variations of photosynthesis from leaf to canopy in a temperate forest. Global Change Biology 23, 2874–2886. https://doi.org/10.1111/gcb.13590

Yang, X., Shi, H., Stovall, A., Guan, K., Miao, G., Zhang, Yongguang, Zhang, Yao, Xiao, X., Ryu, Y., Lee, J.-E., 2018. FluoSpec 2-An Automated Field Spectroscopy System to Monitor Canopy Solar-Induced Fluorescence. Sensors 18, 1–18. https://doi.org/10.3390/s18072063

Yang, X., Tang, J., Mustard, J.F., Lee, J.-E.E., Rossini, M., Joiner, J., Munger, J.W., Kornfeld, A., Richardson, A.D., 2015. Solar-induced chlorophyll fluorescence that correlates with canopy photosynthesis on diurnal and seasonal scales in a temperate deciduous forest. Geophysical Research Letters 42, 2977–2987. https://doi.org/10.1002/2015GL063201

Yoshida, Y., Joiner, J., Tucker, C., Berry, J., Lee, J.E., Walker, G., Reichle, R., Koster, R., Lyapustin, A., Wang, Y., 2015. The 2010 Russian drought impact on satellite measurements of solar-induced chlorophyll fluorescence: Insights from modeling and comparisons with parameters derived from satellite reflectances. Remote Sensing of Environment 166, 163–177. https://doi.org/10.1016/j.rse.2015.06.008

Zarco-Tejada, P.J., Catalina, A., González, M.R., Martín, P., 2013. Relationships between net photosynthesis and steady-state chlorophyll fluorescence retrieved from airborne hyperspectral imagery. Remote Sensing of Environment 136, 247–258. https://doi.org/10.1016/j.rse.2013.05.011

Zarco-Tejada, P.J., Gonzalez-Dugo, M. V, Fereres, E., 2016. Seasonal stability of chlorophyll fluorescence quantified from airborne hyperspectral imagery as an indicator of net photosynthesis in the context of precision agriculture. Remote Sensing of Environment 179, 89–103. https://doi.org/10.1016/j.rse.2016.03.024

Zeng, Y., Badgley, G., Dechant, B., Ryu, Y., Chen, M., Berry, J.A., 2019. A practical approach for estimating the escape ratio of near-infrared solar-induced chlorophyll fluorescence. Remote Sensing of Environment 232, 111209. https://doi.org/10.1016/j.rse.2019.05.028

Zhang, Yongguang, Joiner, J., Guan, K., Yang, X., 2018. Sun-Induced Chlorophyll Fluorescence as a Proxy of Photosynthesis: Measurements, Modeling, and Applications from Field, Airborne, and Satellite Platforms, in: American Geophysical Union Fall Meeting. Washington, D.C.

Zhang, Y J, Hou, M.Y., Xue, H.Y., Liu, L.T., Sun, H.C., Li, C.D., Dong, X.J., 2018. Photochemical reflectance index and solar-induced fluorescence for assessing cotton photosynthesis under water-deficit stress. Biologia Plantarum 62, 817–825. https://doi.org/10.1007/s10535-018-0821-4

Zhang, Yao, Xiao, X., Zhang, Yongguang, Wolf, S., Zhou, S., Joiner, J., Guanter, L., Verma, M., Sun, Y., Yang, X., Paul-Limoges, E., Gough, C.M., Wohlfahrt, G., Gioli, B., van der Tol, C., Yann, N., Lund, M., de Grandcourt, A., 2018. On the relationship between sub-daily instantaneous and daily total gross primary production: Implications for interpreting satellite-based SIF retrievals. Remote Sensing of Environment 205, 276–289. https://doi.org/10.1016/j.rse.2017.12.009

Zhang, Zhaoying, Zhang, Y., Joiner, J., Migliavacca, M., 2018. Angle matters: bidirectional effects impact the slope of relationship between gross primary productivity and sun-induced chlorophyll fluorescence from Orbiting Carbon Observatory-2 across biomes. Global Change Biology 1–4. https://doi.org/10.1111/gcb.14427

Zong, Y., Brown, S.W., Johnson, B.C., Lykke, K.R., Ohno, Y., 2006. Simple spectral stray light correction method for array spectroradiometers. Applied Optics 45, 1111–1119. https://doi.org/10.1364/AO.45.001111

CURRICULUM VITAE

[redacted]

[redacted]

[redacted]